Characterization of Organic Semiconductors and Optoelectronic Elements

C. Melzer

Characterization of
Organic Semiconductors
and Optoelectronic Elements
C. Melzer
Ph.D. thesis
University of Groningen, The Netherlands

MSC Ph.D.-thesis series 2004-05
ISSN: 1570-1530

ISBN: 90-367-2058-3

Cover: Photograph of a light-emitting diode based on a conjugated oligomer.

The Council for Chemical Sciences of the Netherlands Organization for Scientific Research (CW-NWO) has financially supported this research.

Rijks*universiteit* Groningen

Characterization of Organic Semiconductors and Optoelectronic Elements

Proefschrift

ter verkrijging van het doctoraat in de
Wiskunde en Natuurwetenschappen
aan de Rijksuniversiteit Groningen
op gezag van de
Rector Magnificus, dr. F. Zwarts,
in het openbaar te verdedigen op
vrijdag 2 juli 2004
om 13.15 uur

door

Christian Melzer

geboren op 12 mei 1970
te Mannheim, Duitsland

Promotor: Prof. Dr. G. Hadziioannou

Beoordelingscommissie: Prof. Dr. P. W. M. Blom
Prof. Dr. T. Heiser
Prof. Dr. G. G. Malliaras

Contents

1

Introduction

Abstract

In this chapter, conjugated oligomers and polymers are introduced as a novel class of semiconductors and the origin of their semiconducting properties is discussed. These active plastics are already applied in several commercially available products such as light-emitting diodes (LEDs), but until now failed to be competitive in other well-established applications, e.g. solar cells. The operation principles of organic solar cells and LEDs are briefly described and the possible limitations of their device performances are discussed, leading to the outline of this thesis.

1.1 Semiconducting plastics

Nowadays, organic compounds acquired from mineral oil find their utilization in a variety of new materials. One class of these omnipresent oil-based materials comprises the so-called plastics, which are employed in all branches of modern life. Indeed, we encounter plastics on a daily base, in clothes, as bags or even furniture. Plastics are carbonic compounds, which consist of chain-like molecules (polymers) based on chemically equal subunits (monomers). The typically used plastics have the advantage that they are light-weighted, flexible and resistant against environmental influences such as corrosion, but simultaneously exhibit remarkable mechanical strength. The most important reason why plastics are so frequently used in a variety of applications is their easy processability, which makes the fabrication of plastic-based products rather cheap. Until today, however, plastics mainly served as non-active materials, generally as passive, formed parts. They also found their application in electronics, where their insulating properties are appreciated. Polyethylene, polyisoprene or polyvinylidene fluoride, for instance, serve as isolation for electrical wiring. A future prospect is to provide electronics completely made from plastics, combining the mechanical properties and low production costs of polymeric materials with the electrical properties of semiconductors in one material.

The first step towards such functional organic materials was done in the early 1950's, when electrical conduction was observed in anthracene crystals [1, 2], even though the electrical conductivity was extremely low. In the following years, guest/host polymer systems found their use in xerographic applications [3-5]. Nonetheless, the polymeric host with the favorable mechanical properties was still inactive, serving mainly as a matrix for the conducting guest particles. It took several

Figure 1.1 A selection of commercially available products, in which semiconducting organic moieties are employed. *Top, left*: Pioneer car radio with an oLED display. *Right*: Philips shaver with a pLED display. *Bottom left*: Kodak digital camera with an oLED display.

more years, before a radical breakthrough was made. Upon doping polyacetylene with iodine, an increase of the electrical conductivity by ten orders of magnitude was unveiled [6, 7]. This discovery opened an entirely new perspective on the applicability of organic molecules as active materials in modern electronics. Since this time, novel semiconducting polymers, oligomers, and small molecules have been designed for applications usually based on inorganic semiconductors. With organic light-emitting diodes (oLEDs, [8]) being already used in matrix displays (Fig. 1.1), organic photodetectors [9, 10] that are implemented in large-area image sensors [11, 12] and all-organic integrated circuits [13] being produced from organic field effect transistors [14-16], the discovery of organic semiconductors can be regarded as a major scientific breakthrough with high technological impact. Two frequently investigated applications of organic semiconductors are LEDs [17-20] and photovoltaic cells [21-26], which will in detail be discussed below.

The insulating properties of most of the industrial plastics available, which limit their use to passive applications, result from the fact that the imbedded carbon atoms exclusively form σ-bonds in the sp^3 configuration with four adjacent atoms. Polystyrene, nylon, and polyvinyl chloride (PVC) are typical examples of these saturated polymers, which we encounter on a daily base. However, in polyacetylene, for example, the situation is different. Polyacetylene belongs to a class of conjugated polymers, in which single and double bonds alternate in the polymeric main chain (conjugation). Each carbon atom solely binds to three adjacent atoms, which leaves one electron in the p_z orbital of the $sp^2p_z^1$ configuration (Fig. 1.2). The mutual overlap of the p_z orbitals along the conjugation path results in the formation of π-bands and, hence, in a π-electron density extending over the entire conjugation path. Since the π-bands are either fully filled with electrons or fully empty, conjugated systems are intrinsic semiconductors with a band gap typically in the range from 1 to 4 eV. A variety of conjugated moieties are depicted in Fig. 1.3.

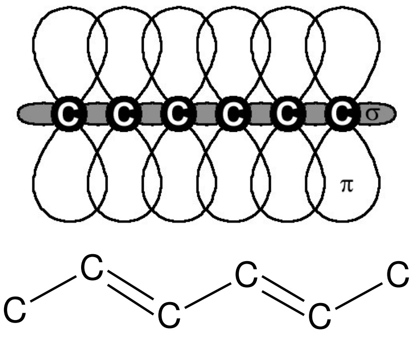

Figure 1.2 Scheme of orbitals (above) involved in the bonding between carbons in a conjugated backbone (below)

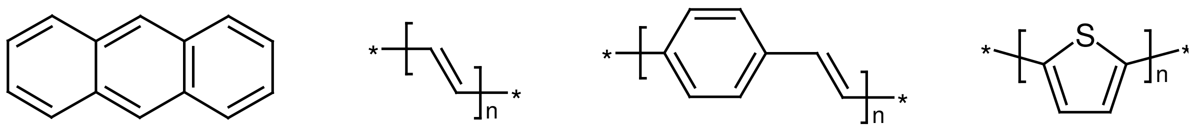

anthracene polyacetylene poly(*p*-phenylene vinylene) polythiophene

Figure 1.3 Some examples of conjugated organic molecules

1.2 Organic light-emitting diodes (oLEDs)

The first report on electroluminescence (EL) from organic semiconductors goes back to 1963. Pope *et al.* observed EL from anthracene crystals by employing silver paste electrodes [17], but since these crystals were several µm thick, operation voltages of hundreds of volts were required. As a consequence, the suitability of organic semiconductors for applications such as LEDs was regarded to be negligible. In 1987, however, the perspective of organic materials in LEDs was renewed, when operation voltages were strongly reduced by employing thin films of small molecules [27, 28]. Since then, LEDs based on small conjugated molecules were intensively studied and improved, which led to high brightness, long-term stability and excellent color purity. These developments finally allowed the use of LEDs based on small organic molecules in full-color displays (Fig. 1.1). The first EL from polymers was reported by Partridge *et al.* in 1983, employing polyvinylcarbazole [29], while real interest in polymer-based LEDs awoke not before the early 1990's when EL was observed in thin films of poly(phenylene vinylene) (PPV) [18]. Even though the scientific and technological effort made was tremendous, the earliest commercially available displays based on pure polymeric semiconductors appeared only very recently (Fig. 1.1).

The device operation scheme and the corresponding energy diagram of a single-layer oLED are depicted in Fig. 1.4. A thin film of an organic semiconductor is sandwiched between an anode and a cathode, resulting in a planar diode structure. Upon biasing the diode in forward direction, holes are injected from the anode and electrons from the cathode into the organic semiconductor (1). The injected charge carriers subsequently migrate towards each other by the aid of the externally applied field (2) until they meet and radiative recombination occurs (3).

Due to the nature of excitations in the organic semiconductor, the maximally possible quantum efficiency attainable with these LEDs is yet restricted. When a hole and an electron meet, they form a new excited state of a strongly bound electron/hole pair, an exciton [30, 31]. This results from the fact that in organic semiconductors, the dielectric constant is rather low, because organic molecules retain their electronic individuality in the bulk. As a consequence, Coulombic interactions become significant. Since this new quasi-particle is created out of two spin-½ particles, singlet

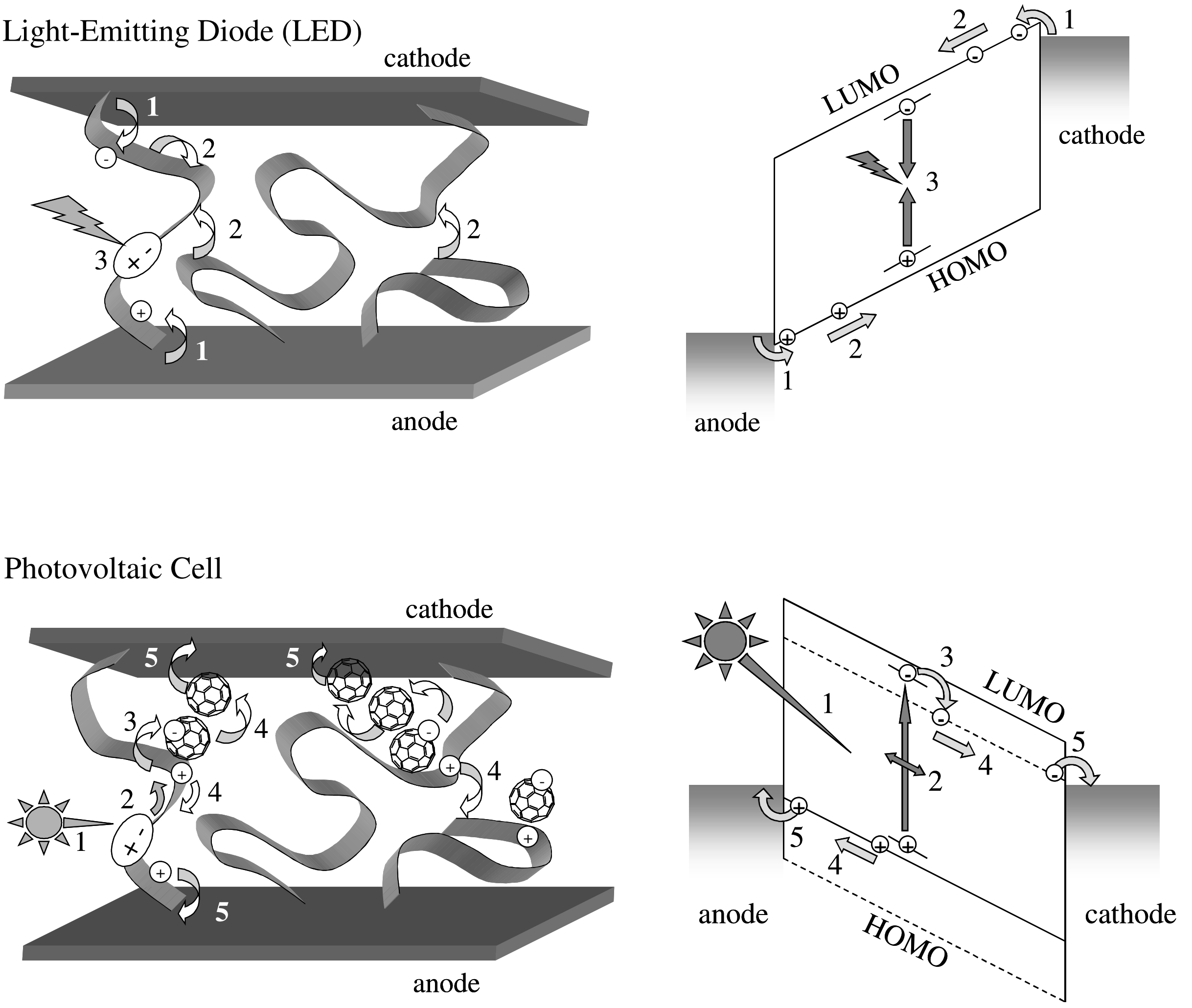

Light-Emitting Diode (LED)

Photovoltaic Cell

Figure 1.4 Operation principles of organic LEDs and photovoltaic cells, and their corresponding energy diagrams. The numbers refer to the device operation steps explained in the text. The dashed lines represent the energy levels of the acceptor, while the straight lines indicate the energy levels of the donor of a photovoltaic cell.

exciton of spin 0 and three-fold degenerated triplet excitons of spin 1 exist. In first instance, radiative decay of excitons is solely allowed from the singlet state, which limits the maximally possible quantum efficiency to 25 %. However, the here-mentioned spin statistics do not strictly hold in polymers and efficiencies of up to 60 % were previously obtained [32-34]. In order to approach the maximally possible quantum efficiency, a number of requirements must be fulfilled. Typically, large and balanced injection efficiencies and charge carrier mobilities as well as a high radiative recombination probability result in high electron-to-photon conversions.

Since, for example, high hole and electron densities are required in the semiconductor to achieve a reasonable brightness, interfacial energy barriers determining the hole and electron injection rates have to be as small as possible. This requires that a low-workfunction metal is used as the cathode, while a high-workfunction metal should serve as the anode, so that high injection rates of the charge carriers are achieved at each electrode. Preferably, both metals should form ohmic contacts with the semiconductor, resulting in the maximal hole and electron densities achievable in the semiconductor.

Moreover, a balanced electron and hole transport, involving identical injection and bulk transport properties, is required for a high quantum efficiency. In this case, the recombination zone is centered in the semiconductor. However, when the charge transport of holes and electrons is unequally fast, the recombination zone shifts towards one of the electrodes [20]. Then, the excitons formed in the recombination zone decay non-radiatively by energy transfer from the organic material to the metal [35], thereby decreasing the quantum efficiency substantially. The introduction of a double-layer LED structure based on a hole and an electron-transporting layer reduces this undesired effect, since the recombination area is located close to the heterojunction interface.

1.3 Organic photovoltaic cells

While oLEDs convert electrical power into light power, photodetectors convert light power in electrical power. This is effectively used in a special type of photodetectors, the solar cell, where solar power is used to create electricity via the photovoltaic effect. Kallman *et al.* reported the first organic photovoltaic cell based on a single crystal of anthracene in 1959 [21]. When semiconducting organic materials were just discovered, however, cells based on one organic material were regarded to be unsuitable as energy source for any imaginable application. This was partly based on the fact that optical excitations lead to strongly bound electron/hole pairs. Photogenerated charge carriers are, hence, not directly accessible for the external circuit, which results in an insufficient external quantum efficiency. Concomitantly, the observed poor photovoltaic response was attributed to the quasi-insulating nature of the intrinsic organic semiconductors. In combination with the typically used layer thickness of hundreds of microns, this led to high series resistances and, consequently, to limited fill factors. It lasted up to 1986, before it was finally reported that fill factors of 65 % can be obtained, using thin-film double-layer photovoltaic cells of copper phtalocyanine and a perylene tetracarboxylic derivative [36]. This result stimulated efforts towards organic photovoltaic cells, now applying the donor/acceptor concept in the thin-film configuration. After the discovery of the photoinduced electron transfer from a conducting polymer to C_{60} [37], the concept was effectively extended to polymeric systems [22, 23]. Nowadays, bulk heterojunction solar cells using PPV derivatives as donor and solubilized fullerene derivatives as acceptor materials reach power conversion efficiencies of 3 % at AM1.5 [25, 26]. However, the obtained efficiencies still lag behind the efficiencies reached with commercial silicon solar cells of 15 %, which requires a deeper understanding of organic solar cells for further improvements.

A schematic picture of an organic donor/acceptor-based photovoltaic cell and the corresponding energy diagram is depicted in Fig. 1.4. In a donor/acceptor organic photovoltaic cell, light absorption results in the creation of singlet excitons (1) in the donor phase. In order to achieve a high exciton generation rate, the absorption spectrum of the donor should preferably match the solar spectrum. This requires a band gap of the donor between 1.1 and 1.7 eV [38]. Concomitantly, the extinction coefficients should be large. However, since the excited electrons are strongly bound to their corresponding holes, the photogenerated charges cannot directly contribute to a drift photocurrent. The mobile excitons diffuse [30] over several nm [39] (2) until they decay and charges get lost for the external circuit. This is the reason why in photovoltaic cells of pristine organic semiconductors, the photoresponse is rather poor. However, when the excitons reach a donor/acceptor interface, an ultra-fast metastable electron transfer from the donor to the acceptor (sub-picosecond range) occurs [37, 40], localizing the hole in the donor and the electron in the acceptor phase (3). Still, the majority of excitons that are photogenerated in a planar donor/acceptor double-layer structure are lost for the external photocurrent, since the exciton diffusion length is typically smaller than the penetration depth of the light. Therefore, bulk heterojunction systems, in which the donor/acceptor heterojunction is distributed in the entire active layer are typically employed [23], thereby increasing the photon-to-electron conversion efficiency and, hence, the photovoltaic sensitivity dramatically.

Since the electron transfer at the heterojunction interface occurs so fast that no other decay mechanism can compete, its efficiency is close to unity. Yet, the separated charge carriers are still bound due to the Coulomb force. At typical operation conditions, the photon-to-free-electron conversion efficiency is, therefore, not maximal [41].

Once the photogenerated charges are set free (by an electric field), they are transported by aid of an internal electric field towards the anode and the cathode (4), which finally results in an external photocurrent (5). The internal electric field, determining the open-circuit voltage of the photovoltaic cell, is caused by the use of electrode metals with different workfunctions. Yet, in the transport step (4), recombination of the free photogenerated charge carriers might further limit the external photocurrent. Recombination is important as long as the transit time of the photogenerated free charge carriers is longer than their lifetime (recombination time), while no recombination occurs for charge carrier lifetimes that are longer than the corresponding transit times [42]. In the latter situation, the electrodes extract all photogenerated free charge carriers.

In the extreme case when electron and hole transport properties are strongly unbalanced, charges of the slower charge carrier species accumulate in the device, thereby modifying the electric field to such extent that the external hole current equals the external electron current. The charge accumulation might lead to a substantial built-up of space-charges and a concomitant screening of the electric field, which might occasionally limit the photoresponse of an organic donor/acceptor photovoltaic cell

[42, 43]. The presence of this phenomenon is typically reflected by a poor fill factor (≤ 0.4).

We can now summarize the essential requirements for an efficient organic photovoltaic cell: A spectral match of the solar spectrum and the absorption spectrum of the donor as well as high extinction coefficients are necessary for high exciton generation rates. The exciton diffusion length should be long in order to increase the active volume for efficient exciton dissociation. The charge carrier lifetimes should be longer than the transit times, and the charge carrier transport should be balanced in order to prevent space-charge effects.

1.4 Scope of this thesis

We have seen that conjugated organic materials share some important properties with inorganic semiconductors, such as mobile charge carrier generation by optical excitation, charge injection or chemical doping, which make them highly interesting for semiconductor applications. Yet, material-specific differences remain. Even though π-electron densities are extended along the conjugation path, charge carriers are not delocalized over the entire semiconductor as it is typically the case in inorganic semiconductors [44]. The localization of charge carriers in organic solids partly finds its origin in the strong polarizability of organic molecules, which in combination with the weak intermolecular interaction induces self-trapping of excess carriers [31]. In molecular crystals, this self-trapping process causes charge carrier localization. The degree of charge carrier localization depends, however, on the relative magnitude of the involved nearest-neighbor interaction and polarization energies. For materials, in which the polarization energy approaches the intermolecular interaction energy, the charge carrier localization is weak, since the carrier transfer time between adjacent molecules is short. In amorphous organic semiconductors, in contrast, where the intermolecular as well as the conformational order of individual molecules is limited, all possible coherence effects are eliminated [45], which leads to truly localized charges.

One consequence of the charge carrier localization is that charge carrier transport occurs via subsequent charge transfer steps from one localized state to another, similar to the hopping between defect states in inorganic semiconductors. Hopping transport is thermally activated and the charge carrier mobility, therefore, increases with rising temperature. This is in clear contrast to the band picture, where charge carrier transport is limited by the scattering of the charge carriers on phonons. Since the phonon density increases upon temperature increase, the charge carrier mobility decreases. The validity of the band picture for organic semiconductors is, hence, restricted.

From the upper example, it becomes apparent that the nature of the charge carrier transport through a semiconductor bulk material is related to the order in the system and, consequently, to the conformational and morphological properties of the organic molecules and their ensemble. Beyond charge transport in organic semiconductors, the film organization in general sways the device operation of organic diodes and optoelectronic elements, such as organic rectifiers, oLEDs or photovoltaic cells, which is the subject of this thesis.

Since the device properties of diodes based on organic compounds are extremely sensitive to the environmental conditions, in particular to the presence of oxygen and moisture, an entire preparation and characterization setup in a single glove-box system with inert atmosphere was constructed for the presented experimental research. This system and the device preparation and characterization are described in *Chapter 2*. Moreover, an electrical test station is introduced, which was attached to a photoelectron spectroscopy setup, allowing the preparation and characterization of diodes based on organic materials under ultra-high vacuum conditions.

In *Chapter 3*, we emphasize the significant aspects in the charge injection process from a metal to an organic semiconductor, and present a phenomenological charge injection model based on these considerations. The developed model is experimentally verified.

In *Chapter 4*, the current-limiting process in single-layer diodes based on either a PPV-like oligomer or its corresponding polymer is determined. Since the employed polymer and its oligomeric counterpart were chemical alike, primarily the film morphology varied between the two systems, and we rationalize the differences in the diode behavior for the two compounds on basis of disparities in the system disorder.

The thin-film morphology of highly crystalline oligomers and their impact on the device performance is treated in *Chapter 5*. The polycrystalline thin-film morphology of a vacuum-deposited PPV derivative in a typical diode structure were investigated by optical microscopy, X-ray and electron diffraction. A change of the film morphology was introduced by varied substrate temperatures during the film deposition. Additionally, transient EL measurements were performed, providing information on the hole mobilities in the particular thin films. The unveiled transient EL traces and the corresponding hole mobilities are discussed, considering the thin-film morphologies of the respective devices.

In *Chapter 6*, we discuss the current-voltage characteristics of diodes based on small organic molecules prepared and characterized in ultra-high vacuum. The results are compared with the corresponding energy diagrams of the investigated diodes determined by ultraviolet photoelectron spectroscopy (UPS) that provide information on the charge carrier injection barriers.

The influence of the film organization on the performance of donor/acceptor-based photovoltaic cells is finally discussed in *Chapter 7*. The photovoltaic performance of planar double-layer cells with one single planar heterojunction is compared with the one of cells based on a blend of the same donor and acceptor materials. In particular, the influence of the film organization of theses diodes on the open-circuit voltage and the photovoltaic sensitivity is in the focus of this chapter. Furthermore, the action spectra of double-layer photovoltaic cells are discussed for several donor-type materials with different film-forming properties, providing information on the volume fraction that is susceptible for efficient exciton dissociation in the respective films. Finally, results on the photovoltaic performance of cells based on a donor/acceptor diblock copolymer and the corresponding thin-film morphology are presented.

References

[1] H. Mette and H. Pick, Z. Physik **134**, 566 (1953).

[2] R. G. Kepler, Phys. Rev. **119**, 1226 (1962).

[3] H. Hoegl, J. Phys. Chem. **69**, 755 (1965).

[4] D. M. Pai, J. Chem. Phys. **52**, 2285 (1970).

[5] W. D. Gill, J. Appl. Phys. **43**, 5033 (1972).

[6] C. K. Chiang, C. R. Fischer, Y. W. Park, A. J. Heeger, H. Shirakawa, E. J. Louis, S. C. Gau and A. G. MacDiarmid, Phys. Rev. Lett. **39**, 1098 (1977).

[7] H. Shirakawa, E. J. Louis, A. G. MacDiarmid, C. K. Chiang and A. J. Heeger, J. Chem. Soc. Chem. Commun. **16**, 578 (1977).

[8] J. Kalinowski, J. Phs. D: Appl. Phys. **32**, R179 (1999).

[9] G. Yu, C. Zhang and A. J. Heeger, Appl. Phys. Lett. **64**, 1540 (1994).

[10] G. Yu, K. Pakbaz and A. J. Heeger, Appl. Phys. Lett. **64**, 3422 (1994).

[11] G. Yu, J. Wang, J. McElvain and A. J. Heeger, Adv. Mater. **10**, 1431 (1998).

[12] J. Wang, G. Yu, G. Srdanov and A. J. Heeger, Organic Electronics **1**, 33 (2000).

[13] C. J. Drury, C. M. J. Mutsaers, C. M. Hart, M. Matters and D. M. de Leeuw, Appl. Phys. Lett. **73**, 108 (1998).

[14] H. Koezuka, A. Tsumara and T. Ando, Synth. Met. **18**, 699 (1987).

[15] H. Sirringhaus, N. Tessler and R. H. Friend, Science **280**, 1741 (1998).

[16] H. Sirringhaus, P. J. Brown, R. H. Friend, M. M. Nielsen, K. Bechaard, B. M. W. Langeveld-Voss, A. J. H. Spiering, R. A. J. Janssen, E. W. Meijer, P. Herwig and D. M. de Leeuw, Nature **401**, 685 (1999).

[17] M. Pope, H. P. Kallman and P. Magnante, J. Chem. Phys. **38**, 2042 (1963).

[18] J. H. Burroughes, D. D. C. Bradly, A. R. Brown, R. N. Marks, K. McKay, R. H. Friend, P. L. Burn and A. B. Holmes, Nature **347**, 539(1990).

[19] R. H. Friend, R. W. Gymer, A. B. Holmes, J. H. Burroughes, R. N. Marks, C. Taliani, D. D. C. Bradly, D. A. Dos Santos, J. L. Brédas, M. Lögdlund and W. R. Salaneck, Nature **397**, 121 (1999).

[20] P. W. M. Blom and M. C. J. M. Vissenberg, Materials Science and Engineering **27**, 53 (2000).

[21] H. Kallman and M. Pope, J. Chem. Phys. **30**, 585 (1959).

[22] N. S. Sariciftci, D. Braun, C. Zang, V. Srdanov, H. A. J., G. Stucky and F. Wudl, Appl Phys. Lett. **62**, 585 (1993).

[23] G. Yu, J. Gao, J. C. Hummelen, F. Wudl and A. J. Heeger, Science **270**, 1789 (1995).

[24] J. J. M. Halls, C. A. Walsh, N. C. Greenham, E. A. Marseglia, R. H. Friend, S. C. Moratti and A. B. Holms, Nature **376**, 498 (1995).

[25] S. E. Shaheen, C. J. Brabec, N. S. Sariciftci, F. Padinger, T. Fromherz and J. C. Hummelen, Appl. Phys. Lett. **78**, 841 (2001).

[26] T. Munters, T. Martens, L. Goris, V. Vrindts and J. Manca, Thin Solid Films **403-404**, 247 (2002).

[27] C. W. Tang and S. A. Van Slyke, Appl. Phys. Lett. **51**, 913 (1987).

[28] C. W. Tang, S. A. Van Slyke and C. H. Chen, J. Appl. Phys. **65**, 3610 (1989).

[29] R. H. Partridge, Polymer **24**, 755 (1983).

[30] D. P. Craig and S. H. Walmsley, *Excitons in Molecular Crystals*, W. A. Benjamin Inc., New York (1968).

[31] M. Pope and C. E. Swenberg, *Electronic processes in organic crystals*, Clarendon Press, Oxford Univ. Press, New York (1982).

[32] Y. Cao, I. D. Parker, G. Yu, C. Zhang and A. J. Heeger, Nature **397**, 414 (1999).

[33] M. Wohlgenannt, K. Tandon, S. Mazumdar, S. Ramasesha and Z. V. Vardeny, Nature **409**, 494 (2001).

[34] J. S. Wilson, A. S. Bhoot, A. J. A. B. Seeley, M. S. Kahn, A. Kohler and R. H. Friend, Nature **413**, 828 (2001).

[35] T. Förster, Ann. Phys. **2**, 55 (1948).

[36] C. W. Tang, Appl. Phys. Lett. **48**, 183 (1986).

[37] N. S. Sariciftci, L. Smilowitz, A. J. Heeger and F. Wudl, Science **258**, 1474 (1992).

[38] A. Goetzberg and C. Hebling, Solar Energy Materials & Solar Cells **62**, 1 (2000).

[39] J. J. M. Halls, K. Pichler, R. H. Friend, S. C. Moratti and A. B. Holms, Appl. Phys. Lett. **68**, 3120 (1996).

[40] J. C. Brabec, G. Zera and N. S. Saritiftci, Chem. Phys. Lett. **340**, 232 (2001).

[41] C. L. Braun, J. Chem. Phys. **80**, 4157 (1984).

[42] A. M. Goodman and A. Rose, J. Appl. Phys. **42**, 2823 (1971).

[43] C. Melzer, E. J. Koop, V. D. Mihailetchi and P. W. M. Blom, Adv. Funct. Mater. (2004) *accepted.*

[44] J. M. Ziman, *Prinzipien der Festkörpertheory*, Verlag Harri Deutsch, Zürich und Frankfurt am Main (1975).

[45] P. W. Anderson, Phys. Rev. **109**, 1492 (1958).

2

Experimental

Abstract

The sensibility of organic semiconductors towards exposition to oxygen and moisture is a strong limiting factor in the operation of semiconductor elements. It is apparent that care needs to be taken to prevent any contamination of the semiconductor during preparation and characterization. Therefore, a glove-box system including preparation facilities such as spin-coater and thermal vacuum deposition chambers as well as characterization facilities was set up for the presented research project. Moreover, an electrical test station was implemented to a combined system of preparation chamber and photoelectron spectroscopy unit, allowing the preparation and characterization of diodes based on organic materials under ultra-high vacuum (UHV) conditions. In this chapter, the glove-box system and the UHV electrical test station are described. In addition, we illustrate our device preparation strategies and outline the characterization units that were included in both setups.

2.1 Introduction

Organic solids such as conjugated polymers or oligomers are highly interesting for the semiconductor industries that address the fields of rectifiers, photovoltaic cells [1], or light-emitting diodes (LEDs) [2], since materials but also processing techniques are rather cheap if compared to their inorganic counterparts. A number of new processing technologies, such as spin-coating with selective solvents, ink-jet printing [3], screen printing [4], micromolding [5], or soft lithography [6] have been developed for these flexible materials. In any case, special measures need to be taken during preparation and further treatment of the manufactured devices. For instance, it is well known that the presence of moisture and oxygen results in a short lifetime of organic LEDs [7]. Due to the loose packing of polymeric or oligomeric materials, H_2O and O_2 molecules can easily penetrate in the organic films, reacting with the employed electrodes, modifying the chemical nature of the molecules, acting as traps, dopingagent or quenching sites [8-12]. As a consequence, e.g. the transport properties of a semiconductor change in time if the semiconductor is exposed to air or moisture and, hence, the device lifetime will be limited. In addition to a change of bulk properties of the organic semiconductor, contamination of interfaces formed between different organic materials or organic materials and metals is likely to occur. Yet, the charge carrier injection barrier between a metal and an organic semiconductor is known to be highly sensitive on the metal/organic interaction [13-16]. Upon polluting the metal/organic interface, the interaction between the two materials is changed, and so will be the injection barrier [16] and the charge injection current through a diode (see *Chapter 6*). These examples illustrate the importance of controlled preparation and characterization conditions for the highly sensitive devices based on organic compounds.

2.2 Glove-box system for the preparation and characterization of organic diodes

In order to prepare electrical devices based on thin films of organic materials in an oxygen- and moisture-free environment, a glove-box system was set up. The design of the glove-box system guarantied controlled conditions from the preparation up to the characterization of the desired devices. In such a way, exterior influences on the devices could be reduced, and enhanced device stability was warranted.

The system consisted of three interconnected glove-boxes filled with dry nitrogen gas (Fig. 2.1). While two of the glove-boxes were used for sample preparation, the third one was conceived as characterization box (box C). The boxes were connected via a T-ante chamber with two translation rails and a loading gate. In order to make thin-film deposition of organic compounds possible, one preparation box was designed for wet processing of organic materials (box A). Box B, on the other hand, was equipped with two separate evaporators for the deposition of small organic molecules and metals, respectively.

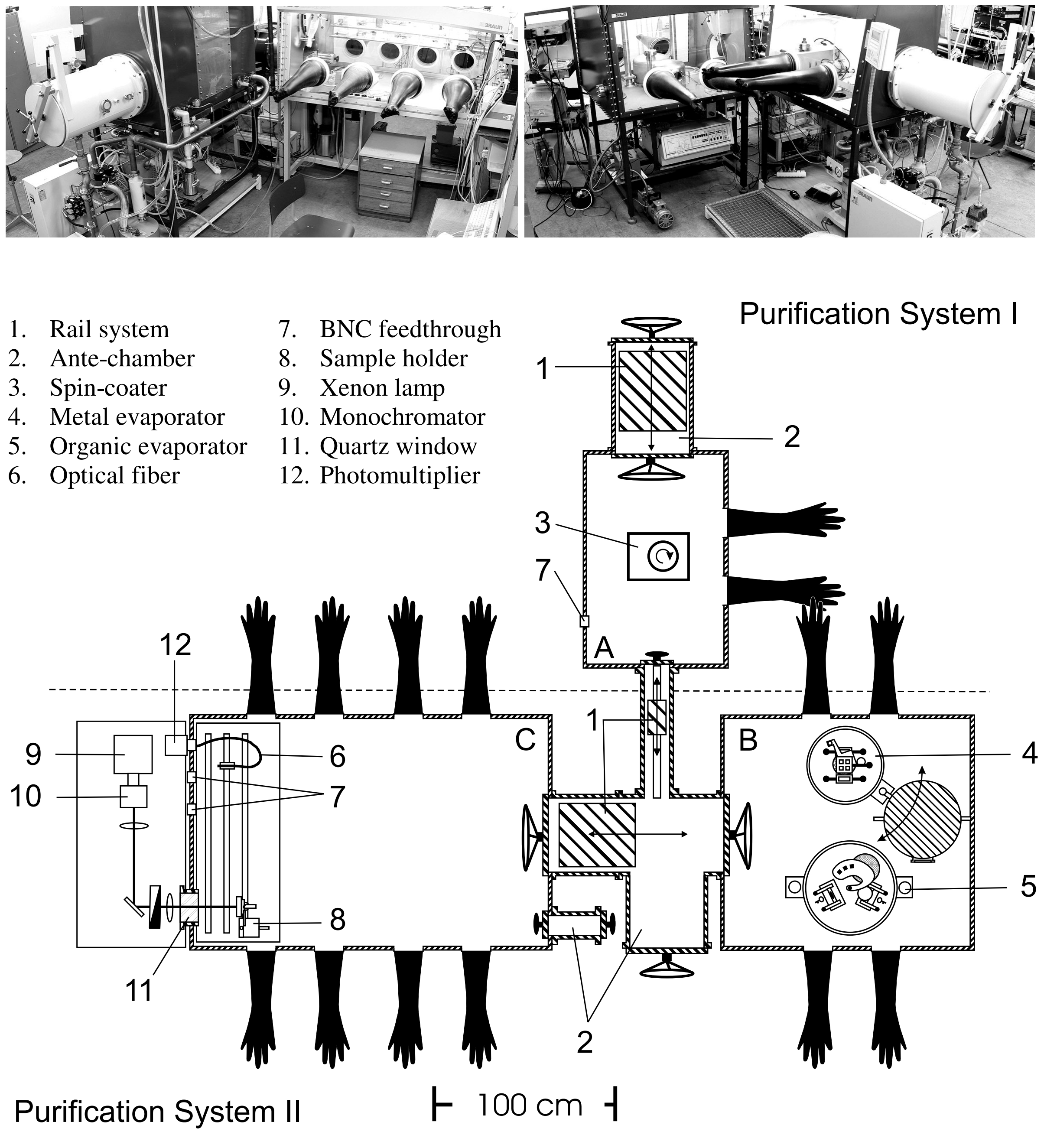

1. Rail system
2. Ante-chamber
3. Spin-coater
4. Metal evaporator
5. Organic evaporator
6. Optical fiber
7. BNC feedthrough
8. Sample holder
9. Xenon lamp
10. Monochromator
11. Quartz window
12. Photomultiplier

Figure 2.1 Glove-box system for the preparation and characterization of rectifiers and optoelectronic elements based on soft organic semiconducting materials. The system consisted of three interconnected boxes: a box for wet processing (box A), a box for thermal vacuum deposition of organic materials and metals (box B), and a box for sample characterization (box C).

Box C solely served for sample characterization, providing electrical feedthroughs and the possibility to couple light in and out off the box. The glove-box system included two gas purification systems based on a copper catalyst and molecular sieves with closed gas circulation. The wet processing box A contained a purification system that was separated from the dry boxes, protecting the latter from solvent contamination. Box B and C shared one purification system that either allowed independent gas circulation in the two boxes or parallel flow. The water and oxygen content was measured by a Combi H_2O/O_2 Analyzer MB-MO-OX-PLC-SSD and was typically below 1 ppm for all boxes.

The preparation box A, MBraun MB200 B1-I, was exclusively used for wet processing of soft materials, using organic solvents such as toluene, chloroform or 1,2-dichlorobenzene. The glove-box had its own ante-chamber in order to keep the T-ante chamber protected from solvent contamination. Moreover, the gas purification system of box A (MB 20 G) was separated from the two remaining glove-boxes, ensuring a protection of the dry boxes B and C. However, due to the high vapor pressure of the used solvents in box A, its gas purification system had to be protected by reducing the solvent content under operation. Two protection systems were implemented. The box could be operated in a flush mode, where the gas circulation in the box was stopped and the protection pump was connected via a cold-trap to the glove-box. By permanently removing the polluted nitrogen gas with the protection pump, the used solvent was captured in the trap. Simultaneously the box was refilled with dry nitrogen. In the purifier mode, the nitrogen gas was cleaned from solvent vapors by an activated charcoal solvent trap (MB LMF-II) that preceded the purification system.

In order to allow the preparation of simple organic diodes, box A was equipped with a Headway Research spin-coater, a hot plate with magnetic stirrer, and a shaker. The spin-coater was inserted in the bottom plate of the glove-box. The accompanying vacuum pump and the controller of the spin-coater were situated outside of the box, ensuring easy handling via foot panel control. In addition, a 4×BNC flange was attached to box A, in order to enable simple measurements within the preparation box.

Box B, MBraun MB200-B, was used for the thermal vacuum deposition of metals and small organic molecules. The purification system was shared with box C. The glove-box could be loaded via the T-chamber, which moreover allowed an exchange with the two other boxes. In box B, two evaporators were placed. The control units and the pumps of the evaporation systems were situated outside of the glove-box, while loading occurred from the inside.

In the metal evaporator (Fig. 2.2), a vacuum of 10^{-7} mbar could be achieved using an Alcatel turbo pump with a rotary pump for backing. The pressure was detected by a Pfeifer single vacuum gauche TPG 251 A. Venting was initiated by an automatic venting mode with time delay, in order to protect the turbo pump. Subsequently, the evaporation chamber was filled with dry nitrogen gas out of the glove-box, while an automatic valve closed the vacuum line to the backing pump, thereby sealing the setup. This mode of operation allowed us to deposit even reactive

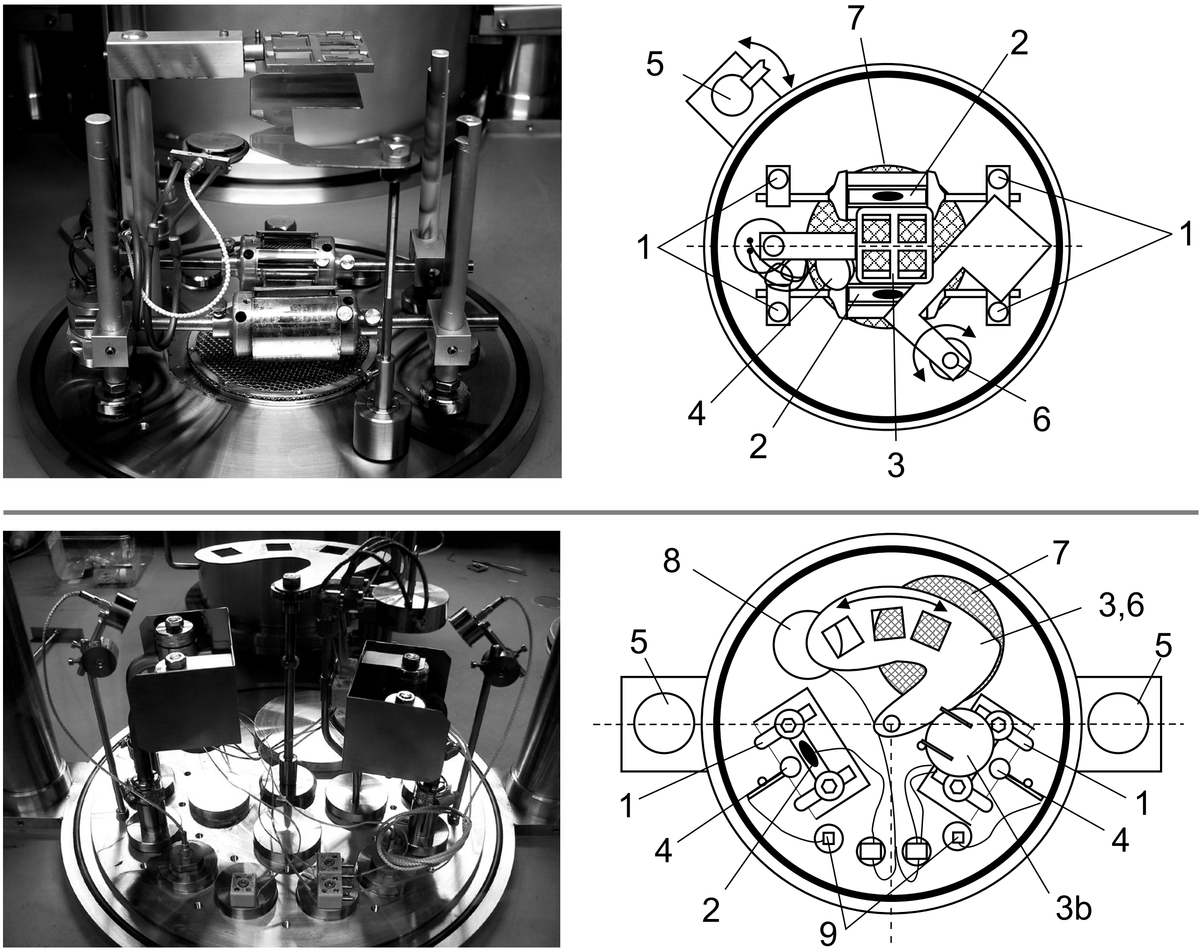

1. Power feedthrough for evaporation source
2. Evaporation source
3. Sample holder (b: temperature-controlled)
4. Quartz balance
5. Bell jar lift
6. Shutter
7. Turbo pump inlet
8. Thermocouple flange
9. Quartz balance flange

Figure 2.2 *Top*: Metal evaporator with two sources for simultaneous deposition, shutter, and quartz balance. *Bottom*: Evaporation system for the deposition of small organic molecules. Two evaporation sources with separate quartz balances and sample holders were available. The substrate temperature of one sample holder was adjustable.

metals such as calcium without any protection layer of a non-reactive metal. The metal evaporation system included two evaporation sources located at the bottom of the evaporating chamber shielded by glass tubes. As deposition sources, tungsten filaments and molybdenum boots were employed, depending on the metal to be deposited. Above the two sources, the sample holder was positioned, which could support four samples with the typical size of 2×2 cm^2. Other sample holders could be mounted as well. Next to the sample holder, a quartz balance was placed, allowing on-line measurement of the evaporation rate and thickness by an externally situated thickness monitor controller (Maxtec TM-350). In order to establish a proper deposition rate without depositing on the substrates, the quartz balance was situated below the manual shutter.

The second evaporation system was solely used for the evaporation of organic materials, mainly phenylene vinylene-type oligomers and buckminster fullerene C_{60} (Fig. 2.2). A vacuum better than 10^{-7} mbar could be achieved using a frequency-controlled Pfeiffer turbo pump with a membrane pump for backing. The pressure was detected by a single vacuum gauche (TPG 251 A). In the evaporation chamber, two evaporation systems were available. In one system, the substrate temperature could be adjusted by heating (Delta Electronika power supply SM70-22) or water-cooling. The sample was imbedded in a copper block with an evaporation window, mounted on the heating/cooling element. The second system allowed the consecutive deposition on three substrates. Evaporation occurred due to heating (Delta Electronika power supply SM15-100) of the organic material in molybdenum boots, and deposition could be started or stopped by a manual shutter. The deposition temperature of the molybdenum boots was controlled via thermocouples and a computer-controlled feedback system, which also kept the substrate temperature in the first deposition system constant. For each deposition source, a separate quartz balance traced the deposition rate and film thickness with a McVac MCM-160 thickness monitor. The venting of the organic evaporator was automated and the deposition chamber was filled with dry nitrogen gas from the glove-box.

The purpose of box C, MBraun LabMaster MB-130, was to enable electrical and optical characterization of the prepared diodes in an inert environment. Box C could be loaded by the T-ante chamber and, additionally, by a small ante chamber (MB-SCH-MINI-100-2/3-R) for small accessories. Box C was designed to ensure the characterization of simple rectifiers, LEDs, and photovoltaic cells. The characterization of such devices included, for example, current-voltage and impedance measurements, and the possibility to illuminate diodes or to read out emitted light. Therefore, the box was equipped with optical rails for sample holders and detector supports, two flanges with 4×BNC connectors, a quartz window, and a multimode optical fiber flange. The measurement equipment will be briefly described below.

2.2.1 Device preparation

The typical device structure of rectifiers, LEDs or photovoltaic cells prepared in the glove-box system is illustrated in Fig. 2.3. The devices exhibited a planar structure with the organic semiconductor sandwiched between two metals. The devices were constructed on pre-patterned, wet-cleaned indium tin oxide (ITO)-coated glass substrates of 2×2 cm^2, acting as the anode. Alternatively, other metals such as Au or Al were thermal vacuum-deposited. In some cases, poly(3,4-ethylene dioxythiophene) (PEDOT) highly doped with poly(styrene sulfonic acid) (PSS), PEDOT:PSS (Bayer Bytron P TP AI 4083), served as a hole conductor. PEDOT:PSS was spin-coated on

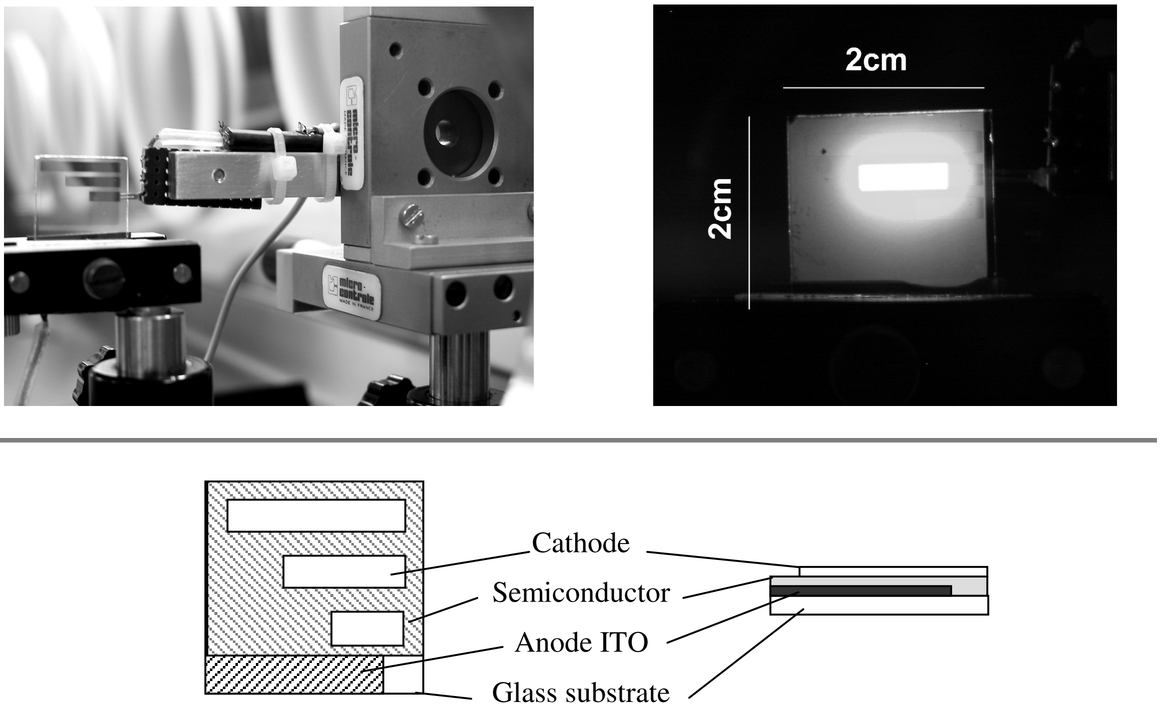

Figure 2.3 *Top, left*: Sample holder for simple electrical connection. *Top, right*: LED based on a phenylene vinylene-type oligomer under operation. *Bottom*: Design of photovoltaic cells and LEDs. One substrate included three devices of different area.

the cleaned ITO plates and dried under 10^{-4} mbar at 130°C for several minutes. Subsequently, single-layer, double-layer or blended structures of organic semiconductors were built up. Polymeric materials were spin-coated from solution and dried under dynamic vacuum, while oligomers were thermal vacuum-deposited at typically 10^{-7} mbar. Bi-layer and blended heterojunction systems of donor and acceptor materials, which are suitable for photovoltaic cells, were prepared by consecutive thermal vacuum-deposition and by co-deposition of the donor and the acceptor, respectively. Finally, a cathode metal was vacuum-deposited on the organic layer through a shadow mask. The resulting sample consisted of three independently addressable devices of different size as shown in Fig. 2.3 (device areas: 6×10^{-2} cm^2, 1.6×10^{-1} cm^2, 2.4×10^{-1} cm^2).

2.2.2 Diode characterization

The characterization of the prepared devices was performed under dry nitrogen in box C. To ensure secure handling of the small and sensitive samples in the glove-box, a suitable sample holder had to be constructed, allowing simple light read-out and an easy way to establish electrical connection (Fig. 2.3). The sample was freestanding, vertically installed in the sample holder that was mounted on an optical rail system. At the same time, the clamp holding the sample established electrical contact to the anode

(ITO). With a gold-coated tip mounted on two microtranslators, the top electrode of each individual device on the sample could be addressed. The devices were then tested upon their device properties using several measurement units.

Current-voltage (IV) and impedance measurement were performed using a Keithley 236 Source/Measure Unit and a Solatron impedance/gain-phase analyzer SI 1260, respectively. During operation of LEDs, the light output could be monitored with a calibrated photodiode making contact to the diode under investigation. The photodiode was coupled to a Labsphere SC5500 pico ampère-meter. Time-resolved electroluminescence (EL) measurements, such as EL transient measurements were performed using a Stanford Research Systems four-channel digital delay/pulse generator DG 535 in combination with an Avtech pulse amplifier AV-143B-PS. The emitted light was collected via an optical multi-mode fiber and a Hamamatzu photomultiplier. The EL signal was followed in time by a Hewlett Packard 54502A digitizing oscilloscope. Vice versa, photovoltaic cells could be illuminated by monochromatic light from a 75W Oriel Oxygen-free Xenon Lamp through a CVI Digikrom 120 monochromator. Alternatively, a Spectra Physics beam-lok argon-ion laser could be used as a light source. Via a set of mirrors and lenses, the light was focused through the quartz window into the glove-box on the addressed diode. In such a way, intensity- and wavelength-dependent measurements could be carried out. Temperature-dependent measurements were performed outside of the glove-box system with a Linkam cooling system under permanent flush of dry nitrogen. All measurements were computer-controlled and automated by home-made Test Point programs.

2.3 Electronic-test chamber imbedded in an UHV system

A powerful tool for the investigation of the dispersion of the occupied density of states in solids is photoelectron spectroscopy (PES) [17]. In this family of measurements, ultraviolet photoelectron spectroscopy (UPS) provides information on the ionization energy of organic semiconductors, but also on the workfunction of metals. Since, for example, the charge injection barrier at the metal/organic interface is dependent on these two parameters [18], UPS is a valuable technique in the field of organic diodes, providing elementary parameters that characterize the device operation. To relate the energy diagram of an organic diode to its device performance, it is essential to monitor the entire energy diagram of a diode by UPS (and preferably inverse UPS) and, finally, to probe corresponding diodes on their device performance.

One of the essential requirements for PES spectroscopy on solid films is a clean surface, since the technique is highly surface sensitive. As a consequence, PES techniques require UHV conditions as otherwise, residual moieties are immediately adsorbed on the surface, negatively affecting the measurements. In general, the establishment of UHV conditions is crucial for the combined determination of diode performance and its energy diagram. It was reported, for instance, that the contamination of a metal/organic interface prepared at UHV conditions but exposed to air at only 2 mbar resulted in a dramatic change in the relative position of the respective energy levels [16]. Hence, it is questionable whether information obtained by UPS can be extrapolated to systems prepared and handled in an atmosphere of inert gas or even air. Therefore, we attached a UHV chamber for the *in situ* electrical characterization of diodes to a PES setup. First results are outlined in *Chapter 6*.

In the following, a description of the layout of the electrical test chamber and of diodes prepared in the UHV chamber is given. The complete PES system is carefully described elsewhere [16]. The layout of the diodes prepared in the PES setup can be seen in Fig. 2.4. Ultra-flat quartz plates were used as substrates with typical dimensions of 12×8.5×0.5 mm. A RMS roughness of only 1 nm was measured by tapping mode AFM. The substrates were pre-cleaned by a wet cleaning procedure and clamped on a supporting plate under two thin metal strips. The supporting plate (stainless steel, 20×18×1 mm) attached to a three-pin bayonet joint matching the bayonet holder of the magnetic translators in the PES setup was required in order to allow transfer of samples inside the UHV system and to mount samples on the available sample holders. The substrate fixed on the supporting plate was once more wet cleaned and the metal strips were subsequently connected to the quartz plate by a small drop of silver paste. The sample was then inserted in the UHV preparation chamber, where it was dried at 110°C for one day at 10^{-9} mbar. Next, the planar diode

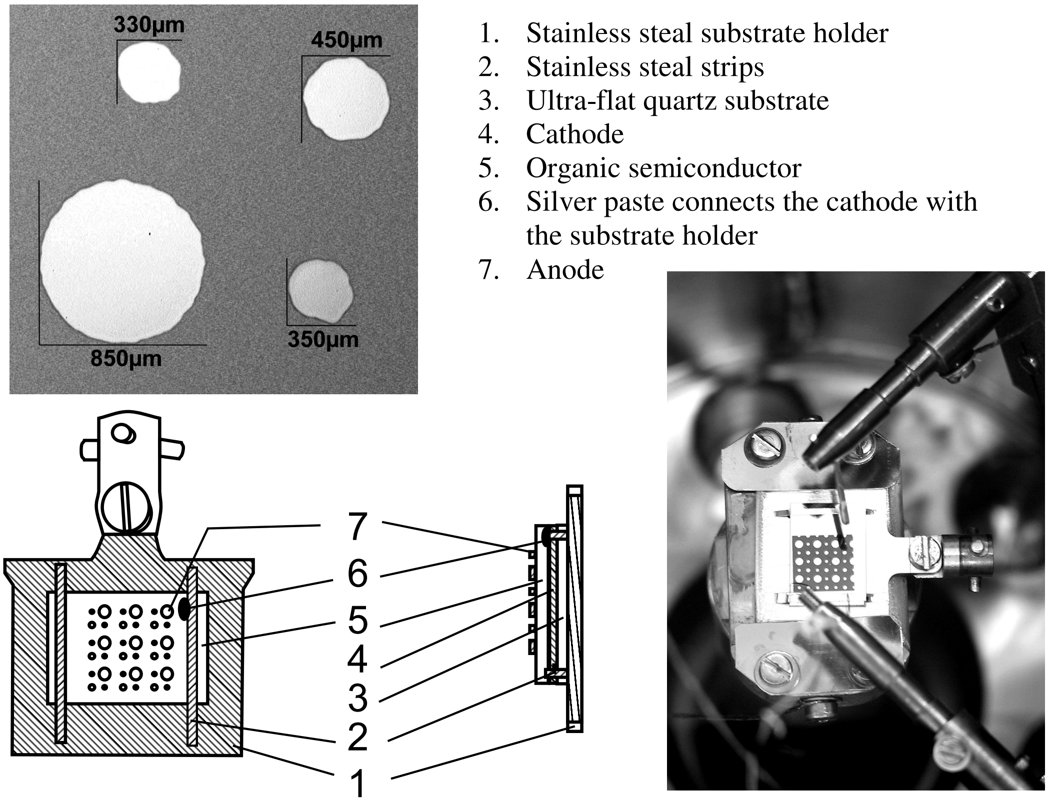

1. Stainless steal substrate holder
2. Stainless steal strips
3. Ultra-flat quartz substrate
4. Cathode
5. Organic semiconductor
6. Silver paste connects the cathode with the substrate holder
7. Anode

Figure 2.4 Organic diodes prepared under UHV and mounted in the electronic-test chamber. One substrate contains minimally 36 diodes of different sizes. The sample layout allows electrical connection via the sample holder and a gold wire.

structure was built up by thermal vacuum-deposition at a base pressure of 10^{-9} mbar. At first, a metal cathode was deposited on the entire quartz substrate without the use of a shadow mask and, hence, also on the dried drop of silver paste, thus making electrical connection between the bottom electrode and the supporting plate. Subsequently, a thin layer of small organic molecules was deposited on the obtained structure. The top electrode was finally deposited through a shadow mask, which was mounted on a mask frame. The frame including the mask could be shifted onto the support plate of the sample and the sample with mask could be moved to the metal deposition cell. The mask consisted of a thin metal foil (~25 µm) with plenty of small holes. In such a way, minimally 36 devices with three different device areas could be produced on one substrate as it can be seen from Fig. 2.4.

The devices were tested in a self-made UHV electronic-test chamber for their diode characteristics (Fig. 2.5). The electronic-test chamber was pumped with a turbo

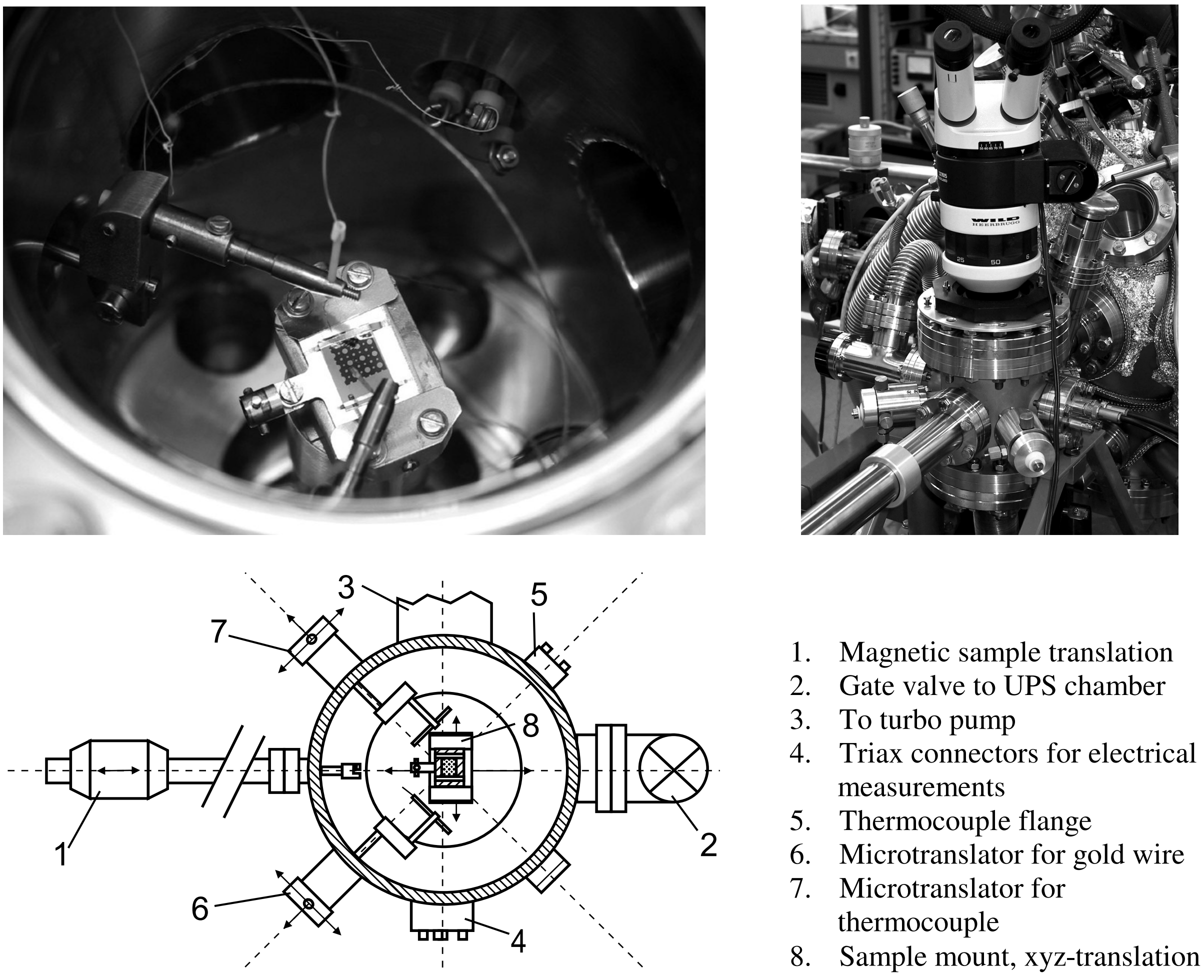

1. Magnetic sample translation
2. Gate valve to UPS chamber
3. To turbo pump
4. Triax connectors for electrical measurements
5. Thermocouple flange
6. Microtranslator for gold wire
7. Microtranslator for thermocouple
8. Sample mount, xyz-translation

Figure 2.5 Electrical test chamber implemented in a UHV system. Diodes prepared under UHV can be analyzed for their device performance under UHV conditions. *Top, left*: Inner of the electrical test chamber, showing the microtranslators that establish contact with the sample. *Top, right*: The electrical test chamber with microscope connected to a UPS/XPS chamber. *Bottom*: Scheme of the electrical test chamber.

pump and a pressure of 5×10^{-7} mbar was routinely reached. Transfer of the samples from the PES-test chamber to the electronic-test chamber was possible via a magnetic manipulator trough a 35 mm gate valve. Once the sample was transferred to the chamber, it was mounted on a sample holder, which was movable in all directions. Two different sample holders were designed. The first one allowed the illumination of the sample during IV measurements. Illumination occurred from the substrate side of the sample, i.e. through a quartz window in the sample holder. The second sample holder permitted temperature scans in a range of 100-400 K. Both sample holders were electrically isolated from the setup. The bottom electrode (cathode) of the prepared diodes was electrically connected via the support plate to the substrate holder and, in turn, the holder was attached to one connector of a 4×Triax flange. The top electrodes were addressed by a thin gold wire with a diameter of approximately 25 µm (Goodfellow, UK) fixed at a gold strip that was attached to a microtranslator. The microtranslator was insulated from the main body of the setup, but had electrical contact to another connector of the 4×Triax flange. The process of connecting the gold wire with the top electrodes of the diodes could be followed with a microscope positioned above the sample. A second microtranslator was equipped with a thermocouple that enabled us to estimate the substrate temperature. The current-voltage measurements were performed with a Kethley 6430 source/measurement unit and impedance measurements were carried out with an Agilent 4284A precision LCR meter 20 Hz-1 MHz.

2.4 Summary

We thoroughly described the design of the setups and the procedures used in this study. Part of the presented research project was the construction of a glove-box system, which implements in one single system the preparation and characterization of organic diodes in an inert environment. The layout of the constructed system, the used characterization units, and the preparation strategies of the desired diodes were outlined in this chapter. Furthermore, an electronic-test chamber was described that was attached to a PES system, combining the preparation of organic diodes and the subsequent electrical characterization under UHV conditions. The layout of the prepared diodes and the preparation protocol were given.

References

[1] S. E. Shaheen, C. J. Brabec, N. S. Sariciftci, F. Padinger, T. Fromherz and J. C. Hummelen, Appl. Phys. Lett. **78**, 841 (2001).

[2] J. H. Burroughes, D. D. C. Bradly, A. R. Brown, R. N. Marks, K. McKay, R. H. Friend, P. L. Burn and A. B. Holmes, Nature **347**, 539 (1990).

[3] H. Sirringhaus, T. Kawase, R. H. Friend, T. Shimoda, M. Inbasekaran, W. Wu and E. P. Woo, Science **290**, 2123 (2000).

[4] F. Pschenitzha and J. C. Sturm, Appl. Phys. Lett. **74**, 1913 (1999).

[5] J. A. Rogers, Z. Bao and L. Dhar, Appl. Phys. Lett. **73**, 294 (1998).

[6] T. Granlund, T. Nyberg, L. S. Roman, M. Svensson and O. Inganäs, Adv. Mater. **12**, 269 (2000).

[7] K. Yamashita, T. Mori and T. Mizutani, J. Phys. D: Appl. Phys. **34**, 740 (2001).

[8] A. Hamed, Y. Y. Sun, Y. K. Tao, R. L. Meng and P. H. Hor, Phys. Rev. B **47**, 10873 (1993).

[9] M. Yan, L. J. Rothberg, F. Papadimitrakopoulos, M. E. Galvin and T. M. Miller, Phys. Rev. Lett. **73**, 744 (1994).

[10] J. Steiger, S. Karg, R. Schmechel and H. von Seggem, Synth. Met. **122**, 49 (2001).

[11] M. Pope and C. E. Swenberg, *Electronic processes in organic crystals*, Clarendon Press, Oxford Univ. Press, New York (1982).

[12] D. Kolosov, D. S. English, V. Bulovic, P. F. Barbara, S. R. Forrest and M. E. Thompson, J. Appl. Phys. **90**, 3242 (2001).

[13] H. Ishii, K. Sugiyama, E. Ito and K. Seki, Adv. Mater. **11**, 605 (1999).

[14] S. C. Veenstra, U. Stalmach, V. V. Krasnikov, G. Hadziioannou, H. T. Jonkman, A. Heeres and G. A. Sawatzky, Appl. Phys. Lett. **76**, 2253 (2000).

[15] S. C. Veenstra, A. Heeres, G. Hadziioannou, G. A. Sawatzky and H. T. Jonkman, Appl. Phys. A: Materials Science & Processing **75**, 661 (2002).

[16] *Thesis:* S. C. Veenstra, *Electronic Structure of Molecular Systems. From Gas Phase to Thin Films to Devices*, Polymer Chemistry Rijksuniversiteit Groningen, Groningen (2002).

[17] S. Hüfner, *Photoelectron Spectroscopy Principles and Applications*, Springer Verlag, Berlin (1995).

[18] S. M. Sze, *Physics of Semiconductor Devices*, Wiley & Sons Inc., New York (1981).

3

Charge carrier injection in organic semiconductors

Abstract

In this chapter, we emphasize the crucial aspects of charge carrier transport and injection processes in disordered organic semiconductors. In particular, a phenomenological charge injection model is presented that takes charge carrier localization, polaronic effects, and disorder into account. The developed model is experimentally verified.

3.1 Introduction

To date, the device operation of rectifiers, light-emitting diodes (LEDs), and photovoltaic cells based on organic semiconductors is still not fully understood. However, in any of these applications, the dark-current-voltage relation is known to be of crucial importance for the general device performance. For this reason, there is still a strong demand for models describing the dark-current behavior even for simple systems such as planar single-layer diodes.

In general, the current-voltage (IV) characteristics of unipolar diodes based on organic materials can be understood by two basic phenomena. The current can be limited by the charge transfer rate from the metal electrode to the organic material if the energy barrier at the metal/organic interface is high. The resulting current is called injection-limited current (ILC) [1-3]. Once the injection rate is high enough to supply the bulk with sufficient charges, substantial accumulation of injected carriers may occur, resulting in a screening of the electric field and in a decrease of the drift current. In this second scenario, the current density is limited by bulk properties of the organic semiconductor, e.g. by the charge carrier mobility, and is named space-charge-limited current (SCLC) [1-4]. The SCLC is predominant in low-mobility media and is, consequently, often observed in diodes based on organic materials [5-8].

In this chapter, we focus on the unipolar charge carrier injection process from metals into organic media. In particular, we present a phenomenological injection model, wherein aspects are emphasized that dominate the charge carrier emission process. The validity of this model is inspected by comparison to experimental data. Before, charge carrier transport in organic semiconductors is briefly discussed, since this gives insight into the nature of the charge carrier injection process.

3.2 Charge carrier transport

Time-of-flight (TOF) measurements in disordered organic semiconductors exhibiting non-dispersive transport, revealed temperature-activated charge carrier mobility at low fields and field-dependent mobility at high fields, resembling the Pool-Frenkel law [9, 10]. Moreover, a decrease of mobility with increasing field above a certain threshold temperature was observed [11]. These observations are satisfied by the empirical equation proposed by Gill [12], describing the temperature and field dependence of the charge carrier mobility μ in many organic semiconductors:

Eq. 3.1
$$\mu = \mu_\infty \exp\left(-\frac{\Delta}{kT}\right)\exp\left(B\left(\frac{1}{kT}-\frac{1}{kT_0}\right)\sqrt{F}\right)$$

Here, k is the Boltzmann constant, T is the temperature, Δ is the activation energy, F is the electric field, and μ_∞, B and T_0 are parameters. The physical meanings of μ_∞, Δ, B and T_0 are still under discussion. The fact, however, that Gill's equation holds for molecular-dispersed systems as well as for a variety of intrinsic polymeric semiconductors indicates that the charge transport in polymers occurs by thermally assisted hopping of localized charge carriers [6, 7, 11, 13-16].

While in organic semiconductors the intramolecular interactions are rather strong, the intermolecular interactions are much weaker, namely van der Waals or London forces. The weak coupling between molecules even in the solid state results in narrow energy bands. Since polymeric materials exhibit weak conformational and intermolecular order, the narrow bands are easily disturbed, resulting in a system of localized states over the entire bulk material [17]. Charge carrier localization is, however, not restricted to disordered materials, and takes even place in well-ordered molecular crystals. Here, charge carrier localization stems from the fact that the polarization energy upon addition or removal of an excess charge exceeds the nearest-neighbor interaction energy, so that charges self-localize [3].

The transport of localized charge carriers within an organic semiconductor involves subsequent charge transfer steps from one localized state to another (hopping transport). Hopping transport is thermally activated and the T and F dependence of the charge carrier mobility is determined by the specificity of the elemental charge carrier hop. It was pointed out by Bässler [11] that the activation energy of the charge carrier mobility is in general determined by two factors. The first arises from the physical disparity of the otherwise chemically identical hopping sites due to disorder in the solid state, which induces a statistical dispersion of site energies. The second contribution is due to conformational changes of the molecules upon addition or removal of charges (e.g. vibronic polarons). The charge transport then requires an activation energy that is associated to the molecular deformation during individual charge transfer steps [18-21].

In the next sections, we will introduce the two most common models that describe the charge carrier transport in organic semiconductors and that emphasize the relative importance of the static disorder and the molecular deformation energy for the charge carrier transport activation energy [11, 22].

3.2.1 Bässler formalism

In the Bässler formalism, solely the static disorder energy (diagonal disorder) is regarded to be important for the charge carrier transport [11]. It is assumed that due to the presence of disorder, the transport manifold is widened into a static Gaussian distribution of localized states. This assumption is supported by the observation that absorption spectra of polymeric materials are inhomogeneously broadened to a Gaussian profile [23]. In addition to the diagonal disorder, off-diagonal disorder is introduced in Gaussian shape, taking into account variations in inter-site distances due to fluctuations of the mutual molecular orientations. Due to the fact that inter-site interactions are regarded to be weak and transport is of hopping nature, it is assumed that an inter-site charge carrier transfer rate R_{il} according to Miller-Abrahams, which was originally derived for low temperatures, can be applied close to room temperature [24]:

Eq. 3.2
$$R_{\mathrm{il}}(E_{\mathrm{l}},E_{\mathrm{i}},x)=\nu_0\exp(-2\gamma|x_{\mathrm{i}}-x_{\mathrm{l}}|)\begin{cases}\exp\left(-\dfrac{E_{\mathrm{l}}-E_{\mathrm{i}}}{kT}\right) & ;E_{\mathrm{l}}>E_{\mathrm{i}}\\ 1 & ;E_{\mathrm{l}}<E_{\mathrm{i}}\end{cases}$$

Here, ν_0 is the attempt frequency to hop, E_{i} is the site energy of the occupied site *i* and E_{l} of the initially unoccupied site *l*, and γ is the inverse localization radius of the charge carriers. The first exponential term in Eq. 3.2 describes the decay of the electronic wavefunction of a charge located at site *i* at the distance $|x_{\mathrm{i}}-x_{\mathrm{l}}|$. Jumps upwards in energy are impeded by the energy barrier that charge carriers need to overcome, while downward jumps are independent from the matching of the site energy difference and the phonon energy.

Monte Carlo simulations on the charge carrier transport considering the described model showed that transport involved charge carriers relaxed to a transport state being $-\sigma^2/\mathrm{kT}$ below the center of the density of states (DOS) distribution with width σ. As a consequence, the Fermi-Dirac statistics in the Bässler formalism is broken, resulting in an enrichment of charge carriers in the vicinity of the transport level. This fact complicates the interpretation of field effect mobilities, considering their density dependence. The temperature and field dependence of the charge carrier mobility in a hopping system with diagonal and weak off-diagonal disorder of Gaussian shape is given by an empirical equation for high fields:

Eq. 3.3
$$\mu_{GDM}=\mu_\infty\exp\left[-\left(\frac{2\sigma}{3kT}\right)^2+C\left(\left(\frac{\sigma}{kT}\right)^2-2.25\right)\sqrt{F}\right]$$

with $C = 2.9\ 10^{-4}\ (\mathrm{cm/Vs})^{1/2}$. From Eq. 3.3 we see that the activation energy Δ of the charge carrier mobility is temperature-dependent and is related to the diagonal disorder-induced DOS width. Experimental results indeed unveiled a mismatch between the temperature dependence of the charge carrier mobility and Arrhenius behavior, and showed a reciprocal square dependence of $\ln\mu$ with T [25, 26]. Taking long-range interactions such as dipole-dipole coupling into account, the charge carrier mobility was approximated to [27]:

Eq. 3.4
$$\mu_{CDM}=\mu_\infty\exp\left[-\left(\frac{3\sigma}{5kT}\right)^2+0.78\left(\left(\frac{\sigma}{kT}\right)^{\frac{3}{2}}-2\right)\sqrt{\frac{qaF}{\sigma}}\right]$$

where *a* is the inter-site spacing and *q* is the electron charge. The so-called correlated Gaussian disorder model (CDM) reveals a different temperature dependence of the charge carrier mobility in comparison to the Gaussian disorder model, which matches the experimental observations better [25].

3.2.2 Small polaron model

In the small polaron model, the static disorder energy plays no significant role if compared to the intramolecular deformation energy [22]. The strong electron-phonon coupling results in self-localization of the charge carriers and, hence, charge carrier transport is regarded to be of hopping type. In this frame, the Marcus rate equation is believed to be suitable to describe the field dependence of the charge transport process [28, 29]. The Marcus rate for a transition from site *i* to site *l* under high-temperature regime is:

Eq. 3.5

$$R_{\mathrm{il}} \propto \frac{1}{\sqrt{E_{\mathrm{r}}T}} \exp\left[-\frac{(E_{\mathrm{l}} - E_{\mathrm{i}} + E_{\mathrm{r}})^2}{4E_{\mathrm{r}}kT}\right]$$

where E_r is the intramolecular reorganization energy, typically being in the range of 0.3 eV [30]. Eq. 3.5 describes the transition rate at the intersection of the two parabolic free energy curves of the donor and the acceptor sites involved in the hopping process. Hopping transport is then regarded to be a one-step process, allowing only hops between adjacent sites in a one-dimensional uniformly spaced chain of hopping sites. The dependence of the mobility on *F* and *T* in the frame of the Marcus theory is given by:

Eq. 3.6

$$\mu = \mu_0 \exp\left[-\frac{E_{\mathrm{r}}}{4kT} - \frac{(qFa)^2}{4E_{\mathrm{r}}kT}\right] \frac{2kT\mathrm{Sinh}\left[\frac{qFa}{2kT}\right]}{qaF}$$

where μ_0 is slightly temperature-dependent [29, 30]. The mobility derived from the Marcus theory is constant for low fields and increases exponentially at high fields. For very high fields or low reorganization energies, the mobility tends to decrease with increasing field. This behavior is related to the Marcus inverted region, a signature of polaronic transport [31]. For high reorganization energies, Eq. 3.6 finally transforms to the well-known Bagley equation [32]. The main limitation of the small polaron theory is the fact that the field dependence of the charge carrier mobility does not coincide with the one observed for most organic semiconductors. On the other hand, the dependence of the charge carrier mobility on the hopping site density is well described [22].

It is obvious that for amorphous polymeric or polycrystalline oligomeric materials, the relative contribution of polaronic or disorder effects will vary. Seki *et al.* recently included local and long-range diagonal disorder in the frame of the Marcus theory [30]. It became apparent that upon inclusion of diagonal disorder, the field dependence of the charge carrier mobility becomes much stronger in the low-field regime, exhibiting an $\ln\mu$ versus $\sqrt{F}$ dependence. This indicates that Gill's phenomenologically derived equation is a result of disorder effects influencing the charge carrier transport.

3.3 Emission-limited injection into a trap-free transport hopping system

Charge carrier injection from a metal to an organic semiconductor is still an issue of scientific discussion. Similar to charge carrier transport, charge carrier injection is strongly influenced by the characteristics of organic media, namely strong charge carrier localization, hopping type of transport, diagonal and off-diagonal disorder, and polaronic effects. Classically, charge injection into semiconductors is described by the thermionic emission theory of Bethe [33], where thermally activated charge carriers in the metal can overcome the offset in the energy levels between metal and semiconductor and freely propagate in the semiconductor. However, it was realized that in low mobility materials, the thermionic emission theory is not applicable, since the large concentration of the injected charges close to the metal/semiconductor interface induces substantial charge backflow [34]. This was encountered in the diffusion-limited injection model, which predicts an injection current density proportional to the charge carrier mobility. However, the classical models lack the fact that in organic semiconductors, especially in highly disordered polymers, the charge carrier transport is no longer a free propagation of charges in extended states but rather a hopping between localized states. The hopping nature of the charge carrier transport was introduces lately by assuming a charge carrier injection process based on thermally assisted tunneling from the metal into a uniformly spaced chain of localized states [35], but disorder effects and the Coulombic potential were ignored. Charge carrier injection into a disordered hopping system was furthermore intensively studied by Monte Carlo simulations [36-38]. Recently, an analytical treatment of the injection process from a metal into a disordered hopping system was proposed regarding the charge emission as a first rate-limiting jump from the metal to the semiconductor, which is followed by either a diffusive escape from the interface or backflow to the electrode [39]. This model has been investigated by Monte Carlo simulations [40] and was verified experimentally for small molecules and polymers [39, 41].

Alternative to the existing injection models for organic media, we phenomenologically describe the injection process as a thermal activation of charges in the metal, leading to an occupation of the first mono-layer of the semiconductor according to the Boltzmann distribution. Subsequently, the emitted charges have to escape the metal electrode by nearest neighbor hopping events. With this model, we followed the concept proposed by Abkowitz *et al.* [35] in the first place. Here, both the charge injection and further charge transport are described as thermally assisted hopping events in a one-dimensional uniformly spaced chain of hopping sites. The model is, therefore, fully consistent with the hopping nature of charge transport, using no further simplifications. This, however, does not allow us to consistently implement disorder effects. Disorder is thus excluded in the first place, but will be later introduced in a phenomenological way. Moreover, the model ignores any space-charge effects and, hence, cannot describe the transition to SCLC. As a consequence, the applicability of the model for devices with typical thickness and operational voltage is limited to barrier heights larger than 0.3 eV [42].

The energy diagram of a metal/semiconductor contact is sketched in Fig. 3.1. The metal Fermi-level is situated in the band gap of the organic semiconductor, which results in a potential barrier that charge carriers have to overcome or to tunnel through in order to be injected into the semiconductor. However, the potential energy shape close to the metal/semiconductor interface is strongly affected by the metal/semiconductor interaction. In particular, the electronic polarization of the metal upon addition of a charge carrier to a molecule close to the contact results in an energy change of the respective site, which is classically described by the image charge potential [1]. In general, the interaction between charges in the semiconductor and the metal has an important consequence. When an electric field is applied, the potential energy of a charge at the distance x from the metal surface is given by the sum of the image charge and the electrostatic potentials:

Eq. 3.7

$$PE(x) = \phi - \frac{q}{16\pi\varepsilon_s x} - Fx$$

where ϕ is the difference of the workfunction of the metal and the electron affinity of the organic semiconductor, and ε_s is the permittivity of the semiconductor. The summation of electrostatic and image charge potentials yields a lowering of the energy barrier height upon increased field, called Schottky lowering, and, concomitantly, a lateral shift of the maximum of the barrier [1]. The Schottky lowering and the position of the barrier maximum relative to the metal/semiconductor interface is given by the

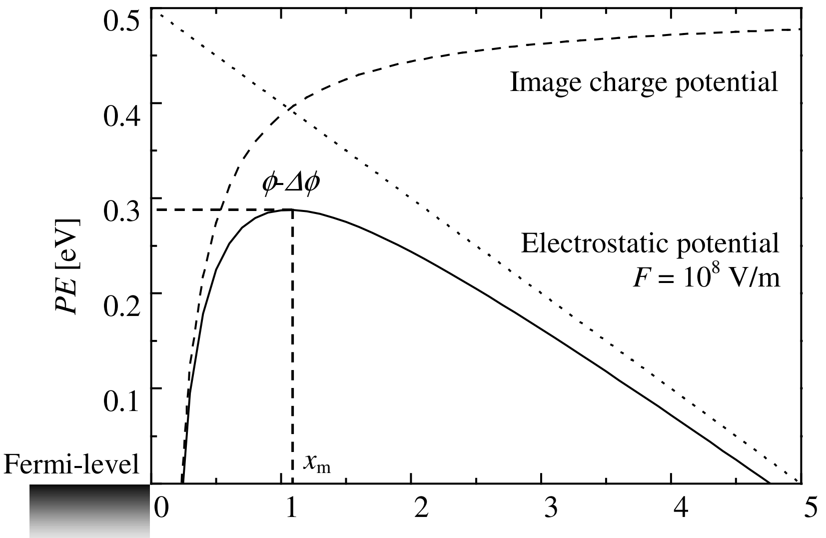

Figure 3.1 Potential energy versus distance of charge carriers situated in a semiconductor close to a metal contact

condition $\partial PE(x)/\partial x = 0$:

Eq. 3.8
$$x_m = \sqrt{\frac{q}{16\pi\varepsilon_s F}} \qquad [\mathrm{m}]$$

Eq. 3.9
$$\Delta\phi = \sqrt{\frac{qF}{4\pi\varepsilon_s}} \equiv \beta_S \sqrt{F} \qquad [\mathrm{eV}]$$

We define β_S as the Schottky parameter. Unlike Abkowitz *et al.*, we include the image charge potentials for both contacts in the description of the injection process. Hence, the energies of the transport-involved sites follow:

Eq. 3.10
$$PE(x) = \phi - Fx - \frac{q}{16\pi\varepsilon_s x} - \frac{q}{16\pi\varepsilon_s (d-x)}$$

where d is the film thickness of the organic semiconductor.

We describe the rate at which a charge carrier occupying the state i moves to the empty state l in terms of the classical Marcus theory for the high-temperature limit, introducing the reorganization energy E_r:

Eq. 3.11
$$R_{\mathrm{il}} \propto \exp\left[-2\gamma\left|x_{\mathrm{i}} - x_{\mathrm{l}}\right|\right]\exp\left[-\frac{(E_{\mathrm{l}} - E_{\mathrm{i}} + E_{\mathrm{r}})^2}{4E_{\mathrm{r}}kT}\right]$$

The rate for the charge transfer from the electrode metals to the semiconductor is given by a similar equation:

Eq. 3.12
$$R_{\mathrm{mi}} \propto \exp\left[-2\gamma\left|x_{\mathrm{m}} - x_{\mathrm{i}}\right|\right]\exp\left[-\frac{E_{\mathrm{i}} - E_{\mathrm{m}}}{2kT}\right]$$

In general, the hopping rate from state i to l is the product of the probability Π_{i} to find a charge carrier at site i, the probability to have site l non-occupied ($1-\Pi_{\mathrm{l}}$), and the rate at which a charge carrier occupying the state i moves to the empty state l. In order to obtain the occupation probabilities of all sites, the principle of detailed balance is used as steady-state condition. This principle requires the number of hops towards a certain site i to be equal to the number of hops leaving the same site. The spatial distribution of sites is set to be equidistant with the inter-site hopping distance a. The first and the last mono-layer have, however, a distance a' from the metal surface, not necessarily being equal to a. The concept of detailed balance leads to the following set of equations:

Eq. 3.13
$$\sum_m (1-\Pi_i)R_{mi} + \sum_{l\neq i} R_{li}\Pi_l(1-\Pi_i) = \sum_m \Pi_i R_{im} + \sum_{l\neq i} R_{il}\Pi_i(1-\Pi_l)$$

for $m = 1, 2$ and $i, l = 1,\ldots, \mathrm{N}$

where N is the number of hopping sites. We assume that the electrode metals are perfect sources for charges, but at the same time they provide an excess of empty sites where charges can tunnel into. Moreover, we approximate all probabilities to find an empty site in the organic semiconductor to be one, since the occupation probability for each remaining site *i* is small in the injection-limited case.

The current density can be calculated by counting hopping events across any plane in the material:

Eq. 3.14
$$j_i \propto \sum_{l=1}^{N}\sum_{k=0}^{l-1} l\left(\Pi_{i-k} R_{i-k,i-k+l} - \Pi_{i-k+l} R_{i-k+l,i-k}\right)$$

where *l* is the number of sites separating two transport-involved hopping sites, and *k* is an index over equal distance hops. Due to the principle of detailed balance, the current is independent of the position *i* of the chosen plane in the semiconductor.

The purpose of the following sections is to stress the important aspects in the charge injection process and to adapt the presented model on basis of these considerations to experimentally obtained data.

3.3.1 Charge carrier localization

We now assume that the charge carrier injection process is adequately described by the emission of charge carriers from the metal to the first mono-layer of a disordered organic semiconductor and further nearest neighbor hopping events, neglecting multiple hops [35], thermionic emission to deeper states in the semiconductor, or direct tunneling through the potential barrier [43]. We believe that this especially holds for amorphous organic semiconductors, where charges are strongly localized. This assumption is based on the fact that the localization radius $1/\gamma$ is typically in the range of 1 Å, which decreases the hopping rate for long-distance hops. The thermally stimulated injection from the metal to deeper states in the organic semiconductor or even direct tunneling through the potential barrier is, hence, rather unlikely. This is in accordance to the results of Arkhipov *et al.* [38-40, 44], who modeled charge injection from a metal to disordered organic semiconductors. In their model, the current density is mainly established by initial jumps to sites close to the metal followed by continuous drift-diffusion motion over the potential barrier, avoiding recombination with image charges. Due to the weak extension of the electronic wavefunction of the metal charges into the semiconductor, and since a Miller-Abrahams rate was used to describe the first jump (Eq. 3.2), direct tunneling or emission to deeper states in the semiconductor is strongly suppressed. From Eq. 3.12 and 3.13 it becomes apparent that in the all-hopping model presented here, small localization radii result in an occupation probability of the first mono-layer, which is given by the Boltzmann factor. At this point, our model essentially differs from the assumption made in the disorder model proposed by Arkhipov, namely that a charge carrier situated in the first mono-layer will perform a fast jump back to the metal, resulting in a charge carrier density in the first mono-layer equal to zero.

Out of the same reasoning, multi-site hopping plays merely a weak role in the charge carrier transport process. Only in regions of extremely high fields, multiple hops or emission from the metal to deeper layers in the semiconductor influence the charge carrier distribution because of the interplay between energetical and lateral decay functions in the rate equation. Nonetheless, this regime is mostly not practical and can safely be ignored. In Fig. 3.2, it is demonstrated that indeed a perfect agreement between the models including and excluding multi-site hops is achieved once a typical localization radius is chosen.

How does the developed model finally compare to experimental data? In Fig. 3.3, we compare simulated and experimental dark-current densities versus the electric field of single-layer diodes based on (*E*,*E*,*E*,*E*)-1,4-bis[(4-styryl)styryl]-2-methoxy-5-(2'-ethyl-hexyloxy)benzene (MEH-OPV5) in an ITO/MEH-OPV5/Al structure (ITO, indium tin oxide). The diodes were biased in forward direction (holes are emitted from ITO). The measured current densities are believed to be injection-limited and a proof is given in *Chapter 4*. The field was corrected for the built-in field, which has been estimated from the transition from diffusion-controlled to injection-controlled current densities. It is striking that sufficiently good agreement between experimental data and simulations could be achieved at room temperature by just regarding the charge carrier

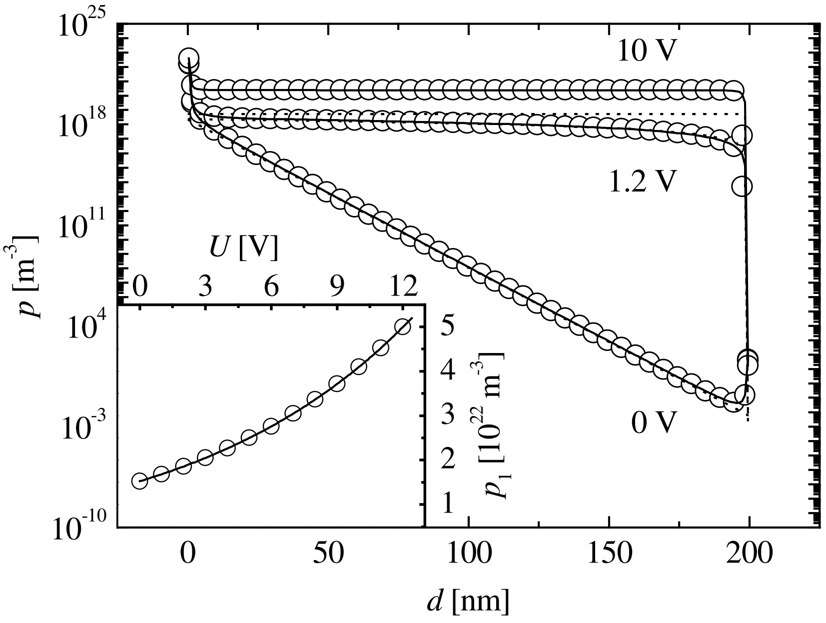

Figure 3.2 Simulated charge carrier density distribution, assuming thermally assisted hopping in a one-dimensional uniformly spaced chain of hopping sites. Emission is achieved by either introducing a rate for a jump from the metals to each state in the organic semiconductor and vice versa and further multi-site hopping transport (○), or by the establishment of a Boltzmann occupation in the first monolayer and further nearest neighbor hopping events (—). The dotted line simulates the charge carrier density excluding image charge potential. The insert shows the charge carrier density of the first monolayer close to x = 0 nm (injection barrier height ϕ_1) for both models. Parameters are: $\phi_1 = 0.5$ eV, $\phi_2 = 1.7$ eV, $a = 1$ nm, $a' = 0.5$ a, $\gamma = 10^{10}$ m^{-1}, $E_r = 0.3$ eV, $\varepsilon = 3.2$, $d = 200$ nm, and $T = 293$ K.

emission from the metal to the organic as the establishment of a Boltzmann occupation of the first mono-layer and further transport by nearest neighbor hopping events, using reasonable parameters. Schottky lowering is naturally required. Hence, in the description of the charge carrier injection process from a metal to a disordered organic semiconductor, multi-site transport steps can be ignored.

3.3.2 Charge carrier transport

The in Fig. 3.3 presented experimental IV–characteristic of an injection-limited diode compares well with the simulations proposed in section 3.3.1. Only at higher fields, the simulated current densities were underestimated. Of course, better fits can be achieved including multi-site hopping, but an unreasonably large localization length of about 3 Å is required. Multi-site hopping is, hence, not a possible explanation for the mismatch at higher fields.

Still, upon inclusion of multi-site hopping, the field dependence increases. This is due to a change of the charge carrier mobility, which is of Marcus type when solely

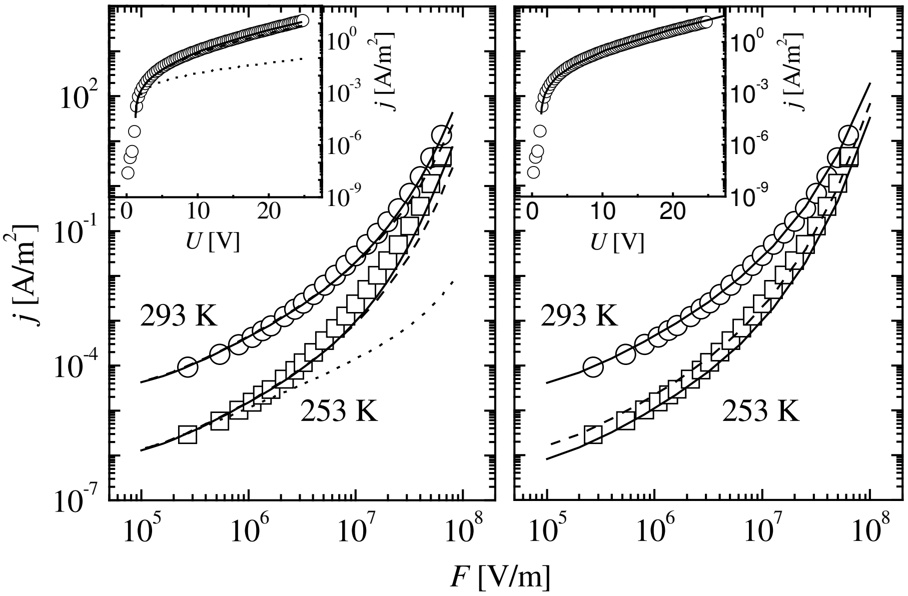

Figure 3.3 *Left*: IV-characteristic of an ITO/MEH-OPV5/Al device (○, □). (—) is a fit using multi-site hopping and counting the hopping events through any plane in the device. The localization radius was found to be 3 Å. (---) is a fit regarding only nearest neighbor hopping events and a Boltzmann occupation of the first monolayers. In (···) Schottky lowering is excluded. *Right*: IV-characteristic of an ITO/MEH-OPV5/Al device (○, □). (—) is a fit using the drift-diffusion current equation and the mobility in the frame of the CDM, whereas (---) is a fit using a slightly reduced barrier height. $\varepsilon = 3.2$, $E_r = 0.3$ eV, $d = 370$ nm, $a = 1$ nm, $a' = 0.5$ a, $\phi = 0.5$ eV, $N_V = 0.9\ 10^{27}$ m^{-3}, $\mu_\infty = 1.3\ 10^{-8}$ m^2/Vs, and $\sigma = 0.06$ eV.

nearest neighbor hopping events are assumed. In organic semiconductors of poor order, however, the field and temperature dependence of the charge carrier mobility is strongly influenced by the diagonal and off-diagonal disorder as it was shown by Seki *et al.* and, usually, it can be better described in the frame of the correlated Gaussian disorder model than in the frame of the Marcus theory [27, 30]. Therefore, the inclusion of multi-site hopping with weak localization in the hopping model might artificially mimic the field dependence of a charge carrier mobility dominated by disorder. Apparently, it is required to introduce the charge carrier mobility independent to the proposed model, which we do by exchanging the current equation 3.14 with the standard drift-diffusion expression for the current density:

Eq. 3.15
$$j_{\mathrm{h}}(x) = q\mu_{\mathrm{h}} p(x) F - kT\mu \frac{\partial p(x)}{\partial x}$$

Here, p is the density of free holes. The current is approximated by assuming the charge carrier density to be equal to the density of states N_{V} multiplied with the occupation probability obtained by detailed balance, $p_{\mathrm{i}} = N_{\mathrm{V}}\Pi_{\mathrm{i}}$. We estimated N_{V} to be equal to the molecular density. Obviously, the current densities are comparatively sensitive to the transport model used. Of course, a perfect agreement of current density using the drift-diffusion equation (Eq. 3.15) and the charge carrier mobility in the frame of the Marcus theory (Eq. 3.6) is obtained with current densities calculated by Eq. 3.14. Once, however, the CDM mobility (Eq. 3.4) is used, the modeled current-voltage relationship perfectly fits to the experimental data over orders of magnitude in current density and electric field, requiring the field activation factor of the charge carrier mobility and the zero field charge carrier mobility to be very close to the ones independently measured by transient electroluminescence measurements (see *Chapter 4*). This result indicates that the IV–characteristic of an ITO/MEH-OPV5/Al diode is strongly biased by the disorder prevailing in the organic semiconductor, which is, moreover, reflected in the temperature dependence of the charge carrier injection current [39, 41].

3.3.3 Disorder effect

We now discuss the temperature dependence of the observed current densities. Since no information on the temperature activation of the charge transport is available, the following remains a qualitative discussion. So far, the temperature activation of the current could not be described properly as it can be seen from Fig. 3.3 and 3.4. Nevertheless, the temperature dependence of the current densities could be met by slightly reducing the barrier height for lower temperatures (Fig. 3.3). This is likely to be the result of the apparently existing diagonal disorder in the MEH-OPV5 film. It has been shown by Monte Carlo simulations that the presence of diagonal disorder results in an effective temperature dependent energy barrier lowering and, hence, in a weak temperature dependence of the injection current densities at low temperatures [38, 44]. This effect was identified in several oligomer- and polymer-based diodes [39, 41, 44] and was considered by Arkhipov *et al.* in an analytical charge injection model [39]. In this model, the injection process is described by a first rate-limiting hop from the metal to the DOS of the semiconductor, followed by a continuous drift-diffusion motion of the injected charge carriers trying to escape their image twin. Accordingly, we now phenomenologically describe the charge carrier emission to be a jump from the Fermi-level of the metal to a disorder-broadened DOS of the first mono-layer rather than to a monoenergetic site. Injection in deeper layers is ignored due to the reasons explained before. The occupation probability in the first mono-layer is then given by the interplay between the normalized DOS function $g(E)$ of the first mono-layer

Eq. 3.16 $$g(E)=\frac{1}{\sqrt{2\pi}\sigma}\exp\left[-\frac{E^2}{2\sigma^2}\right]$$

which is typically taken in a Gaussian form with width σ, and the Fermi-Dirac distribution:

Eq. 3.17 $$\Pi_1=\int_{-\infty}^{\infty}\frac{1}{1+\exp\left[\frac{E}{kT}\right]}g(PE(a')-E)\partial E \overset{PE(a')>\frac{q\sigma^2}{kT}}{\approx} \exp\left[-\frac{q}{kT}\left(PE(a')-\frac{q\sigma^2}{2kT}\right)\right]$$

The result of Eq. 3.17 implies that the potential at *a*’ is shifted to lower energies by a temperature-dependent factor. In a sense, we then argue in accordance to Arkhipov *et al.* [39, 40] that upon the initial jump from the metal to the organic material, the transport level is established as the mean occupation energy. Further transport is, therefore, independent of the total site energy and is described as a sequence of nearest neighbor hopping events. Consequently, all site energies can be regarded to be shifted to lower energies by the same factor, resulting in an effective lowering of the injection barrier.

From Eq. 3.17, it becomes clear that upon inclusion of diagonal disorder the temperature dependence of the occupation probability is weakened for low temperatures, and the current no longer exhibits an Arrhenius type of temperature activation, which is in good agreement with the experimental results (Fig. 3.4). Best correspondence with experimental data could be obtained by introducing an interfacial disorder width that is slightly larger than the one of the bulk, which might result from the approximate calculation of Eq. 3.17. However, especially for oligomeric materials, it is reasonable that the diagonal disorder at the metal/organic interface can differ from the diagonal disorder in the bulk. Moreover, it has been reported that the Gaussian DOS of organic semiconductors broadens close to metal contacts [45]. Nonetheless, the rather strong temperature dependence of the injection current density (Fig. 3.4) resulted in disorder energies too small for organic materials, once a reasonable hole injection barrier height at the MEH-OPV5/ITO interface was chosen. Typically disorder energies of 100 meV even for solids based on small molecules [44] are found. The small disorder energy might originate from the crystalline nature of the material used. Applying the disorder model proposed by Arkhipov *et al.* [39], an even lower disorder energy (larger barrier height) is required for the same barrier height (disorder energy). This stems from the fact that in our injection model, in contrast to the one of

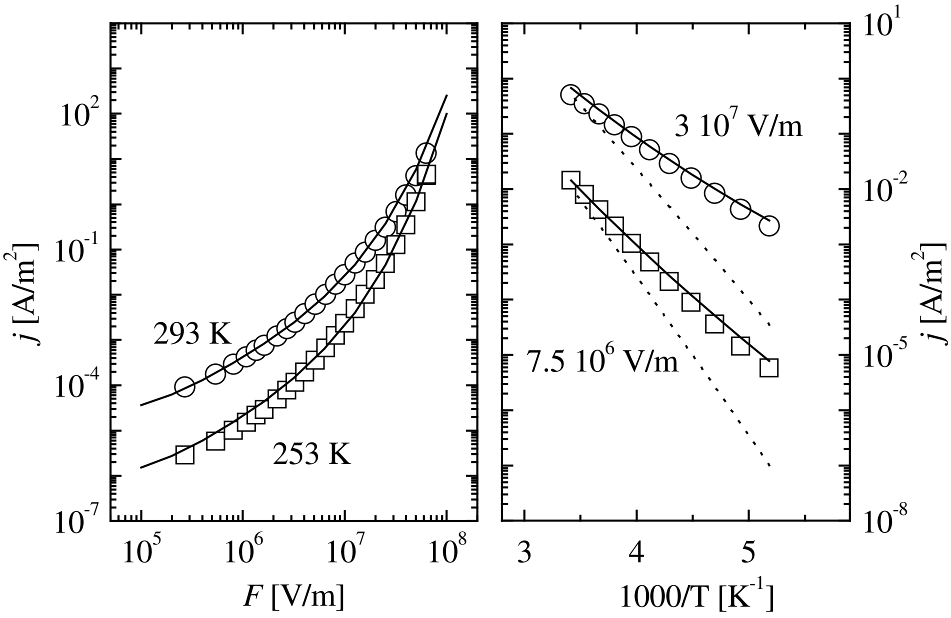

Figure 3.4 *Left*: IV-characteristic of an ITO/MEH-OPV5/Al device (○, □). (—) is a fit using the drift-diffusion current equation and the mobility in the frame of the CDM. In addition, energy disorder-induced lowering of the potential energy is included. *Right*: Arrhenius plot of the current density of an ITO/MEH-OPV5/Al device (○, □). (—) is a fit using the drift-diffusion current equation and the mobility in the frame of the CDM. In addition, energy disorder-induced lowering of the potential energy is included. (···) is the result upon exclusion of energy disorder. $\varepsilon = 3.2$, $E_r = 0.3$ eV, $d = 370$ nm, $a = 1$ nm, $a' = 0.5$ a, $\phi = 0.65$ eV, $N_V = 0.9\ 10^{27}$ m^{-3}, $\mu_\infty = 1.3\ 10^{-8}$ m^2/Vs, $\sigma = 0.06$ eV, and $\sigma = 0.08$ eV (interfacial).

Arkhipov, a noticeable mobility activation energy contributes to the temperature dependence of the injection current density (Eq. 3.15).

3.4 Conclusion

In this chapter, we introduced a charge carrier injection model, which describes the charge carrier emission from a metal to an organic semiconductor by thermally assisted hopping in a one-dimensional uniformly spaced chain of hopping sites. On basis of this model, we demonstrated that the charge injection from a metal to an organic semiconductor is dominated by the establishment of the charge carrier density in the first mono-layer according to the Boltzmann statistics and by further nearest neighbor hopping events. Comparison of the injection model with experimental data obtained for ITO/MEH-OPV5/Al cells revealed the importance of disorder effects, which were introduced in a phenomenological way to the model. Perfect agreement of the simulated IV–characteristics with the experimental data was obtained, which justifies the proposed charge injection model.

References

[1] S. M. Sze, *Physics of Semiconductor Devices*, Wiley & Sons Inc., New York (1981).

[2] K. C. Kao and W. Hwang, *Electrical transport in solids with particular reference to organic semiconductors*, Pergamon Press, Oxford (1981).

[3] M. Pope and C. E. Swenberg, *Electronic processes in organic crystals*, Clarendon Press, Oxford Univ. Press, New York (1982).

[4] N. F. Mott and R. W. Gurney, *Electronic Processes in Ionic Crystals*, Univ. Press, Oxford (1940).

[5] W. Brütting, S. Berleb and A. G. Mückel, Synth. Met. **122**, 99 (2001).

[6] L. Bozano, S. A. Carter, J. C. Scott, G. G. Malliaras and P. J. Brock, Appl. Phys. Lett. **74**, 1132 (1999).

[7] P. W. M. Blom, M. J. M. de Jong and J. J. M. Vleggaar, Appl. Phys. Lett. **68**, 3308 (1996).

[8] S. Forero, P. H. Nguyen, W. Brütting and M. Schwoerer, Phys. Chem. Chem. Phys. **1**, 1769 (1999).

[9] H. H. Pool, Philos. Mag. London, Edinb., and Dublin **33**, 112 (1916).

[10] J. Frenkel, Phys. Rev. **54**, 647 (1938).

[11] H. Bässler, Phys. Stat. Sol. B **175**, 15 (1993).

[12] W. D. Gill, J. Appl. Phys. **43**, 5033 (1972).

[13] E. M. Cornwell, Phys. Rev. **103**, 51 (1956).

[14] N. F. Mott, Can. J. Phys. **34**, 1356 (1956).

[15] Y. Shen, M. W. Klein, D. B. Jacobs, J. C. Scott and G. G. Malliaras, Phys. Rev. Lett. **86**, 3867 (2001).

[16] H. J. Yuh and D. M. Pai, Molec. Cryst. Liq. Cryst. **183**, 217 (1990a).

[17] P. W. Anderson, Phys. Rev. **109**, 1492 (1958).

[18] W. J. Siebrand, J. Chem. Phys. **41**, 3574 (1964).

[19] R. W. Munn and W. J. Siebrand, J. Chem. Phys. **52**, 47 (1970).

[20] E. A. Silinsh and A. J. Jurgis, Chem. Phys. **94**, 77 (1985).

[21] N. Sato, H. Inokuchi and E. A. Silinsh, Chem. Phys. **115**, 269 (1987).

[22] P. M. Borsenberger and D. S. Weiss, *Organic photoreceptors for imaging systems*, Marcel Dekker, Inc., New York (1993).

[23] K. D. Rockwitz and H. Bässler, Chem. Phys. **70**, 307 (1982).

[24] A. Miller and J. D. Abrahams, Phys. Rev. **120**, 745 (1960).

[25] H. C. F. Martens, P. W. M. Blom and H. F. M. Schoo, Phys. Rev. B **61**, 7489 (2000).

[26] P. M. Borsenberger, L. T. Pautmeier and H. Bässler, J. Chem. Phys. **94**, 5447 (1991a).

[27] S. V. Novikov, D. H. Dunlap, V. M. Kenkre, P. E. Parris and A. V. Vannikov, Phys. Rev. Lett. **81**, 4472 (1998).

[28] R. A. Marcus and N. Sutin, Biochim. Biophys. Acta **811**, 265 (1985).

[29] D. Emin, Adv. Phys. **24**, 305 (1975).

[30] K. Seki and M. Tachiya, Phys. Rev. B **65**, 1 (2001).

[31] R. A. Marcus, Rev. Mod. Phys. **65**, 599 (1993).

[32] B. G. Bagley, Solid State Commun. **8**, 345 (1970).

[33] H. A. Bethe, MIT Radiat. Lab. Rep. **43**, 12 (1942).

[34] J. G. Simmons, Phys. Rev. Lett. **15**, 967 (1965).

[35] M. A. Abkowitz, H. A. Mizes and J. S. Facci, Appl. Phys. Lett. **66**, 1288 (1995).

[36] Y. N. Garstein and E. M. Conwell, Chem. Phys. Lett. **255**, 93 (1996).

[37] E. M. Conwell and M. W. Wu, Appl. Phys. Lett. **70**, 1867 (1997).

[38] U. Wolf, V. I. Arkhipov and H. Bässler, Phys. Rev. B **59**, 7507 (1998).

[39] V. I. Arkhipov, E. V. Emelianova, Y. H. Tak and H. Bässler, J. Appl. Phys. **84**, 848 (1998).

[40] V. I. Arkhipov, U. Wolf and H. Bässler, Phys. Rev. B **59**, 7514 (1999).

[41] T. van Woudenbergh, P. W. M. Blom, M. C. J. M. Vissenberg and J. N. Huiberts, Appl. Phys. Lett. **79**, 1697 (2001).

[42] P. W. M. Blom and M. C. J. M. Vissenberg, Mater. Sci. Eng. **27**, 53 (2000).

[43] R. H. Fowler and L. Nordheim, Proc. Roy. Soc. **119**,173 (1928).

[44] S. Barth, U. Wolf, H. Bässler, P. Müller, H. Riel, H. Vestweber, P. F. Seidler and W. Rieß, Phys. Rev. B **60**, 8791 (1999).

[45] M. A. Baldo and S. R. Forrest, Phys. Rev. B. **64**, 085201 (2001).

4

Unipolar organic diodes and disorder effects

Abstract

The charge carrier transport in disordered polymeric semiconductors is governed by its hopping nature and the disorder-induced energy dispersion of the hopping sites. This energy dispersion is related to fluctuations in the intermolecular arrangement and to intramolecular disparities in the presence of molecular imperfections, length or conformation in the solid state. In contrast, oligomeric films possess enhanced long-range and conformational order as well as low intramolecular failure density and polydispersity. In this chapter, we discuss experimental results concerning charge carrier transport and, in more general terms, the device characteristics of unipolar single-layer diodes, employing a phenylene vinylene-based polymer and its oligomeric pendent. The current limitations of the unipolar diodes are interpreted on basis of the disclosed disorder energies.

4.1 Introduction

In amorphous polymeric films, the charge carrier transport is governed by its hopping nature and the high degree of diagonal and off-diagonal disorder as discussed in *Chapter 3* [1-3]. The static disorder energy, determining the activation energy of the charge carrier transport, is mostly related to the disordered nature of the intermolecular organization, involving fluctuations in the inter-site distance and orientation. These fluctuations give rise to a statistical distribution of site energies. Concomitantly, an intramolecular contribution to the energy dispersion of sites may exist that is subject to e.g. the chemical perfection, length or the molecular conformation of individual molecules in the bulk. Due to the nature of the chemical synthesis, a polymeric material exhibits a considerable chemical failure density and polydispersity, resulting in a distributed conjugation length. Moreover, due to conformational constrains in the bulk, which are predominant for materials based on long polymeric molecules, the intramolecular ππ-stacking is disturbed. As a consequence, energy levels are intrinsically a matter of distribution. For short oligomeric molecules on the other hand, the intramolecular contribution to the disorder energy is strongly reduced, since they can be produced with high chemical perfection and because the conformational constrains in the bulk are small. In single crystals of conjugated oligomers that possess pronounced long-range intermolecular order [4-6], the intermolecular disorder energy might, moreover, be negligibly small if compared to the polaron binding energy. In such a system, disorder will hardly play a role in the charge carrier transport. In polycrystalline oligomeric films as usually used in the field of light-emitting diodes (LEDs) and photovoltaic cells, however, the situation is more complex. Even though these films are crystalline, dislocations, crystal failures and grain boundaries may govern the transport properties, resembling a transition from order- (single crystal) to disorder-dominated (polymeric film) solid-state properties [7].

The scope of the here-presented study was to investigate the differences in the charge transport properties of the polymer poly(2-methoxy-5-(2’-ethyl-hexyloxy)-phenylene vinylene) (MEH-PPV) forming amorphous films and its oligomeric counterpart (*E*,*E*,*E*,*E*)-1,4-bis[(4-styryl)styryl]-2-methoxy-5-(2’-ethyl-hexyloxy) benzene (MEH-OPV5) (Fig. 4.1), which grows to polycrystalline films. Furthermore,

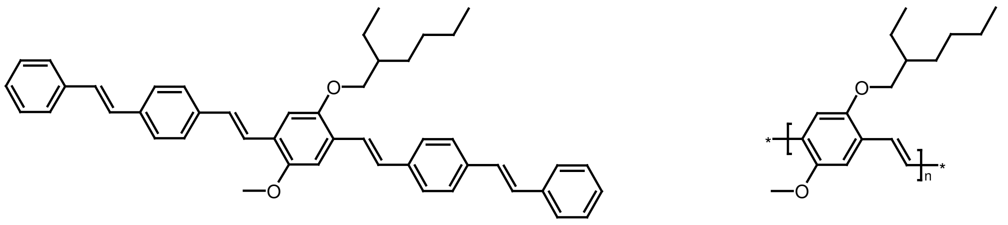

MEH-OPV5 MEH-PPV

Figure 4.1 The chemical structure of MEH-OPV5 and MEH-PPV we investigated the device characteristics of simple unipolar single-layer diodes based on these materials in more general terms. Employing chemically alike oligomeric and polymeric materials emphasizes their differences in purity, polydispersity, molecular conformation and intermolecular organization, which finally affect the device performance. Substantial differences between the hole transport properties and the device performance of unipolar diodes based on MEH-OPV5 and MEH-PPV were found, which we related to the disparity in their disorder energies.

4.2 Charge carrier mobility

The determination of the charge carrier mobility in semiconducting media is usually done by time-of-flight (TOF) measurements, where free charge carriers are optically generated close to one of the electrodes and subsequently travel through the semiconductor layer [8-10]. By measuring the temporal course of the photocurrent, information about the charge carrier transport can be gained. However, since extinction coefficients are typically small for organic semiconductors, a layer thickness of several µm is required in order to prevent homogeneous excitation throughout the entire film. As an alternative to TOF measurements, the charge carrier mobility in strongly luminescent organic semiconductors can be determined on basis of transient electroluminescence (EL), where the sample thickness can be smaller than the penetration depth of light, and measurements can be performed in a typical LED configuration [11-14]. The equivalence of transit times obtained by transient EL and TOF measurements was confirmed experimentally [15].

In transient EL measurements, a planar LED is exposed to a short voltage pulse in forward bias direction, and the light emitted upon this stimulus is collected by a photodiode or, in our case, by a photomultiplier. Typically, the appearance of the EL signal is delayed with respect to the stimulus, since the charge carriers that are injected at both contacts have to travel through the film until they meet and radiative recombination can occur. In general, the delay time τ_t required for the appearance of EL is, therefore, determined by both the hole and the electron transport, compromising transient EL measurements as a tool for the exact determination of individual transit times:

Eq. 4.1

$$\tau_t = \frac{\tau_e \tau_h}{\tau_e + \tau_h} \underset{\tau_e >> \tau_h}{\approx} \tau_h$$

Here, τ_e and τ_h are the electron and hole transit times, respectively. Yet, in materials with highly unbalanced electron and hole transport properties, the movement of the slower carrier species, which in PPV-based materials, such as MEH-PPV or MEH-OPV5, are typically the electrons, can be neglected and the transit time of the faster charge carrier type solely determines the delay time. The delay time between the rising edge of the voltage pulse and the appearance of the EL signal is then a direct measure for the hole transit time.

Organic LEDs based on MEH-OPV5 and MEH-PPV were investigated with respect to their transient EL behavior. While an indium tin oxide(ITO)-coated glass substrate covered with a thin layer of poly(3,4-ethylene dioxythiophene) (PEDOT) doped with poly(styrene sulfonic acid) (PSS) served as the anode, Ca was used as the cathode in order to increase and equilibrate the electron and hole densities in the semiconductor. The ITO-coated glass substrates were pre-cleaned by a wet cleaning procedure and PEDOT:PSS (Bytron P TP AI 4083) was spin-coated from a water dispersion and dried under high vacuum. The substrates were then inserted in the glove-box system filled with dry nitrogen. Subsequently, MEH-OPV5 was vacuum-deposited at 10^{-7}mbar with a deposition rate of 1 Å/s. Thin films of MEH-PPV (ADS100RE, M_W = 50000, American Dye Source Inc.) were spin-coated from a 0.6 wt % 1,2-dichlorobenzene solution and were dried under high vacuum. The top metal electrode was deposited by thermal vacuum deposition at 10^{-6}mbar.

We first discuss the temporal course of EL transients obtained from vacuum-deposited MEH-OPV5 thin-film diodes. In Fig. 4.2, a typical EL signal in pulsed regime is shown for a single-layer ITO/PEDOT:PSS/MEH-OPV/Ca diode. After an initial delay time, the EL signal increased double exponentially. A detailed analysis of such EL transients was elaborated by Pinner *et al.* [12]. In the frame of their model, the transit time for the faster holes is given by the initial delay time t_d, after which the first recombination occurs, and t_1, after which the charge distribution of the faster charge carrier species is fully established. An increase in EL after t_d+t_1 is then due to the built-

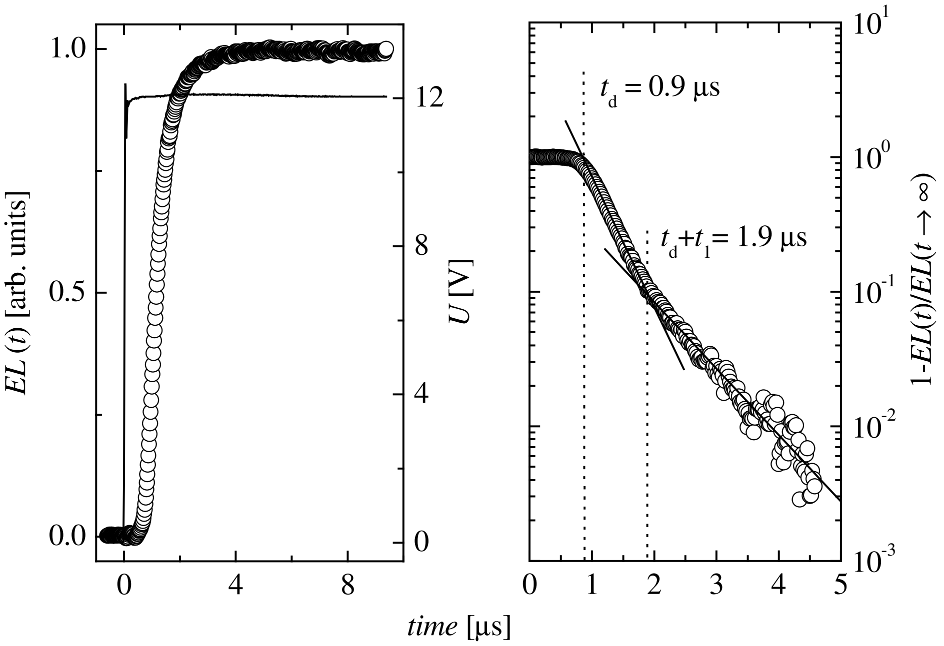

Figure 4.2 *Left*: The transient EL signal for an ITO/PEDOT:PSS/MEH-OPV (300 nm) /Ca device (O) and the applied voltage (–) in time. *Right*: Two distinct exponential increases of the EL signal were observed.

up of the charge carrier distribution of the slower electrons. However, from Fig. 4.2 it becomes apparent that the time constant of the second exponential increase is comparable to that of the first one, meaning that the electron distribution was established rather fast. This indicates that electron transport in MEH-OPV5 is only slightly slower than hole transport. For MEH-PPV, similar observations have been reported that are in agreement with our experimental observations [16, 17]. As a consequence, the hole transit times determined by means of transient EL are slightly underestimated, because the electron transit is not taken into account.

Out of the unveiled transit times, the hole mobility μ_h can be determined by $\mu_h = d/(\tau_h F)$, where d is the thickness of the semiconductor and F is the internal field. This holds even under space-charge conditions, since it has been shown that the electric field pulling the charge carrier front in the semiconductor is unaffected by any space-charge [18]. The resulting hole mobilities obtained from transient EL measurements as a function of the square root of the field can be seen in Fig. 4.3. Yet, the determination of the hole mobility from transient EL measurements is only valid when the charge transport is of non-dispersive nature. A clear signature of dispersive transport is a pronounced thickness dependence of the determined mobilities [11, 19]. Since we did not observe any variation in hole mobilities upon two fold increase in the semiconducting layer thickness, the hole transport can be regarded to be non-dispersive, with the transient hole mobility being the actual DC hole mobility.

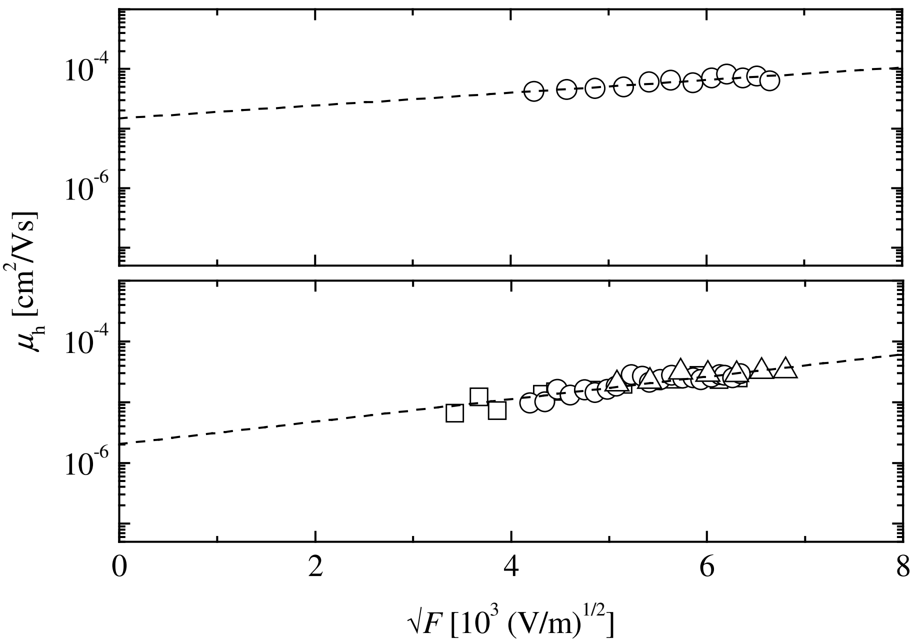

Figure 4.3 *Top*: The hole mobility of MEH-OPV5 versus the square root of the electric field determined by transient EL measurements. *Bottom*: The hole mobility of MEH-PPV versus the square root of the electric field obtained by transient EL measurements for different layer thickness: □ for 140 nm, ○ for 175nm, and Δ for 230 nm.

At a field strength of 3×10^{7} V/m, hole mobilities of 2.1×10^{-5} cm^{2}/Vs and 5.7×10^{-5} cm^{2}/Vs were measured in MEH-PPV and MEH-OPV5, respectively. For both materials, the hole mobilities were found to be field-activated according to Gill's equation, indicating that holes move by a disorder-controlled hopping mechanism:

Eq. 4.2
$$\mu_h = \mu_0(T)\exp\left[\gamma_\mu(T)\sqrt{F}\right]$$

Here, μ_0 is the zero field hole mobility, γ_μ is the field activation factor and T is the temperature. The field activation factor γ_μ and the zero field hole mobility μ_0 of MEH-OPV5 were 2.45×10^{-4} (m/V)$^{1/2}$ and 1.5×10^{-5} cm^{2}/Vs, respectively. The obtained hole mobility of MEH-OPV5 was similar to the value measured by Jain *et al.* [20]. The field dependence of the hole mobility of MEH-PPV was found to be stronger than the one of MEH-OPV5. Values of 2×10^{-6} cm^{2}/Vs and 4.3×10^{-4} (m/V)$^{1/2}$ were found for μ_0 and γ_μ, respectively. While the zero field hole mobility of MEH-PPV was one order of magnitude higher than that given in literature, the field activation factor was comparable to the one determined by Shen *et al.* [21].

Although the hole mobilities of MEH-OPV5 and MEH-PPV showed similar dependence on the electric field according to Gill's equation, they exhibited obvious differences. Whereas the field activation of MEH-PPV was much stronger than the one of its oligomeric counterpart, the zero field mobility was smaller, resulting in a lower hole mobility in MEH-PPV than in MEH-OPV5 in the measurement range. As will be shown in section 4.4, this observation has a strong impact on the general device performance of diodes based on either MEH-PPV or its oligomeric counterpart.

4.3 Diode characteristics

As reasoned in *Chapter 3*, unipolar diodes can either be injection-limited when the interfacial barrier height is sufficiently large to prevent strong charging of the semiconductor under bias, or space-charge-limited when the charge carrier density required for substantial space-charge built-up in the bulk is supplied by the contacts [22-25]. The unipolar trap-free space-charge-limited current (TFSCLC) is given by the Mott and Gurney law [22]:

Eq. 4.3
$$j_{\mathrm{TFSCLC}} = \frac{9}{8}\varepsilon_{\mathrm{s}}\mu\frac{U^2}{d^3}$$

where ε_s is the permittivity, μ is the charge carrier mobility, U is the applied bias, and d is the semiconductor layer thickness. It is important to realize that generally, the space-charge-limited current (SCLC) is proportional to μ. The investigation of space-charge-limited diodes therefore supplies information on the charge carrier mobility of the employed semiconductor [2, 16]. Vice versa, however, TFSCLCs can be simulated on basis of independently determined carrier mobilities and be compared to the measured IV–characteristics. In this way, information on the current limitation in the respective device can be obtained [21, 26].

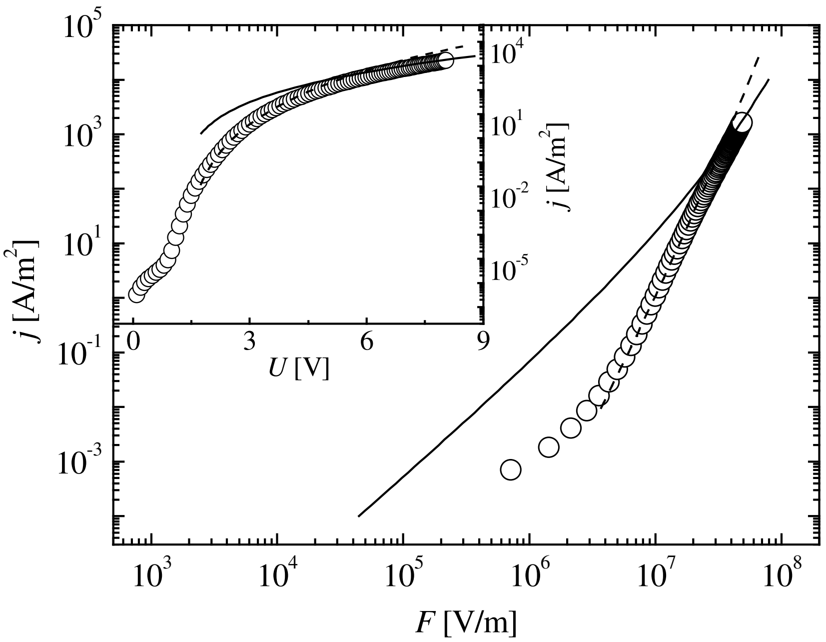

Figure 4.4 IV–characteristic of an ITO/PEDOT:PSS/MEH-PPV/Al diode under forward bias (○) for a 140 nm layer of MEH-PPV. The continuous line is a numerical solution for TFSCLC, considering the field-activated hole mobility determined by transient EL measurements. The dashed line is a fit in the low-field regime, assuming trap-controlled SCLC according to Eq. 4.4: $N_v \equiv 10^{20}$ cm^{-3}, $N_t = 7.5\ 10^{17}$ cm^{-3}, and m =3.2.

4.3.1 MEH-PPV

The IV–characteristic of an unipolar single-layer ITO/PEDOT:PSS/MEH-PPV/Al device can be seen in Fig. 4.4. In addition, the numerically simulated TFSCLC, considering the field-dependent hole mobility obtained by transient EL measurements, is depicted. The measured current densities exhibited a strong increase with the electric field and tended to saturate to the simulated TFSCLC at higher fields, which suggests that the current is space-charge-limited at high electric fields. This is in line with observations of others, where TFSCLC was achieved with high-workfunction synthetic metals used as cathode [16]. The initial current densities at low fields were, however, far below the simulated TFSCLC. In this region, the current density increase with the electric field was stronger than the one predicted by the simulated TFSCLC. Such an IV–characteristic at low electric fields is explainable by a trap-controlled SCLC. The trap-controlled space-charge-limited current density with an exponential or Gaussian trap distribution follows:

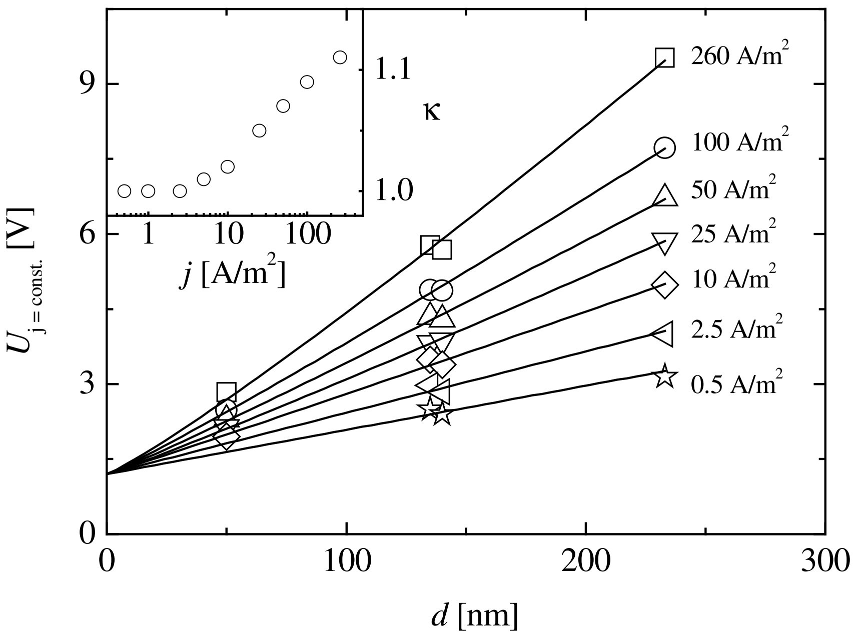

Figure 4.5 Required drive voltage at constant current densities versus the layer thickness of MEH-PPV measured in an ITO/PEDOT:PSS/MEH-PPV/Al diode structure. Lines represent the least mean square fits with a power law $U\text{-}U_{\text{bi}} \propto d^{\,\kappa}$, U_{bi} being the built-in potential. The insert shows the resulting power κ versus the current density.

Eq. 4.4
$$j_{\text{SCLC}} = q^{1-m}\mu_{\text{h}} N_{\text{V}} \left(\tfrac{2m+1}{m+1}\right)^{m+1} \left(\frac{m}{m+1}\frac{\varepsilon_{\text{s}}}{N_{\text{t}}}\right)^{m} \frac{U^{m+1}}{d^{2m+1}} \qquad m>1$$

where m is a parameter related to the trap distribution width, q is the electron charge, N_{V} is the density of states of the valence band and N_{t} is the trap density [24, 27, 28]. Obviously, the current density increase is steeper than the one for a TFSCLC. From Fig. 4.4, we see that perfect fits can be obtained based on Eq. 4.4, requiring reasonable parameters [29]. However, besides a trap-controlled SCLC, charge carrier injection from the metal to the organic material can predict a similar behavior. Obviously, additional independent verification of space-charge effects was required.

One indisputable indication for SCLC is a proper thickness dependence. In Fig. 4.5, we show the required drive voltage at constant current density in dependence of the thickness of the active layer. In the case of a field-dependent mobility, the thickness dependence of the required drive voltage at constant current density is generally described by $d^{\,\kappa}$ (see e.g. Eq. 4.3), where $1<\kappa<1.5$ holds for TFSCLC. For a trap-controlled SCLC of exponential or Gaussian trap distribution, $1<\kappa<2$ holds, depending on the parameter m and the field-dependent mobility. In the regime of injection limitation, on the other hand, no space-charge effects occur and the electric field is constant in the entire semiconductor. $\kappa = 1$ is obtained. By fitting the data for each current density with a power law, we obtained κ as a function of the current density shown in the insert of Fig. 4.5. Obviously, κ is close to 1 in the low-current regime. However, assuming a trap-controlled SCLC of exponential or Gaussian trap distribution at low current densities in combination with the field-dependent mobility obtained by transient EL measurements, κ exceeds 1.63. This indicates that current densities of unipolar single-layer ITO/PEDOT:PSS/MEH-PPV/Al diodes are injection-limited for low fields, rather than being space-charge-limited. At higher current densities, κ increases to approximately 1.12 (insert Fig. 4.5), which suggests that space-charge effects are indeed present. This is in line with the conformity of simulated TFSCLC and measured current at higher electric fields. Certainly, the influence of the field-dependent charge carrier mobility is enhanced at higher fields, resulting in a κ lower than 1.5. However, assuming TFSCLC and using the field-dependent hole mobility of MEH-PPV obtained by transient EL measurements, a κ ≥ 1.3 is predicted, while a value of 1.12 was measured. We can therefore conclude that although space-charge effects were present at higher fields, TFSCLC was not yet fully established, and the system was still in a transition regime between injection and space-charge limitation.

4.3.2 MEH-OPV5

Recently, it has been reported that the current densities through ITO/MEH-OPV5/Al diodes are space-charge-limited and IV–characteristics were modeled over a wide voltage and current range [20]. In Fig. 4.6, we present the IV–characteristic of a single-layer ITO/PEDOT:PSS/MEH-OPV5/Al device and the simulated TFSCLC. Interestingly, the IV–characteristic indeed resembles SCLC in shape over a wide range of voltage and current density, although it differs in amplitude. This discrepancy in current density amplitude is slightly relaxed by the fact that the mobility determined by transient measurements is overestimated due to the ignorance of the electron transit. The observation that the measured current is similar in shape but lower than the simulated TFSCLC can be modeled by a shallow or single trap level-controlled SCLC that is proportional to an effective charge carrier mobility $\theta_t\mu$ [24, 28]:

Eq. 4.5

$$j_{\mathrm{SCLC}} = \frac{9}{8}\varepsilon\theta_{\mathrm{t}}\mu\frac{U^2}{d^3}$$

The effective charge carrier mobility is a product of the charge carrier mobility μ and the ratio of free and total charge carrier densities θ_t, resulting in a lower amplitude of SCLC compared to the trap-free case. Yet, injection limitation cannot be excluded as well. Apparently, a proper thickness dependence is required to proof the presence of SCLC.

The predicted κ for a single trap level-controlled SCLC ranges from 1.47 to 1.43 for the lowest and highest measured current density, respectively. These values are close to 1.5, because the field dependence of the hole mobility is weak. In the insert of Fig. 4.7, the required drive voltage at constant current densities in dependence of the active layer thickness is shown. Despite some irreproducible variations in the measured current densities from sample to sample, the thickness dependence could not be

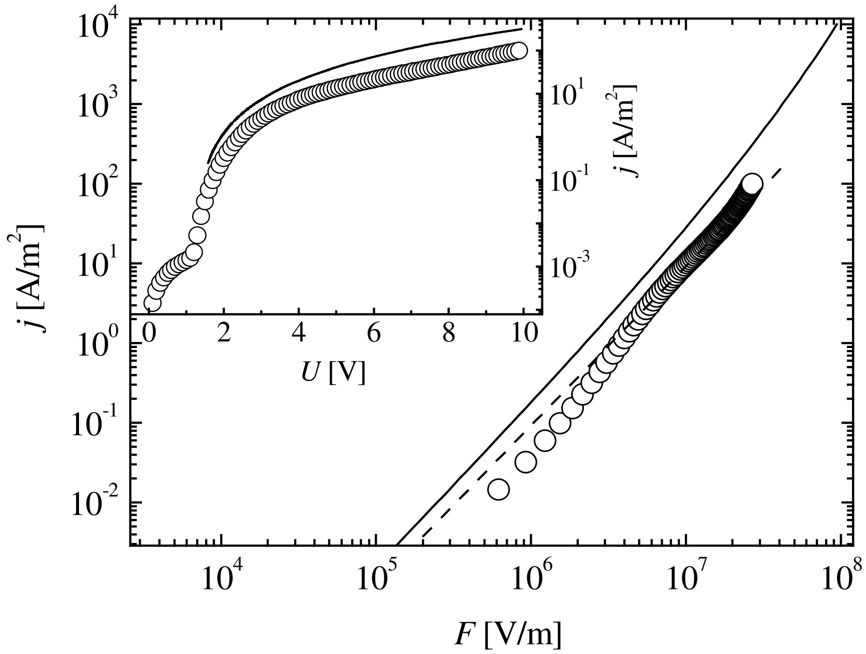

Figure 4.6 IV–characteristic of an ITO/PEDOT:PSS/MEH-OPV5/Al diode under forward bias (○) for a 325 nm thick layer of MEH-OPV5. The dashed line is a fit according to TFSCLC with a constant mobility. The continuous line is a numerical solution for TFSCLC, considering a field-dependent mobility according to Eq. 4.2. The field activation factor and the zero field hole mobility of MEH-OPV5 were taken from transient EL measurements.

approximated with $\kappa \geq 1.43$ but rather with $\kappa \approx 1$, questioning the presence of SCLC and suggesting injection limitation.

The comparison of the IV–characteristics of ITO/PEDOT:PSS/MEH-OPV5/Al and ITO/MEH-OPV5/Al diodes depicted in Fig. 4.7 is also in favor of injection limitation. The shapes of both IV–curves are similar, but the amplitude is much smaller in the case of ITO/MEH-OPV5/Al, requiring a barrier height increase of approximately 0.15 eV if compared to the barrier at an PEDOT:PSS/MEH-OPV5 contact. Such a barrier height change reflects the difference in anode workfunction of PEDOT:PSS and ITO. At higher bias, both curves show an exponential behavior versus the square root of the field, which is typical for injection-limited current. This observation confirms that ITO/MEH-OPV5/Al devices are injection-limited, an assumption we used in *Chapter 3*, and suggests injection as the current-limiting process in ITO/PEDOT:PSS/MEH-OPV5/Al devices.

To demonstrate that even an ITO/PEDOT:PPS/MEH-OPV5/Al diode exhibits injection limitation at forward bias, we simulated the IV–characteristic by the injection model introduced in *Chapter 3* and compared the simulations with the IV–characteristics of an ITO/PEDOT:PSS/MEH-OPV5/Al diode for different temperatures. From Fig. 4.8 it is apparent that not only the shape, but also the absolute values of currents could be simulated correctly for a wide temperature, voltage and

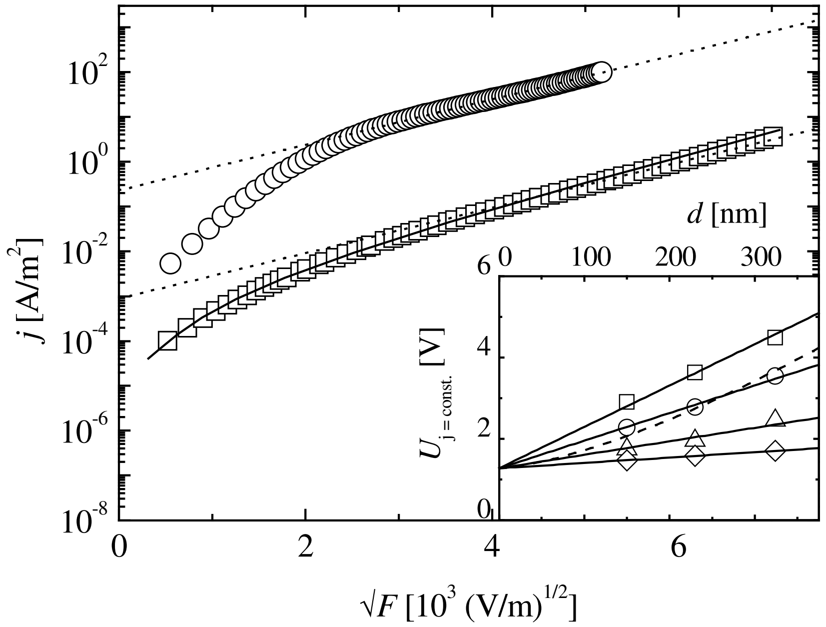

Figure 4.7 IV–characteristics of an ITO/MEH-OPV5 (370nm)/Al (□) and an ITO/PEDOT:PSS (325nm)/MEH-OPV5/Al (○) diode. The continuous line is a fit according to the charge injection model proposed in *Chapter 3*. *Insert*: Required drive voltage for constant current densities versus the semiconductor layer thickness: 10 A/m^2 (□), 5 A/m^2 (○), 1 A/m^2 (Δ),and 0.1 A/m^2 (◊). The continuous lines are linear fits, and the dotted line indicates a $d^{1.44}$ law.

current range, with a reasonable dielectric constant of 3.2, barrier height of 0.47 eV, and interfacial Gaussian density of states (DOS) width of 0.06 eV. Optimal fits were achieved with a field activation factor of the charge carrier mobility of 1.7×10^{-4} (m/V)$^{1/2}$ and a zero field hole mobility of 2.2×10^{-5} cm^2/Vs, being close to the parameters obtained by transient EL measurements.

Hence, we can conclude that due to the observed thickness dependence and the influence of the anode workfunction on the absolute value of the current (but not on the shape), injection limitation is most likely the current-limiting process, even though the IV–characteristics show typical features of SCLC. This conclusion is supported by the fact that the observed IV–characteristics could be simulated over a wide current and temperature range with the charge carrier injection model proposed in *Chapter 3*.

4.4 Effects of diagonal disorder

We have shown that the zero field hole mobility of the polymer MEH-PPV is lower than the one of its oligomeric counterpart MEH-OPV5, while the field activation is stronger. The field dependence of the hole mobilities followed Gill's equation, indicating that the field activation is disorder-controlled [30]. The field and temperature dependence of the charge carrier mobility for disorder-controlled transport

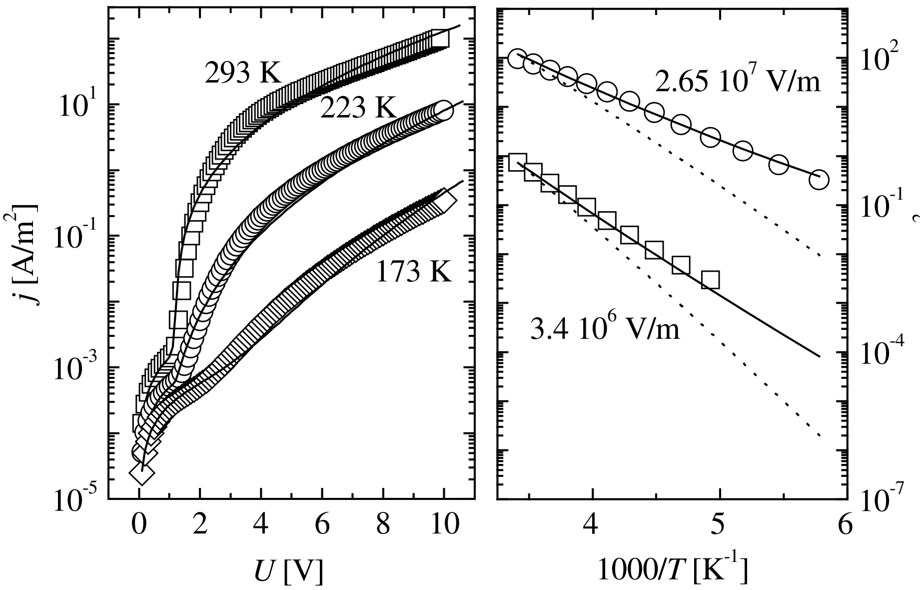

Figure 4.8 *Left*: IV-characteristics of an ITO/PEDOT:PSS/MEH-OPV5/Al device for different temperatures. The MEH-OPV5 layer thickness was 325 nm. Lines are fits according to the charge injection model proposed in *Chapter 3*. A σ of 0.06 eV and a barrier height ϕ of 0.47 eV (ϕ' = 0.39 eV at 293 K) were determined. *Right*: Arrhenius plots of the current densities at different fields. The continuous lines are fits, using the charge injection model proposed in *Chapter 3*. The dotted lines are the expectations, excluding the effective lowering of the barrier height due to diagonal disorder.

is well described in the frame of the correlated Gaussian disorder model (CDM) introduced in *Chapter 3* [31]. In the CDM, the field activation is governed by the nearest neighbor hopping distance *a* and the Gaussian DOS width σ. Assuming a typical hopping distance of 1 nm, we obtain from the field activation a σ of 0.07 ±0.01 eV for MEH-OPV5. Interestingly, the interfacial σ used in the injection model is very close to the one determining the field dependence of the charge carrier mobility, which indicates that the diagonal disorder of MEH-OPV5 at the organic (PEDOT:PSS)/organic (MEH-OPV5) interface is comparable to the diagonal disorder in the MEH-OPV5 bulk. Yet, σ of MEH-OPV5 is much smaller than σ of its corresponding polymer that was found to be around 0.095 ±0.01 eV from the field activation of the hole mobility. The larger σ of MEH-PPV, concomitantly, results in an approximately 10 times lower zero field hole mobility, which was indeed confirmed by transient EL measurements and which justifies the applicability of the CDM model.

The noticeable disparity in σ is, in general, related to the inter- and intramolecular differences between the two compounds in the solid state. While MEH-PPV exhibits an amorphous film morphology, MEH-OPV5 tends to form polycrystalline films when deposited by thermal vacuum deposition [32]. Yet, the domain size of MEH-OPV5 crystals is known to be in the nm-range, with the degree of crystallization depending on the preparation conditions. When the substrate temperature is increased during thermal vacuum deposition, the MEH-OPV5 crystal

$$\delta\phi' \approx \frac{q}{2kT}\left(\sigma^2_{MEH-OPV5} - \sigma^2_{MEH-PPV}\right)$$

$$\phi' \approx \phi - \frac{q\sigma^2}{2kT}$$

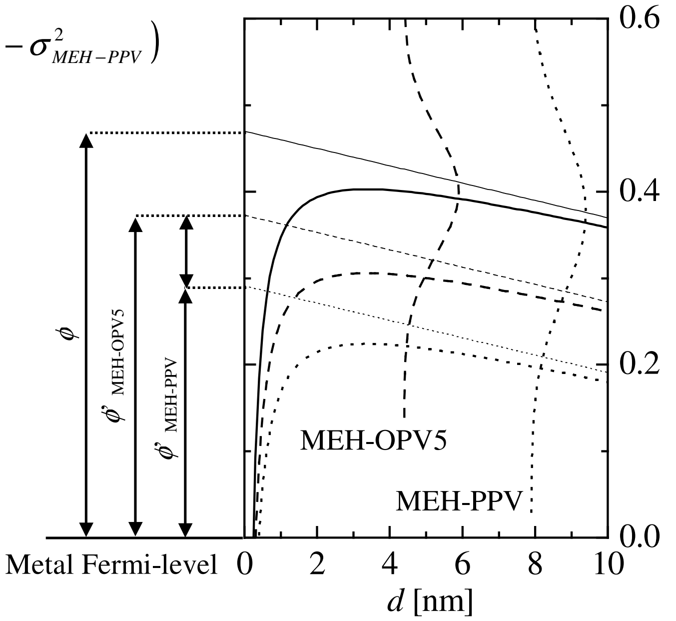

Figure 4.9 Scheme of the barrier lowering due to diagonal disorder for MEH-OPV5 and MEH-PPV. The continuous lines are the potential well (thick line) and the electrostatic potential (thin line) excluding diagonal disorder. The dashed and the dotted lines are the potential curves of MEH-OPV5 and MEH-PPV, respectively, taking the diagonal disorder-induced potential lowering into account, which results in an effective barrier height ϕ'. The density of states is taken as a Gaussian distribution function of width σ. The difference of ϕ' for MEH-OPV5 compared to MEH-PPV is then given by $\delta\phi'$.

size increases and the structural difference towards its polymeric counterpart is emphasized. In other words, the intermolecular contribution to the disorder energy is reduced. Joswick *et al.* [32] found that the crystal size of MEH-OPV5 in polycrystalline films exceeds 20 nm when deposited at 80°C substrate temperature, while it is far below 5 nm for room temperature deposition. Although the oligomeric film deposited at room temperature is still polycrystalline, it though exhibits an intermolecular organization that is close to an amorphous one, emphasizing the intramolecular contributions to the differences in disorder energies between polymer and oligomer.

The fact that the disorder energies vary between MEH-OPV5 and MEH-PPV has not only a strong impact on the charge carrier mobility itself, but also affects the diode dark-current characteristics in general. As described above, the IV–characteristics of ITO/PEDOT:PSS/MEH-PPV/Al and ITO/PEDOT:PSS/MEH-OPV/Al are rather different. While the former exhibits SCLC at higher fields, the latter is still injection-limited. Due to the poorer hole mobility in MEH-PPV, induced by its strong diagonal disorder, the drift velocity of the injected charge carriers in the bulk is lower. Consequently, substantial space-charge built-up and, hence, SCLC become more probable than for MEH-OPV5. On the other hand, it has been demonstrated that the charge carrier injection current is proportional to the hole mobility in the bulk [21], which leads to a lower charge carrier injection rate in the polymer, in turn decreasing the probability to reach SCLC. An alternative explanation for the disclosed disparities in current limitation involves differences in the injection barrier height induced by their dissimilar diagonal disorder. As discussed in *Chapter 3*, the interplay between the Boltzmann exponent and the Gaussian DOS of width σ results in an effective temperature-dependent lowering of the transport level [33-36]. As a consequence, the asymptotic charge injection barrier height ϕ is reduced to an effective asymptotic charge injection barrier height ϕ', as illustrated in Fig. 4.9. The lower σ in MEH-OPV5 (approximately 0.07 eV) compared to MEH-PPV (approximately 0.1 eV) thus results in a disorder-induced difference $\delta\phi'$ of the effective hole injection barriers of already 0.1 eV at room temperature. In addition, the band gap of MEH-PPV is more narrow than the band gap of MEH-OPV5. While the latter was determined by absorption measurements to be approximately 2.5 eV, it was 2.2 eV for MEH-PPV. The difference of 0.3 eV can potentially result in a further reduction of the barrier height at the MEH-PPV/PEDOT:PSS contact if compared to the MEH-OPV5/PEDOT:PSS contact. However, the ionization potential of MEH-OPV5 was reported to be 5.3 ±0.2 eV, i.e. close to the one of MEH-PPV, which suggests a potential barrier height difference due to the disparity in band gaps below 0.3 eV [37-39]. After all, $\delta\phi'$ between an oligomeric and a polymeric contact with PEDOT:PSS can come close to 0.4 eV, but will be at least 0.1 eV at room temperature. The simulation of the injection current with the charge injection model proposed in *Chapter 3* (Fig. 4.8) unveiled a ϕ' of approx. 0.4 eV for a PEDOT:PSS/MEH-OPV5 contact. Assuming a minimal $\delta\phi'$ of 0.1 eV, the maximal obtainable ϕ' at a PEDOT:PSS/MEH-PPV contact is 0.3 eV. However, since the band gap in MEH-PPV is smaller than in MEH-OPV5, an even further reduced hole injection barrier is feasible. Hole injection is, therefore, more efficient for an ITO/PEDOT:PSS/MEH-PPV/Al device, and SCLC becomes more probable, which is in agreement with our experimental observation. The unveiled difference in diagonal disorder consequently explains the observed disparity in the current limitation of unipolar single-layer diodes based on MEH-PPV and MEH-OPV5.

4.5 Conclusion

In this chapter, we demonstrated the influence of disorder on the device performance of unipolar single-layer organic diodes. In first instance, hole mobilities were measured in the polymer MEH-PPV and in its corresponding oligomer MEH-OPV5. The analysis of the field-dependent hole mobilities suggested that the hole transport in both materials is governed by an disorder-dominated hopping process. The disorder energy difference between oligomer and polymer was found to be substantial, and made SCLC in the highly disordered polymer more probable than in the corresponding oligomer, since the disorder-induced lowering of the hole injection barrier favors efficient charge carrier injection from the metal into the polymer. In MEH-OPV5, in contrast, the injection barrier lowering is minor and eventuates in a sufficiently high hole injection barrier, preventing substantial space-charge built-up and, hence, SCLC.

References

[1] H. Bässler, Phys. Stat. Sol. B **175**, 15 (1993).

[2] P. W. M. Blom, M. J. M. de Jong and J. J. M. Vleggaar, Appl. Phys. Lett. **68**, 3308 (1996).

[3] S. Forero, P. H. Nguyen, W. Brütting and M. Schwoerer, Phys. Chem. Chem. Phys. **1**, 1769 (1999).

[4] W. Warta and N. Karl, Phys. Rev. B **32**, 1172 (1985).

[5] T. Siegrist, R. M. Fleming, R. C. Haddon, R. A. Laudise, A. J. Lovinger, H. E. Katz, P. Bridenbaugh and D. D. Davis, J. Mater. Res. **10**, 2170 (1995).

[6] R. C. Haddon, T. Siegrist, R. M. Fleming, P. M. Bridenbaugh and R. A. Laudise, J. Mater. Chem. **5**, 1719 (1995).

[7] S. Verlaak, V. Arkhipov and P. Heremans, Appl. Phys. Lett. **82**, 745 (2003).

[8] R. G. Kepler, Phys. Rev. **119**, 1226 (1962).

[9] E. Lebedev, T. Dittrich, V. Petrova-Koch, S. Karg and W. Brütting, Appl. Phys. Lett. **71**, 2686 (1997).

[10] D. Poplavskyy and J. Nelson, J. Appl. Phys. **93**, 341 (2003).

[11] P. W. M. Blom and M. C. J. M. Vissenberg, Phys. Rev. Lett. **80**, 3819 (1998).

[12] D. J. Pinner, R. H. Friend and N. Tessler, J. Appl. Phys. **86**, 5116 (1999).

[13] T. C. Wong, J. Kovac, C. S. Lee, L. S. Hung and S. T. Lee, Chem. Phys. Lett. **334**, 61 (2001).

[14] J. Wang, R. G. Sun, G. Yu and A. J. Heeger, J. Appl. Phys. **91**, 2417 (2002).

[15] P. Ranke, I. Bleyl, J. Simmerer, D. Haarer, A. Bacher and H. W. Schmidt, Appl. Phys. Lett. **71**, 1332 (1997).

[16] L. Bozano, S. A. Carter, J. C. Scott, G. G. Malliaras and P. J. Brock, Appl. Phys. Lett. **74**, 1132 (1999).

[17] J. C. Scott, P. J. Brock, J. R. Salem, S. Ramos, G. G. Malliaras, S. A. Carter and L. Bozano, Synth. Met. **111-112**, 289 (2000).

[18] M. Abkowitz and M. Morgan, Solid State Commun. **47**, 141 (1983).

[19] H. Scher and E. W. Montroll, Phys. Rev. B **12**, 2455 (1975).

[20] S. C. Jain, A. K. Kapoor, W. Geens, J. Poortsmans and R. Mertens, J. Appl. Phys. **92**, 3752 (2002).

[21] Y. Shen, M. W. Klein, D. B. Jacobs, J. C. Scott and G. G. Malliaras, Phys. Rev. Lett. **86**, 3867 (2001).

[22] N. F. Mott and R. W. Gurney, *Electronic Processes in Ionic Crystals*, Univ. Press, Oxford (1940).

[23] S. M. Sze, *Physics of Semiconductor Devices*, Wiley & Sons Inc., New York (1981).

[24] K. C. Kao and W. Hwang, *Electrical transport in solids with particular reference to organic semiconductors*, Pergamon Press, Oxford (1981).

[25] M. Pope and C. E. Swenberg, *Electronic processes in organic crystals*, Clarendon Press, Oxford Univ. Press, New York (1982).

[26] P. W. M. Blom and M. C. J. M. Vissenberg, Mater. Sci. Eng. **27**, 53 (2000).

[27] P. Mark and W. Helfrich, J. Appl. Phys. **33**, 205 (1962).

[28] J. S. Bonham, Aust. J. Chem. **26**, 927 (1973).

[29] V. Kumar, S. C. Jain, A. K. Kapoor, W. Geens, T. Aernauts, J. Poortmans and R. Mertens, J. Appl. Phys. **92**, 7325 (2002).

[30] K. Seki and M. Tachiya, Phys. Rev. B **65**, 1 (2001).

[31] S. V. Novikov, D. H. Dunlap, V. M. Kenkre, P. E. Parris and A. V. Vannikov, Phys. Rev. Lett. **81**, 4472 (1998).

[32] M. D. Joswick and I. H. Campbell, J. Appl. Phys. **80**, 2883 (1996).

[33] V. I. Arkhipov, E. V. Emelianova, Y. H. Tak and H. Bässler, J. Appl. Phys. **84**, 848 (1998).

[34] V. I. Arkhipov, U. Wolf and H. Bässler, Phys. Rev. B **59**, 7514 (1999).

[35] S. Barth, U. Wolf, H. Bässler, P. Müller, H. Riel, H. Vestweber, P. F. Seidler and W. Rieß, Phys. Rev. B **60**, 8791 (1999).

[36] M. A. Baldo and S. R. Forrest, Phys. Rev. B. **64**, 085201 (2001).

[37] S. C. Veenstra, U. Stalmach, V. V. Krasnikov, G. Hadziioannou, H. T. Jonkman, A. Heeres and G. A. Sawatzky, Appl. Phys. Lett. **76**, 2253 (2000).

[38] *Thesis:* S. C. Veenstra, *Electronic Structure of Molecular Systems. From Gas Phase to Thin Films to Devices*, Polymer Chemistry Rijksuniversiteit Groningen, Groningen (2002).

[39] I. H. Campbell, T. W. Hagler, D. L. Smith and J. P. Ferraris, Phys. Rev. Lett. **76**, 1900 (1996).

5

Morphology and hole transport properties of polycrystalline oligomeric thin films

---

Abstract

Bulk properties of organic semiconductors, in particular the charge carrier transport properties, are very sensitive to the intermolecular organization of the material. The relation between morphology and device performance, however, is not straightforward, especially in polycrystalline films of conjugated oligomers. Therefore, we investigated various thin-film morphologies of vacuum-deposited highly luminescent 2,5-di-*n*-octyloxy-1,4-bis[4’-(styryl)styryl]-benzene (Ooct-OPV5) in a typical light-emitting diode (LED) structure. Variations in the thin-film organization were obtained by changing the film deposition conditions, and are evaluated in this chapter. Furthermore, the hole mobility of each film was determined by transient electroluminescence (EL) measurements. The determined charge carrier transport properties are discussed, considering the respective thin-film morphologies, and morphology-dependent characteristics of the EL transient signal are outlined.

5.1 Introduction

The semiconducting nature of materials based on conjugated organic molecules finds its origin in the π-orbital overlap and the resulting delocalization of the π -electrons. While intrachain charge transport in such molecules is usually regarded to be fast due to the large ππ-overlap along the molecule, the charge transport through the bulk material is governed by the ππ-stacking of adjacent molecules. The semiconducting properties of the bulk material are, therefore, dependent on the mutual orientation and interchain distance of conjugated segments. Since in most of the conceivable and attractive applications based on organic semiconductors, such as field-effect transistors [1, 2], light-emitting diodes (LEDs) [3, 4], or photovoltaic cells [5, 6], the device structure is planar, molecular long-range ordering with continuous ππ-stacking along the preferential current direction is desirable. Information about the molecular arrangement in thin films, therefore, is useful to assess the suitability of a given organic conjugated material for semiconductor applications.

Due to an excellent control over the chemical structure and their low molecular weight, conjugated oligomers exhibit the useful property of strong crystallinity [7], which allows the preparation of high-purity polycrystalline thin films via thermal vacuum deposition techniques, and which might occasionally result in the desired long-range order in the solid state. By controlling the deposition conditions, such as evaporation rate and substrate temperature, particular thin-film morphologies with distinct crystallite perfection, size, and orientation can be established and these films need to be investigated with respect to their structural and charge carrier transport properties. Conjugated oligomers, for which single crystal structural information is available, have in this respect the advantage that the single crystal structure can be used for the interpretation of the diffraction data of their corresponding thin films, thereby

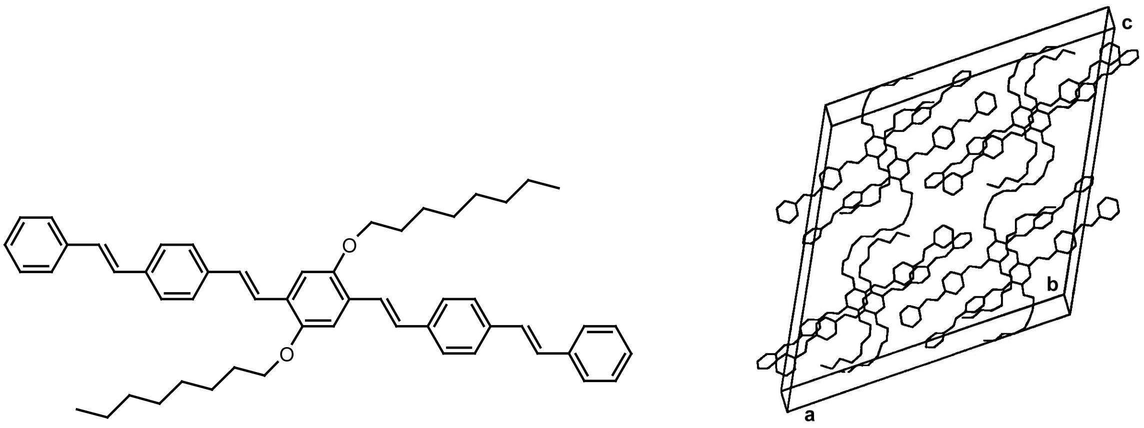

Figure 5.1 *Left*: Chemical structure of Ooct-OPV5. *Right*: Crystal structure of Ooct-OPV5; a = 36.2 Å, b = 7.5 Å, c = 36.6 Å, $\alpha = 90°$, $\beta = 116.9°$, and $\gamma = 90°$ [8].

reducing the complexity of the thin-film morphology determination. For highly luminescent 2,5-di-*n*-octyloxy-1,4-bis[4'-(styryl)styryl]-benzene (Ooct-OPV5) (Fig. 5.1), single crystals have been obtained [8] and were thoroughly characterized by X-ray and electron diffraction. The single crystal structure of this material displays a herring-like pattern as depicted in Fig. 5.1 (monoclinic, space group *I*2/*a*) [8, 9]. Additionally, thin-film morphologies of Ooct-OPV5 were previously investigated [8, 10, 11], their impact on the optical properties of the films was unveiled [8], and results on the device performance of field-effect transistors (FET) [2] and LEDs employing thin films of this material [8] were presented.

In contrast to this earlier work, we focused on the determination of the thin-film morphology in the actual LED configuration, providing meaningful information about the relation between morphology and device performance. Thin films of Ooct-OPV5 were deposited on a typical anode used in the field of photovoltaic cells and LEDs, namely an indium tin oxide (ITO)-coated glass substrate covered with a thin film of poly(3,4-ethylene dioxythiophene) (PEDOT) highly doped with poly(styrene sulfonic acid) (PSS). PEDOT:PSS is often used as a hole conductor between ITO and the active material [12, 13]. Pre-patterned ITO-coated glass substrates were wet cleaned, and thin layers (~80 nm) of PEDOT:PSS (Bytron P TP AI 4083) were deposited by spin-coating. The layers were dried under high vacuum at elevated temperature. Subsequently, the substrates were inserted into the glove-box system. Thin films of Ooct-OPV5 were thermal vacuum-deposited at a rate of 0.5 Å/s and at 10^{-7} mbar. We prepared Ooct-OPV5 thin films either on a heated substrate or under conditions, where thin films were thermally treated after deposition. For the former, the substrates were imbedded in a copper block with a deposition window, and the block was kept at T_{sub} during deposition by a computer-controlled feedback system. Subsequently, a counter electrode of calcium was deposited at 10^{-6} mbar on the obtained structure and the hole transport properties of the films were determined by transient electroluminescence (EL) measurements. Besides, the time evaluation of the EL signal was closely investigated. Finally, the morphologies of the resulting polycrystalline films in the LED structure were investigated by optical microscopy, X-ray diffraction (XRD), atomic force microscopy (AFM), and transmission electron microscopy (TEM).

We found that upon increase in substrate temperature T_{sub}, the crystal size and, most likely, the crystal quality in the film increased, which we regard as the major reason for the observed improved hole transport in films deposited at high T_{sub}. This is in line with a time-delayed peak-like increase of the EL signal that we relate to charge carrier trapping during operation, and redistribution and recombination of the accumulated charges after voltage switch-off. The effect diminishes for films prepared at higher T_{sub}, indicating a reduction of the trap density in the respective devices. We believe, moreover, that the relative appearance of two polymorphs, one being predominant for films deposited at low T_{sub} and another solely existing at T_{sub} above 60°C, may substantially influence the hole transport properties of Ooct-OPV5 thin films.

5.2 Thin-film morphology

The deposition of Ooct-OPV5 on an ITO/PEDOT:PSS substrate at room temperature resulted in a rough granular structure, indicating the presence of some extended crystallites. The observation of birefringence by cross-polarized microscopy supports this interpretation (Fig. 5.2). Tapping mode AFM revealed domains of wedge-like shape with a typical size of 0.05 × 0.4 μm^2 (Fig. 5.3). A thin-film RMS roughness of 8 nm was found. Interestingly, the domains of equal molecular orientation, which resulted in areas of equal light intensity in cross-polarized microscopy, were several microns larger than the domains observed by AFM. This clearly indicates correlation between the orientation of adjacent domains, which is additionally supported by the electron diffraction (ED) patterns, showing the presence of arcing (wide infra) (Fig. 5.4).

An increase in substrate temperature T_{sub} during Ooct-OPV5 deposition resulted in an increase of the mean size of crystalline domains. The transition in morphology was most pronounced in the range of 50°C to 60°C, which is in agreement with earlier findings [14]. The RMS roughness and the mean domain size obtained by AFM are listed in Table 5.1. The increase of the mean crystal size upon T_{sub} increase might have its origin in enhanced molecular diffusion, which leads to larger capture zones around nuclei and, hence, to bigger crystals. Once the crystals touch each other, coarsening might additionally occur, involving an effective mass transport from small crystals to large crystal. Coarsening is predominant at high T_{sub}, since the inter grain

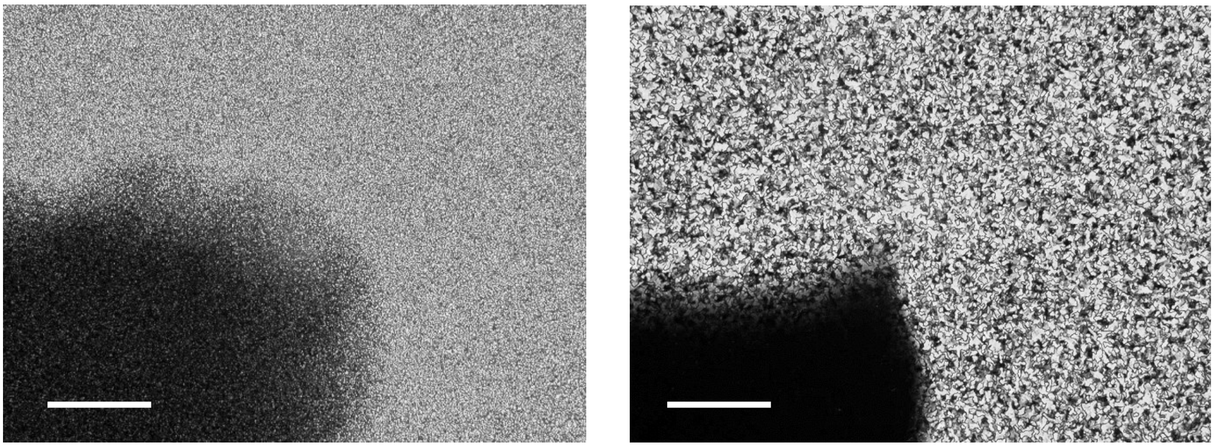

Figure 5.2 Polarized light optical micrographs of Ooct-OPV5 thin films evaporated at different T_{sub} on ITO/PEDOT:PSS substrates. *Left*: T_{sub} = 23°C (Scale bar: 50 µm). *Right*: T_{sub} = 89°C (Scale bar: 100 µm).

Table 5.1 RMS roughness and domain size of thin films of Ooct-OPV5 at different T_{sub} obtained by tapping mode AFM.

T_{sub} [°C]	23	50	57	89
Domain size [μm^2]	0.02	0.07	0.2	3
RMS roughness [nm]	8	13	23	60

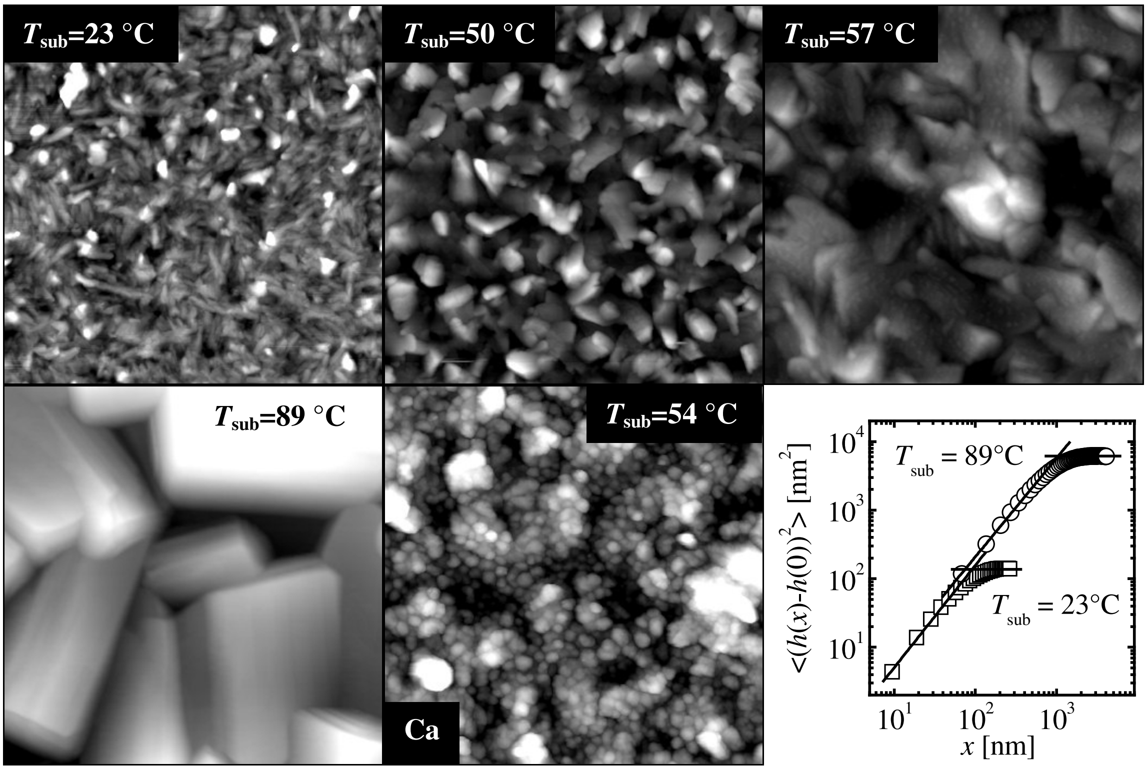

Figure 5.3 Topographical map (4×4 μm^2) of Ooct-OPV5 thin films deposited at different substrate temperatures T_{sub}, obtained by tapping mode AFM. The maximal height values of the topographical maps are 50 nm, 90 nm, 190 nm, 340 nm, and 190 nm for 23°C, 50°C, 57°C, and 89°C substrate temperature and the Ca overlayer, respectively. *Bottom, right*: Height correlation function $<(h(x)\text{-}h(0))^2>$ versus in-plane distance x for Ooct-OPV5 thin films deposited at different T_{sub}.

surface diffusion becomes more efficient. Yet, this process typically results in a depletion region around individual domains, which could not be confirmed by AFM (Fig. 5.3).

Profound information on the growth process can be gained by investigating the growth-front scaling characteristics of the films. If the roughness follows the self-affine scaling hypothesis [15], the height-to-height correlation function, averaged over the whole lateral extension, is given by $\left\langle (h(x)-h(0))^2 \right\rangle = Ax^{2H}$ for lateral distances x below the correlation length ξ, while $\left\langle (h(x)-h(0))^2 \right\rangle = 2\Sigma^2$ holds for x above ξ. Here, A = $(2\Sigma^2/\xi^{2H})$, Σ is the RMS roughness amplitude, and H is the roughness exponent. Recently, $\left\langle (h(x)-h(0))^2 \right\rangle$ obtained from Ooct-OPV5 thin-films that were thermal vacuum-deposited on SiO_2 substrates unveiled a pronounced change of H at T_{sub} around 50°C [14], which is indicative for a change in the growth mechanism. It was found that growth at T_{sub} around room temperature is dominated by desorption or vacancy formation [10, 11], while at elevated temperatures diffusive growth takes place [14]. However, from Fig. 5.3 it becomes apparent that no considerable change of H upon T_{sub} increase is present with Ooct-OPV5 deposited on PEDOT:PSS. This mismatch in the evaluation of H upon T_{sub} increase might be related to the different substrate and the higher deposition rate used in our experiment. The unveiled H of 0.7 suggests that growth of Ooct-OPV5 on PEDOT:PSS is dominated by surface diffusion relaxation ($0.66 \leq H \leq 1$) [16, 17]. Yet, diffusion-limited growth typically results in a fractal-like shape of crystallites, such as e.g. observed for thin films of Ooct-OPV5 deposited on silicon at high T_{sub} [14]. Here, however, domains were rather platelet-shaped and no coarsening was observed, although coarsening is expected to be favored during diffusive growth. The exact growth mechanism is, hence, not univocal. Nonetheless, the overall mechanism seems to be of Volmer-Weber type [18], since films coalesce in a pronounced 3-D manner rather than wetting the substrate. This implies that the attraction force between Ooct-OPV5 molecules of the film is stronger than between the molecules and the substrate.

5.2.1 Structure of polycrystalline thin films and polymorphism

The in-plane order of the thin oligomeric films was studied by TEM. A typical evolution of the ED pattern as a function of T_{sub} is depicted in Fig. 5.4. In accordance with the AFM results, the ED pattern of the room temperature films revealed non-uniform azimuthal intensities, which indicate that the in-plane orientations of adjacent Ooct-OPV5 domains are correlated. Upon T_{sub} increase, the ED reflections became sharper and narrower being consistent with the increase in domain size observed by AFM. The high-temperature ED pattern is discussed in the next section.

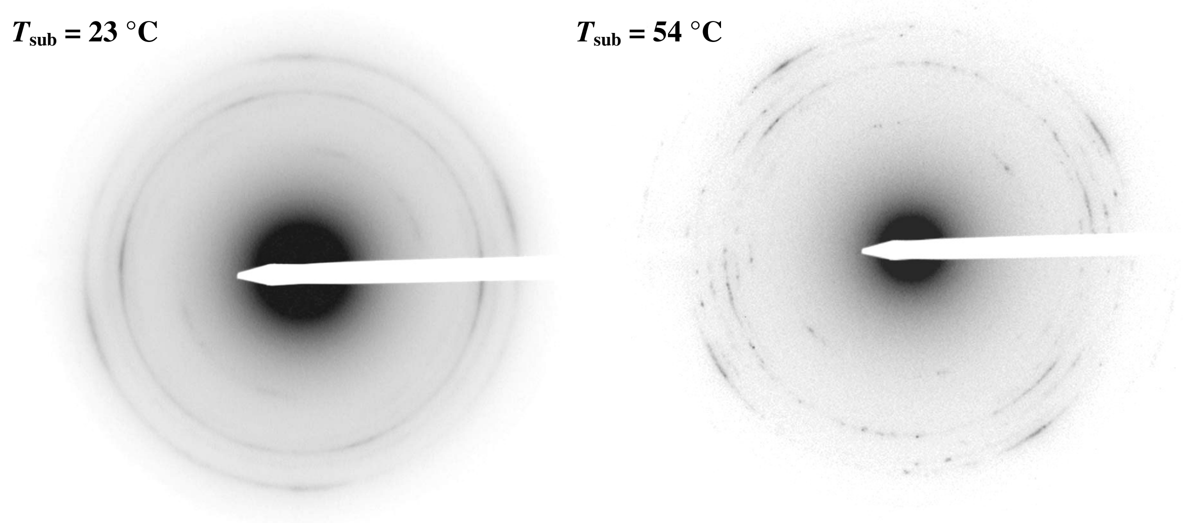

T_{sub} = 23 °C **T_{sub} = 54 °C**

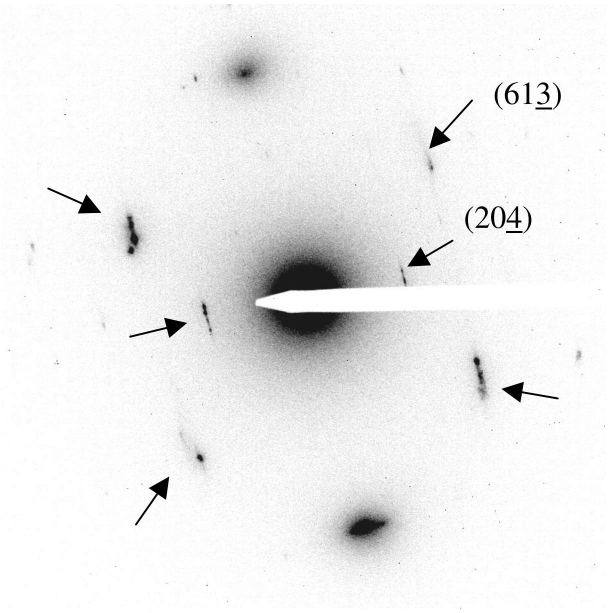

T_{sub} = 83 °C

Figure 5.4 Electron diffraction (ED) pattern of Ooct-OPV5 thin films deposited at different T_{sub} on ITO/PEDOT:PSS substrates. The arrows mark the (61$\underline{3}$) and the (20$\underline{4}$) reflections.

XRD (θ, 2θ) was used to investigate the thin-film order in the direction perpendicular to the substrate plane. The development of the XRD pattern upon T_{sub} increase is depicted in Fig. 5.5, and the reticular distances d_{hkl} of the main diffraction peaks are summarized in Table 5.2. For $T_{\text{sub}} \leq 54$°C, the XRD diffractogram consists mainly of two peaks corresponding to d_{hkl} values of 15.50 Å and 15.15 Å and of the second orders of these two reflections at 7.64 Å and 7.44 Å. An increase of T_{sub} above 54°C resulted in the appearance of two additional peaks at 16.9 Å and 16.4 Å that further gained intensity upon T_{sub} increase and afterwards co-existed with the two former peaks. Considering the known single crystal structure of Ooct-OPV5 [8], the 16.9 Å and 16.4 Å reflections can be attributed to the (002) and (200) planes of a single crystal, respectively (single crystal d_{hkl}: 16.34 Å, 16.15 Å). The presence of two first order reflections indicates the existence of two contact planes of the Ooct-OPV5 crystals with the ITO/PEDOT:PSS substrate, namely the (*ab*)–plane and the (*bc*)–

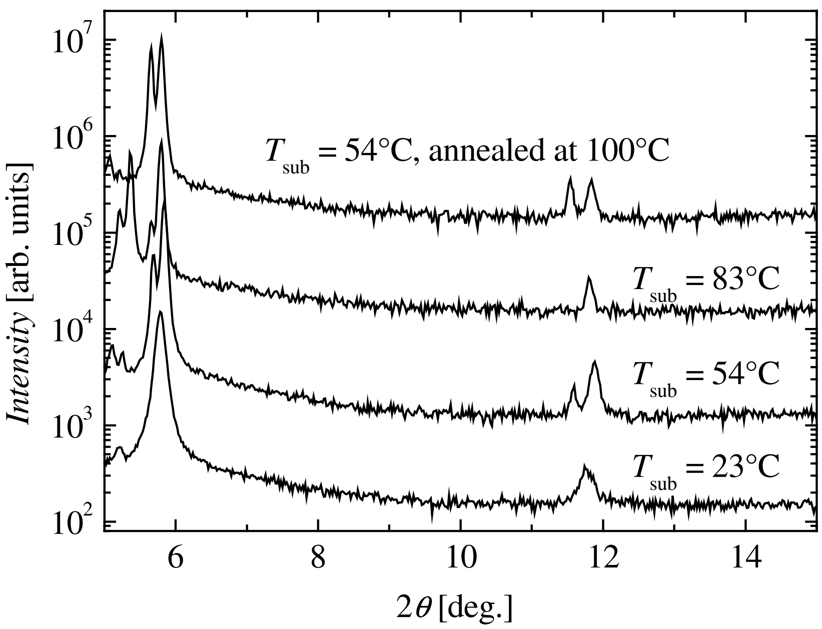

Figure 5.5 XRD (θ, 2θ) (λ = 1.540 Å) diffractogram of Ooct-OPV5 thin films vacuum-deposited on ITO/PEDOT:PSS substrates at different substrate temperatures T_{sub}. The top trace was measured on a thin film that was post-growth annealed at 100°C for 5 min.

plane. This is in agreement with the ED pattern, as we will see later. The fact that in polycrystalline thin films of Ooct-OPV5 two contact planes with the substrate co-exist was not yet recognized. It has been rather assumed that solely the *ab* –plane forms contact with the substrate. A consequence of our observation is that two crystal orientations co-exist with respect to the electric field direction in a planar device structure. While for one possible orientation, the conjugated backbone is nearly perpendicular to the field direction in a planar diode structure, it is nearly parallel for the other (Fig. 5.1). Hence, the overall charge carrier transport properties in thin films consisting of crystals of both orientations will be strongly influenced by their relative occurrence.

In contrast to the 16.9 Å and 16.4 Å reflections, both the 15.50 Å and 15.15 Å reflections could not be indexed on basis of the known crystal structure. Since the 16.9 Å and 16.4 Å reflections coincide with the known bulk structure of single crystals, and the 15.50. Å and 15.15 Å reflections co-exist with the 16.9 Å and 16.4 Å reflections in thin films deposited at higher T_{sub}, one must ascribe the 15.50 Å and the 15.15 Å reflections to a low-temperature polymorph (hereafter α–phase), of which the structure is not known yet. Accordingly, the 16.9 Å and 16.4 Å reflections belong to a high-temperature polymorph (β–phase), of which the structure is equal to the known single crystal structure. Previously, the 15.15 Å reflection was indexed to the (002) plane [8], and its discrepancy in reticular distances towards a single crystal has been attributed to the flexibility of the octyloxy sidechains. The aliphatic layer between the conjugated backbones has been regarded to be highly compressible, resulting in a deformability of

Table 5.2: d_{hkl} reticular distances observed by XRD (θ,2θ) (λ = 1.540 Å) in Ooct-OPV5 thin films deposited on ITO/PEODT:PSS substrates at different T_{sub}.

	α-phase d_{hkl} [Å]		β-phase d_{hkl} [Å]	
T_{sub} [° C]	(002)	(200)	(002)	(200)
23	15.28	-	-	-
54	15.50	15.15	-	-
83	15.60	15.22	16.9	16.4
54 (annealed at 100°C, 5min)	15.60	15.20	-	-

the unit cell. Such a deformation will certainly involve a change in the *c*–axis length and/or the monoclinic angle, and will, furthermore, depend on the thin-film preparation conditions.

For this section we can conclude that polymorphism exists in thin films of Ooct-OPV5 deposited on an ITO/PEDOT:PSS substrate with a specific trend in appearance for each polymorph upon change in T_{sub}. While the β–phase preferably exists in the high T_{sub} regime, the α–phase was observed also for low-T_{sub} films. Since, however, the structure of the low-temperature polymorph is not known, the impact on the charge carrier transport properties is difficult to predict. In this context, the reticular distances d_{002} and d_{200} may merely give indications about the strength of the ππ –interaction or the hopping distance between adjacent molecules along the current direction.

5.2.2 Domain structure and homoepitaxy

For T_{sub} = 90°C, we obtained the ED pattern of single domains (β–phase) of a few microns in size with selected area electron diffraction (SAED). The unveiled SAED patterns were compared to simulated diffraction patterns derived from the Ooct-OPV5 single crystal structure. Interestingly, the SAED patterns could only be simulated by superposing the ED patterns of two crystal orientations, namely the [102] and [201] zone axes (orientation of the electron beam with respect to the unit cell of the micro-crystal) (Fig. 5.6). The 9.13 Å reflection in the ED pattern of Fig. 5.4, for instance, indexed as ($20\underline{4}$) cannot be accounted by using exclusively a [102] zone axis even for higher order layer lines. However, the reflection is perfectly reproduced in the ED pattern obtained for a [201] zone axis. This suggests that within the same Ooct-OPV5 crystal, sub-domains with [102] and [201] orientations co-exist. The 9.13 Å reflection has also been observed for single crystals of Ooct-OPV5 [8].

In accordance with the computer-simulated ED patterns for the [102] and [201] zone axis, the most intense reflections were indexed to the (020) direction with d_{020} = 3.86 Å. Consequently, and in agreement with the XRD data, the "π-stacking-axis" lies

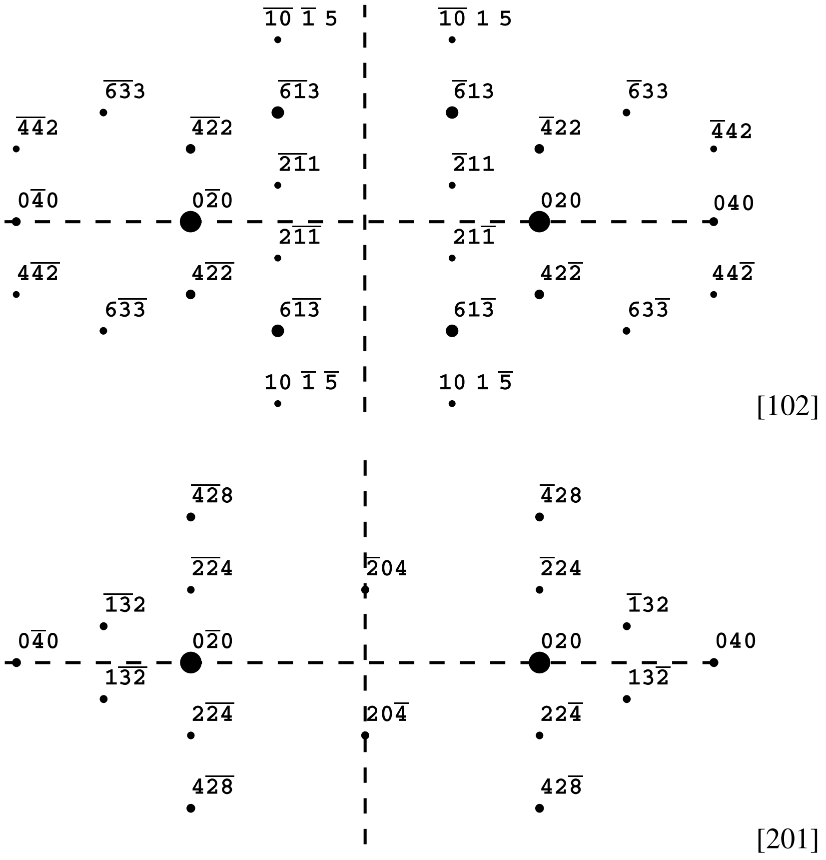

Figure 5.6 Computer-simulated ED pattern of an Ooct-OPV5 single-crystal for the [102] and the [201] zone axis.

in the plane of the substrate for both crystal orientations. However, typical molecular separations for π -stacked molecules are in the range of 3.3-3.4 Å [19], indicating that even in the direction of the "π-stacking-axis" no strong ππ-interaction exists.

The co-existence of [102] and [201] orientations for the same crystal can be explained by homoepitaxy of the (100) face on the (001) face and vice versa (Fig. 5.7). This explanation is in perfect agreement with the XRD diffractograms. Indeed, the (*ab*)- and (*bc*)-planes of the high-temperature polymorph share almost the same unit-cell parameters, since *a* and *c* are almost equal in length (*a* = 36.2 Å versus *c* = 36.6 Å). Considering the bulk crystal structure of Ooct-OPV5, a rotation of the unit cell along the [101] twin axis exchanges the (*ab*)- and (*bc*)-planes. For both orientations, the "π-stacking-axis" is situated in the plane of the substrate. Such a twinning mechanism is known to induce fine structures, e.g. streaking in the ED pattern, as it is observed for the (20$\underline{4}$) and (61$\underline{3}$) reflections (Fig. 5.4). The streaking is typically caused by strain at a twin interface, which is likely to occur in our case, since the *a* and *c* lengths are slightly different. We can anticipate that the presence of strain at the twin

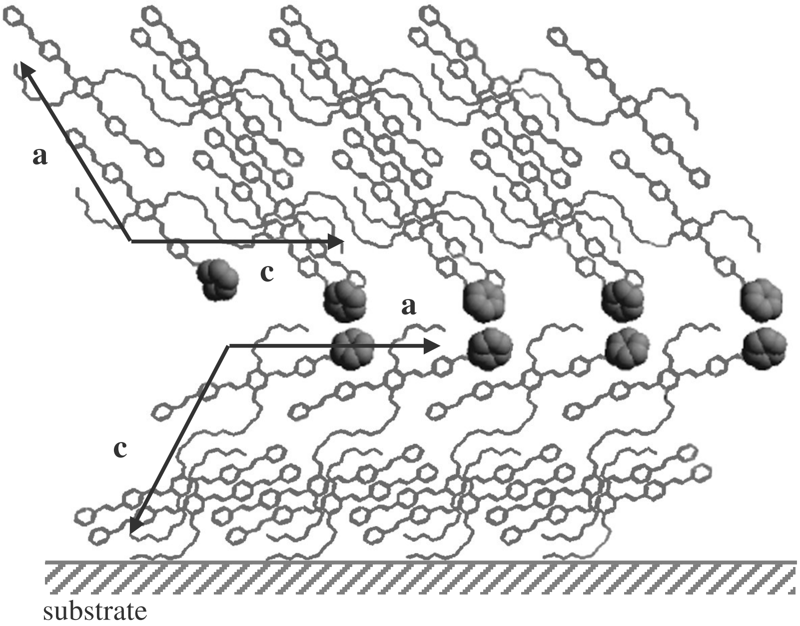

Figure 5.7 Simulation of the interface between the two possible domains of a [102] and a [201] zone axis. Matching of the terminal phenyl groups can be observed.

interface directly translates in charge carrier traps or scatter centers, which might limit the charge carrier transport through a crystal of Ooct-OPV5. However, if we model the interface between (*ab*)- and (*bc*)-planes as shown in Fig. 5.7, a nice matching of the positions of the terminal phenyl groups of the OPV-core in the (*bc*)-plane with the corresponding phenyl groups in the (*ab*)-plane is observed. It is possible that an improved ππ-interaction between the terminal phenyl rings at the interface between the (*ab*)- and (*bc*)-planes favors the homoepitaxy phenomenon, but, moreover, assists charge transfer across the twining interface.

5.2.3 Annealing of Ooct-OPV5 thin films

The evaluation of the film morphology upon post-growth thermal treatment of the Ooct-OPV5 thin films has been extensively studied earlier [8]. In accordance to our observations, annealing resulted in an increase of the mean domain size and a roughening of the thin films, just as in films prepared at higher substrate temperatures. Yet, an important difference remains as can be seen from the XRD diffractograms presented in Fig. 5.5. While the deposition of Ooct-OPV5 at elevated temperature (84°C) clearly resulted in the appearance of the β -phase, no phase transformation from α to β occurred during annealing at 100°C. The post-growth annealing of Ooct-OPV5 thin films deposited on ITO/PEDOT:PSS substrates thus results in a different morphology than the deposition of Ooct-OPV5 at high temperature, suggesting that also the semiconductor properties of these films are not alike.

5.2.4 Cathode morphology

Calcium deposited on top of Ooct-OPV5 exhibited a granular texture of small spherically shaped domains with a mean diameter bigger than 10 nm (Fig. 5.2). Yet, the contribution of the Ca film to the roughness of the electrode is below the one of the underlying Ooct-OPV5 film. Accordingly, Ca simply decorates the polycrystalline Ooct-OPV5 film. Nonetheless, the overlying Ca layer formed a pinhole-free film and, hence, we can regard the Ca cathode as being continuous over the whole electrode area.

5.3 Electrical characterization of Ooct-OPV5-based thin films

5.3.1 Hole transport in thin films of Ooct-OPV5

The transport properties of Ooct-OPV5 thin films where investigated by transient electroluminescence (EL) measurements [20-23] in a planar diode structure. The LEDs were exposed to a rectangular voltage pulse with a typical pulse duration >10 µs, and a photomultiplier coupled to a digital oscilloscope followed the time evolution of the emitted light. Typically, a double exponential increase of the EL signal in time was observed. The transit time of the faster carrier species - in organic semiconductors usually the holes - is then given by the initial delay before the first light is emitted and the time the first exponential EL increase dominates the temporal development of the EL signal [21]. Out of the transit times, we obtained the hole mobility in dependence of the electric field for different morphologies of Ooct-OPV5 thin films (Fig. 5.8).

The hole mobility obtained from Ooct-OPV5 thin-film LEDs prepared at T_{sub} = rt was field-activated according to Gill's equation with a field activation factor of 2.7×10^{-4} $(\mathrm{m/V})^{1/2}$ and a zero field hole mobility μ_0 of 3.6×10^{-6} $\mathrm{cm^2/Vs}$. This is in accordance with the hole mobility found by Geens *et al.*, employing field-effect measurements [2]. For thin films deposited at elevated T_{sub}, the hole mobilities of Ooct-OPV5 were still field-activated, but the field activation factor strongly decreased, while the zero field hole mobility increased. However, due to the pronounced roughness of Ooct-OPV5 thin films, especially when deposited at elevated T_{sub}, measurements in a planar device structure are strongly biased, since the device thickness varies locally, affecting the transit distance and the electric field. This situation is unavoidable and results in significant measurement errors. Nonetheless, the trend in the evolution of the hole mobility upon change in T_{sub} is meaningful.

The change in hole mobility upon varied T_{sub} is most likely related to a variation in crystal size and perfection. While for devices prepared at T_{sub} = rt, the mean crystal size was smaller than 50 nm in diameter, crystal diameters exceeded even the average film thickness at high T_{sub}, thereby strongly reducing the number of grain boundaries that have to be traversed by charge carriers. Furthermore, the crystal perfection is expected to be enhanced when Ooct-OPV5 is deposited on a hot substrate, since the molecular reorganization in the crystals is facilitated. This results in a reduction of the trap density and diagonal and off-diagonal disorder in the film. Exclusively regarding the change in the hole mobility as disorder-controlled, the correlated Gaussian disorder model (CDM) can be applied [24, 25]. The decrease of the field activation factor and the simultaneous increase of the zero field hole mobility upon increased T_{sub} then translate in a diagonal disorder reduction of about 0.02 eV. This indicates a considerable improvement in the molecular order upon T_{sub} increase. Certainly, however, the validity of the CDM in polycrystalline films is limited. The decrease of the trap density and/or scatter centers upon T_{sub} increase is also in favor of a higher hole mobility, but the existence of homoepitaxial layers in a grain may be seen as an intrinsic limit for this reduction. The crystallite perfection of a grain would thus be limited by the extent of homoepitaxial growth.

Besides the crystal size and perfection, the crystal structure varied upon changed T_{sub}. While films prepared at low T_{sub} consisted mainly of the α–polymorph, the β-polymorph became more and more abundant upon increase of T_{sub}. Concomitantly, the crystal plain that preferably interacts with the PEDOT:PSS substrate changed. Obviously, the relative presence of the two different polymorphs and their possible crystal orientations with respect to the preferential current direction influence the overall hole transport properties of the corresponding polycrystalline layer. At high T_{sub}, for example, rather the (bc)-plane of the β-polymorph was found to be in contact with the substrate than the (ab)-plane. However, once the (ab)-plane of a crystal forms contact with PEDOT:PSS, the oligomeric main chain is quasi perpendicularly oriented towards the current direction (see Fig. 5.1), while it is almost parallel once the (bc)-plane touches the substrate. The hopping distance between adjacent molecules is

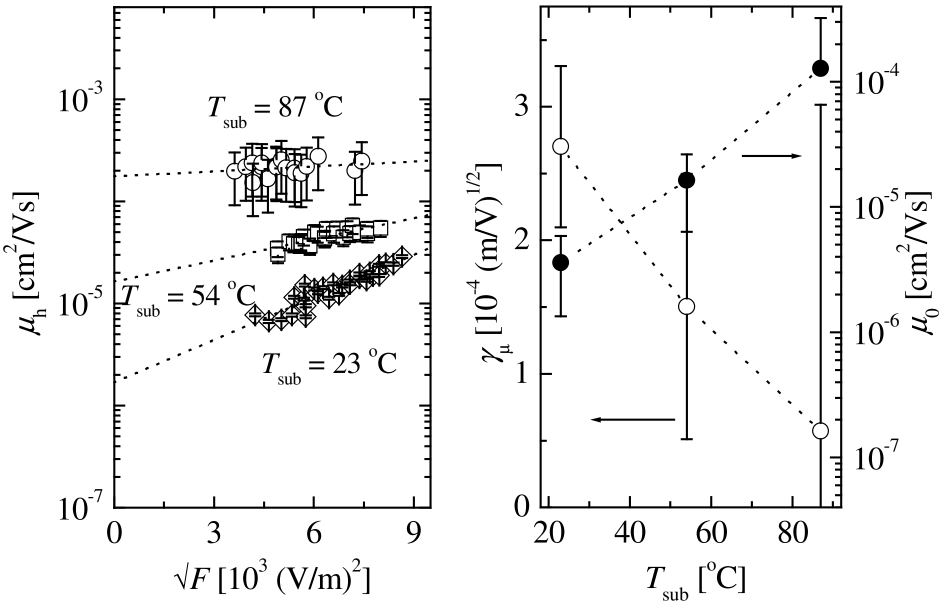

Figure 5.8 *Left*: Hole mobility of Ooct-OPV5 measured in thin films that were deposited at different T_{sub}. *Right*: Field activation factor γ_μ (○) and zero field hole mobility μ_0 (●) of Ooct-OPV5 for different T_{sub}. Error bars indicate the error due to roughness of the thin film.

furthermore longer in the former case than in the latter. As a consequence, charge transport in films deposited at higher T_{sub} is expected to be comparatively efficient.

However, from Table 5.2 it can be seen that the reticular distances (002) and (200) of the high-temperature β–polymorph exceeded the ones of the low-temperature α–polymorph. This might on one hand result from an increased separation distance between adjacent molecules, e.g. induced by a conformational change of the highly flexible octyloxy sidechains. In such a situation, the ππ–interaction along the current direction would be reduced just as the hopping distance between adjacent molecules would get longer. Consequently, the charge carrier mobilities of crystals grown at room temperature would be superior and less field-activated compared to the ones prepared at elevated temperature. According to the though observed increase in hole mobility with increasing T_{sub}, crystal size, purity and orientation would need to dominate the evolution of the hole transport properties upon T_{sub} change. On the other hand, the disparity of the reticular distances between α–and β–polymorph might be accompanied by dissimilar molecular orientations towards the current direction. Hence, in order to judge in which way the appearance of the β-polymorph at elevated temperatures may influence the hole transport, information about the crystal structure of the α–polymorph is obviously required, particularly concerning the molecular

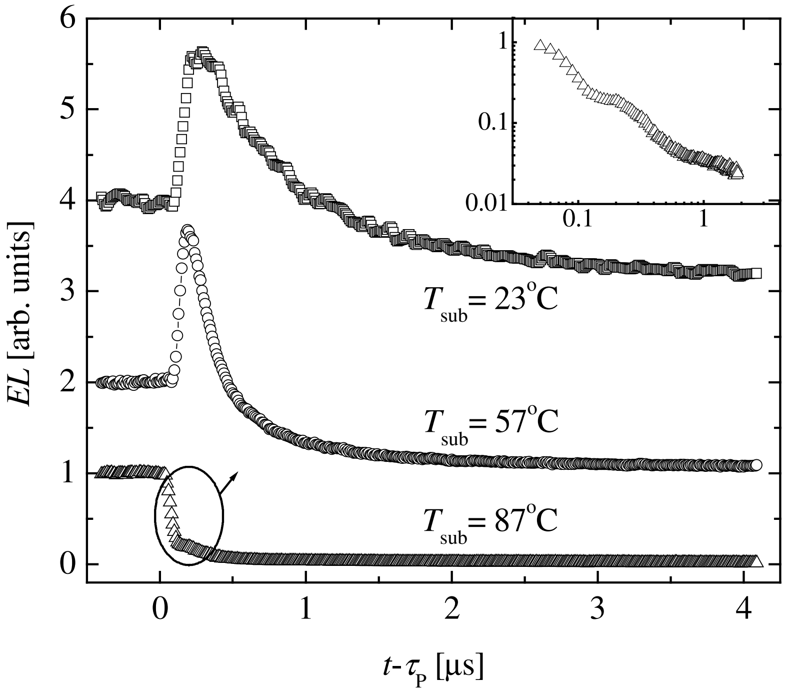

Figure 5.9 Switch-off dynamics of transient EL signals obtained from ITO/PEDOT:PSS/Ooct-OPV5/Ca devices prepared at different T_{sub}. Parameters were τ_p ~ 1 ms and F ~ 4.5×10^7 V/m. *Insert*: Log-Log presentation of the overshooting measured with a sample prepared at T_{sub} = 87°C.

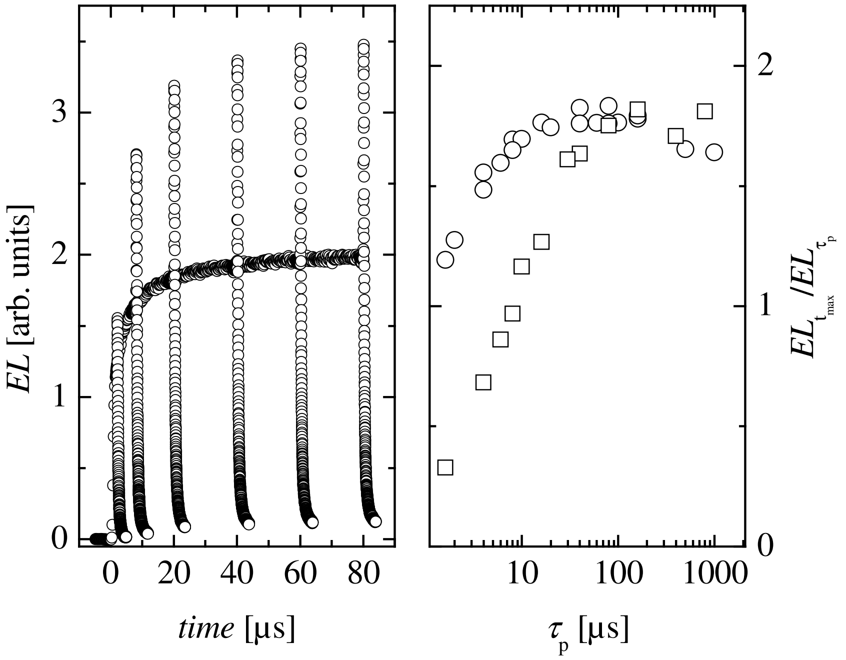

Figure 5.10 *Left*: Time evolution of the EL signal of an ITO/PEDOT:PSS/Ooct-OPV5/Ca device prepared at 57°C for different τ_p versus time. *Right*: Ratio of EL peak amplitude and EL steady-state amplitude for different T_{sub}. $F \sim 6\times10^7$ V/m.

orientations towards the preferential current direction and the intermolecular distance of nearest neighbor molecules.

In conclusion, we can say that the improved hole mobility upon increase of T_{sub} and the concomitantly reduced field activation can be understood on basis of a reduction of the grain boundaries and trap and/or scatter-center densities, and improved intermolecular order. The transition from the α– to the β–polymorph might have an additional impact on the hole transport, which needs to be confirmed by structural analysis of the low-temperature polymorph.

5.3.2 Electroluminescence overshoot

For LEDs based on thin films of Ooct-OPV5, the EL transient measurements revealed a peak-like increase of the EL signal after a rapid switch-off of the applied bias (Fig. 5.9). The magnitude of the peak was found to be dependent on the thin-film morphology. While the effect was almost undetectable for films deposited at T_{sub} = 87°C, the peak amplitude considerably exceeded the steady–state EL level when films were deposited below 60°C. In addition, the pulse duration τ_p influenced the peak amplitude substantially as can be seen from Fig. 5.10, while its dependence on the amplitude of the voltage pulse was minor (Fig. 5.11).

EL overshoot upon rapid switch-off of the applied bias has been previously observed in single–layer and double–layer LED systems [21, 26-28]. In general, the origin of the overshooting was attributed to the release and redistribution of accumulated and/or trapped charges in a region of improved radiative recombination probability. Particularly, in single–layer LEDs, the appearance of the overshoot was explained by the recombination of electrons trapped in the bulk of the organic semiconductor and holes being previously accumulated at the semiconductor/cathode interface. The accumulation of holes at the cathode has been related to the presence of a thin blocking layer of Al_2O_3 between the semiconductor and the used aluminum cathode and/or interfacial traps. Upon switch–off of the stimulus, the accumulated holes redistribute out of the quenching zone near the cathode and radiative recombination with the electrons is efficient, resulting in the peak-like behavior of the EL signal. We anticipate, that when using Ca as a cathode, it is even more likely that a thin oxide layer is formed between the metal and the Ooct-OPV5 film. Under device operation, accumulation of holes at the semiconductor/cathode interface is therefore very likely. Consequently, the EL overshoot can be rationalized by the release of holes out of the quenching zone near the cathode upon voltage switch–off and the radiative recombination of these holes with electrons trapped in the bulk material.

In the sketched scenario, the time evolution of the EL signal after rapid switch-off of the external voltage is related to the transit time the released holes require to reach the trapped electrons. Lupton *et al.* [27] calculated the relative time evolution of the EL overshoot by solely assuming geminate recombination (GR)-controlled EL:

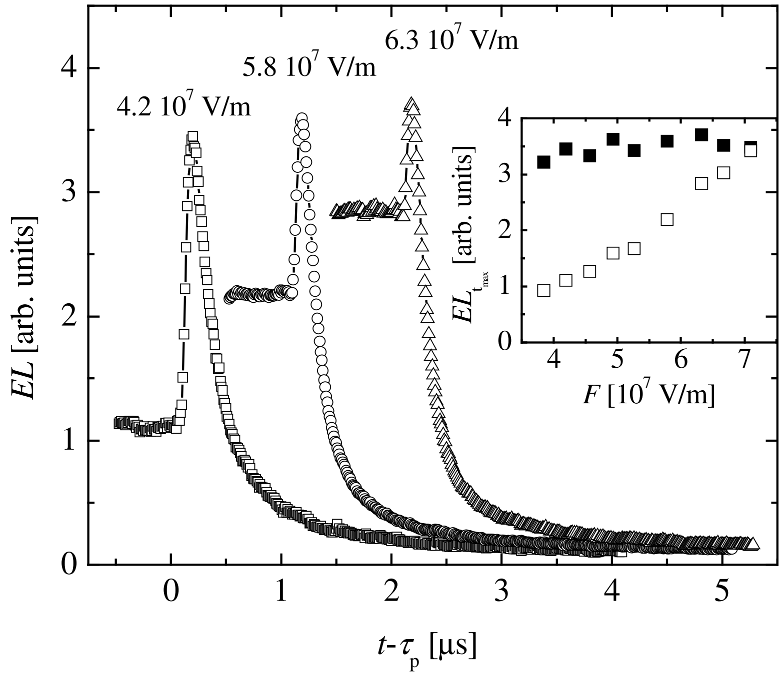

Figure 5.11 EL signal versus time upon rapid switch-off of the applied bias for an ITO/PEDOT:PSS/Ooct-OPV5/Ca device prepared at 57°C for different voltage pulse amplitudes. τ_p = 0.5 ms. The traces are shifted in time for clarity. *Insert*: Development of the EL peak amplitude (■) and the EL amplitude at t = τ_p (□) of the same sample with the field amplitude of the pulse.

Eq. 5.1

$$\frac{j_{t>\tau_p}(t)}{j_{t=\tau_p}(t)} \propto -\frac{\partial p_{\mathrm{gp}}(t)}{\partial t}$$

Here, we define $t = \tau_{\mathrm{p}}$ as the time when the voltage pulse is switched off. In Eq. 5.1, $j_{\mathrm{t}=\tau_{\mathrm{p}}}$ is the steady-state current density due to GR processes (EL current density) and $j_{\mathrm{t}>\tau_{\mathrm{p}}}$ is the EL current density after bias switch-off. $-\partial p_{\mathrm{gp}}(t)/\partial t$ is the GR-controlled recombination rate and $p_{\mathrm{gp}}(t)$ is, hence, the survival probability of geminate pairs. Even though the initial distribution of electrons and holes is planar, Lupton *et al.* approximated it to be of spherical symmetry [29] and assumed diffusion as the dominant redistribution process of charges [30]. Under these assumptions, the survival probability of geminate pairs generated at $t=\tau_{\mathrm{p}}$ is given by $p_{\mathrm{gp}}(t) \propto 1 - \mathrm{Erf}\left(\mathrm{r}_0 / \sqrt{4\pi D(t-\tau_{\mathrm{p}})}\right)$, where D is the diffusion coefficient of the majority carriers and r_0 defines the initial separation length of the recombination pairs. Obviously, r_0 finds its lower limit in the distance of total EL quenching at the electrode, being approximately 10 nm. Assuming the Einstein relationship $D = kT\mu_h / q$, with q as the electron charge, k as the Boltzmann constant, T as the temperature, and μ_{h} as the hole mobility obtained from transient EL measurements, the simulated EL peak evaluation in time perfectly followed the experimental observation (Fig. 5.12). The fit required a r_0 of about 13 nm, which is very close to the lower limit of r_0. However, the time delay between voltage switch–off and appearance of the peak

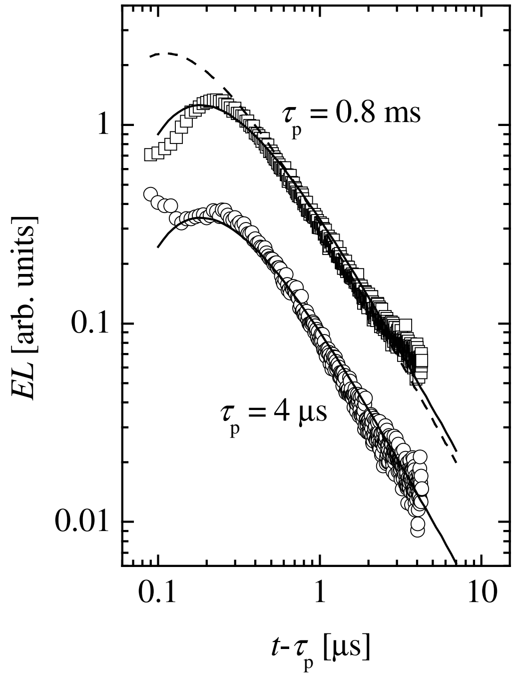

Figure 5.12 EL versus time for an ITO/PEDOT:PSS/Ooct-OPV5/Ca device prepared at room temperature. Lines are fits according to Eq. 5.1 with μ_{h} = 1.8×10^{-5} cm^2/Vs from EL transient measurements and r_0 = 13 nm (—) and 10 nm (---).

maximum $t_{\max}$ was always close to the RC time of our measurement circuit, typically around 0.2 μs for all systems and conditions. Hence, the time resolution was not sufficient to resolve the initial shape of the EL overshoot, particularly the peak maximum itself. As a consequence, the unveiled 13 nm have to be regarded as the upper limit of r_0 as depicted in Fig. 5.12. The fast on–set of the EL overshoot below 0.2 μs can therefore be attributed to a typical EL quenching length of 10 nm in combination with the high hole mobility found for Ooct-OPV5, resulting in fast transit times of holes out of the quenching region.

Besides its dependence on the recombination rate, the relative time evolution of the EL overshoot is proportional to the number of correlated "hot" holes per "radiative" electron. This number quantifies, among other things, the trapping and accumulation of holes and electrons involved in the process. Yet, once τ_p is smaller than the time required to fully establish the charge accumulation and trapping, the number of correlated "hot" holes per "radiative" electron is supposed to be strongly reduced, resulting in a weakened overshoot effect. From Fig. 5.10 it can be seen that the peak amplitude was constant for $\tau_p >> 0$, while it indeed decreased considerably once τ_p came close to the transit times of the charge carriers. Likewise, upon T_{sub} increase, the electron trap density in the Ooct-OPV5 thin film reduced and the overshoot effect diminished, as it can be seen from Fig. 5.9.

Regarding the described process as being responsible for the observed EL overshoot, the effect should be observable in similar systems, such as ITO/PEDOT:PSS/MEH-OPV5/Ca LEDs, because the elemental requirements for the overshoot are equivalently fulfilled, namely trapping of charges, in particular electrons, and the existence of a CaO layer between semiconductor and cathode. However, no time-delayed EL peak upon rapid voltage switch-off was detected in such systems, questioning the presence of a CaO layer. An alternative qualitative explanation of the EL overshoot excluding the presence of a CaO layer can be given, considering the findings in bi-layer LEDs [26]. The principles sketched above also hold true in this case, however, the polycrystalline nature of Ooct-OPV5 thin films is addressed. Upon biasing the LED, holes travel through a grain of the polycrystalline film and might be blocked at the grain boundary, where they try to escape the grain. For holes, this grain boundary is closer to the cathode. The blocking may be related to the strongly reduced mobility at the grain boundary or the charges might simply be trapped. In turn, electrons can be accumulated near the grain boundary in the same grain, but closer to the anode. Under device operation, EL then preferably occurs at the grain boundaries. Upon switch-off of the external electric field, the charges redistribute in the grain. After a certain transit time, electrons and holes meet and finally recombine radiatively, which results in a time-delayed EL signal after bias switch-off. Upon increase in T_{sub}, less grain boundaries are present and, consequently, the overshooting effect diminishes. In order to explain, however, why the time-delayed EL overshoot is higher than the steady-state EL, an improved radiative recombination probability in the grain compared to the grain boundary is required. This requirement is met since the Langevin excitation generation is proportional to the effective charge carrier mobility, which is higher in the crystal than at the grain boundary. Consequently, the Langevin recombination rate in the crystal is higher than the one at the grain boundary [31]. Moreover, H-like aggregation might appear more frequently at the grain boundary than in the crystal, which further reduces the radiative decay rate.

In conclusion, two qualitative explanations can be given for the appearance of the time-delayed EL spike after bias switch-off, both addressing the nature of polycrystalline thin films. Qualitatively, the phenomenon is explained by charge accumulation during device operation and the subsequent redistribution of charges in regions of improved recombination probability, once the external voltage is switched off. In the first proposed model, electrons are trapped in the bulk and holes are accumulated at a CaO layer close to the cathode, while the second model deals with the fact that charge carriers can be accumulated at grain boundaries present in the polycrystalline film.

5.4 Conclusion

The thin-film morphologies of vacuum-deposited Ooct-OPV5 on an anode of ITO/PEDOT:PPS at different substrate temperatures were investigated. The growth mechanism was found to be of Volmer-Weber type, indicating weak wetting of the Ooct-OPV5 films with the PEDOT:PSS substrate. In general, Ooct-OPV5 thin films consisted of two polymorphs with one being predominant when films were deposited at low T_{sub} and another solely existing at T_{sub} above 60°C. The structure of the high-temperature polymorph coincided with the known single crystal structure of Ooct-OPV5, while the one of the low temperature polymorph is currently not known. It was demonstrated, that two crystal orientations of the high-temperature polymorph towards the substrate plane were present. Yet, the impact of the relative occurrence of the two polymorphs and their possible crystal orientations towards the preferential current direction on the hole transport properties could not be fully explained. Nevertheless, the evolution of the hole mobility upon changed film morphology could be sufficiently understood on basis of changes in crystal size and quality. The hole mobility considerably improved for polycrystalline films with larger crystalline domains and became less field-dependent. The importance of crystal size and quality for the device operation was, moreover, reflected in the switch-off dynamics of EL in single–layer LEDs based on Ooct-OPV5 thin films. For film morphologies of small crystalline domains and poor crystal quality, a time-delayed peak-like increase of the EL with a rather long decay time was revealed, which we relate to charge accumulation and/or trapping during operation and redistribution of the accumulated charges in a region of improved radiative recombination probability upon voltage switch–off. Once the crystal size increased and the crystal quality improved, the overshoot effect diminished.

References

[1] F. Garnier, G. Horowitz, G. Peng and D. Fichou, Adv. Mater. **2**, 592 (1990).

[2] W. Geens, D. Tsamouras, J. Poortmans and G. Hadziioannou, Synth. Met. **122**, 191 (2001).

[3] C. Adachi, A. Tsutsui and S. Saito, Appl. Phys. Lett. **56**, 799 (1990).

[4] J. Kalinowski, J. Phs. D: Appl. Phys. **32**, R179 (1999).

[5] S. E. Shaheen, C. J. Brabec, N. S. Sariciftci, F. Padinger, T. Fromherz and J. C. Hummelen, Appl. Phys. Lett. **78**, 841 (2001).

[6] C. Melzer, V. V. Krasnikov and G. Hadziioannou, Appl. Phys. Lett. **82**, 3101 (2003).

[7] H. E. Katz, S. F. Bent, W. F. Wilson, M. L. Schilling and S. B. Ungashe, J. Am. Chem. Soc. **116**, 6631 (1994).

[8] *Thesis:* R. E. Gill, *Design, synthesis and characterization of luminescent organic semiconductors*, Chemistry Department Rijksuniversiteit Groningen, Groningen (1996).

[9] R. E. Gill, A. Meetsma and G. Hadziioannou, Adv. Mater. **8**, 212 (1996).

[10] D. Tsamouras, G. Palasantzas and J. T. M. De Hosson, Appl. Phys. Lett. **79**, 1801 (2001).

[11] G. Palasantzas, D. Tsamouras and J. T. M. De Hosson, Surface Science **507-510**, 357 (2002).

[12] A. C. Arias, M. Granström, D. S. Thomas, K. Petritsch and R. H. Friend, Phys. Rev. B **60**, 1854 (1999).

[13] L. B. Groenendaal, F. Jonas, D. Freitag, H. Pielartzik and J. R. Reynolds, Adv. Mater. **12**, 481 (2000).

[14] D. Tsamouras and G. Palasantzas, Appl. Phys. Lett. **80**, 4528 (2002).

[15] G. Palasantzas and J. Krim, Phys. Rev. Lett. **73**, 3564 (1994).

[16] W. E. Wolf and J. Villain, Europhys. Lett. **13**, 389 (1990).

[17] Z. W. Lai and S. Das Sarma, Phys. Rev. Lett. **66**, 2348 (1991).

[18] M. D. Ward, Chem. Rev. **101**, 1697 (2001).

[19] M. S. Dresselhaus and G. Dresselhaus, Adv. Phys. **30**, 139 (1981).

[20] P. W. M. Blom and M. C. J. M. Vissenberg, Phys. Rev. Lett. **80**, 3819 (1998).

[21] D. J. Pinner, R. H. Friend and N. Tessler, J. Appl. Phys. **86**, 5116 (1999).

[22] T. C. Wong, J. Kovac, C. S. Lee, L. S. Hung and S. T. Lee, Chem. Phys. Lett. **334**, 61 (2001).

[23] J. Wang, R. G. Sun, G. Yu and A. J. Heeger, J. Appl. Phys. **91**, 2417 (2002).

[24] S. V. Novikov, D. H. Dunlap, V. M. Kenkre, P. E. Parris and A. V. Vannikov, Phys. Rev. Lett. **81**, 4472 (1998).

[25] P. W. M. Blom and M. C. J. M. Vissenberg, Mater. Sci. Eng. **27**, 53 (2000).

[26] V. R. Nikitenko, V. I. Arkhipov, Y.-H. Tak, J. Pommerehne, H. Bässler and H.-H. Hörhold, J. Appl. Phys. **81**, 7514 (1997).

[27] J. M. Lupton, V. R. Nikitenko, I. D. W. Samuel and H. Bässler, J. Appl. Phys. **89**, 311 (2001).

[28] J. Pommerehne, D. V. Nikolaenkov, V. R. Nikitenko and H. Bässler, J. Appl. Phys. **90**, 5554 (2001).

[29] K. M. Hong and J. Noolandi, J. Chem. Phys. **68**, 5163 (1978).

[30] A. Mozumber, J. Chem. Phys. **48**, 1659 (1968).

[31] D. J. Pinner, R. H. Friend and N. Tessler, Appl. Phys. Lett. **76**, 1137 (2000).

6

Interface effects and electrical conduction in single-layer organic diodes

---

Abstract

The energy barrier at the metal/organic interface determines the charge injection current through a diode and depends on the interactions between the organic semiconductor and the metal electrode. In order to gain information about the injection barriers in organic diodes, the energy diagrams of small organic molecules on top of metals were determined by ultraviolet photoelectron spectroscopy (UPS). Concomitantly, conductivity measurements were performed on single-layer diodes based on the same organic semiconductors and metals. The current-voltage dependencies of the investigated diodes are discussed in this chapter, considering the experimentally determined energy diagrams of the respective contacts.

6.1 Introduction

Charge carrier injection from a metal to an organic semiconductor is the limiting process that determines the current-voltage characteristic of a diode if the charge transport rate through the bulk exceeds the injection rate. In general, the injection current density depends on the energy barrier that charges need to overcome to be emitted into the semiconductor [1, 2]. For hole (electron) injection, this energy barrier ϕ is roughly given by the difference of the Fermi-level energy of the metal E_F and the energy E_{HOMO} (E_{LUMO}) of the highest occupied molecular orbital, HOMO (lowest unoccupied molecular orbital, LUMO), of the organic semiconductor. Since the injection-limited current density is proportional to the charge carrier density in the semiconductor that is established by excess charges of the metal, the injection-limited current density is proportional to $\exp[-q\phi/kT]$, where q is the electron charge, k is the Boltzmann's constant and T is the temperature. From *Chapter 4* it becomes apparent that the nature of the charge carrier transport through a diode can be altered by changing the injection barrier height. Injection-limited conduction is expected when ϕ is so large that no substantial space-charge built-up in the semiconductor is possible and, hence, a screening of the electric field and the concomitant reduction of the drift velocity of charge carriers is prevented [2-4].

When an organic molecule is deposited on a metal, the interaction between the two materials influences the charge injection barrier at their interface [5, 6]. For instance, the energy of a charged molecule is affected by the polarizability of its environment. If e.g. an electron is extracted from a molecule of the organic bulk, the surrounding molecules will be polarized, which results in a screening of the Coulomb interaction by the dielectric and, hence, in a reduction of its ionization potential. However, once the charge is placed on a molecule in the vicinity of a metal, the metal polarizes, which further reduces (increases) the ionization potential (electron affinity) of the organic material. Classically, this effect is described by the image charge potential [1]. The image charge potential in combination with an electrostatic potential arising from an externally applied voltage leads to the Schottky lowering $\Delta\phi$ of the injection barrier ϕ, which essentially determines the voltage dependence of the injection current (see *Chapter 3*). Several other interactions between metals and organic materials are known, such as charge transfer from the metal to the first mono-layer of the organic medium or distortion of the electron cloud at the metal surface upon adsorption of an organic molecule (Fig. 6.1), which result in vacuum-level shifts confined to the metal/organic interface [5]. These effects have been identified in several metal/organic systems and result in vacuum-level shifts as strong as 1 eV [5-11]. In Fig. 6.1, a schematic energy diagram of a semiconductor/metal contact illustrates that an interfacial vacuum-level shift leads to a change of the charge injection barrier ϕ and, hence, varies the charge injection current through a diode.

In this chapter, results from conductivity measurements performed on single-layer thin-film organic diodes are discussed, considering experimentally determined energy diagrams. While (*E*,*E*,*E*,*E*)-1,4-bis[(4-styryl)styryl]-2-methoxy-5-(2'-ethyl-

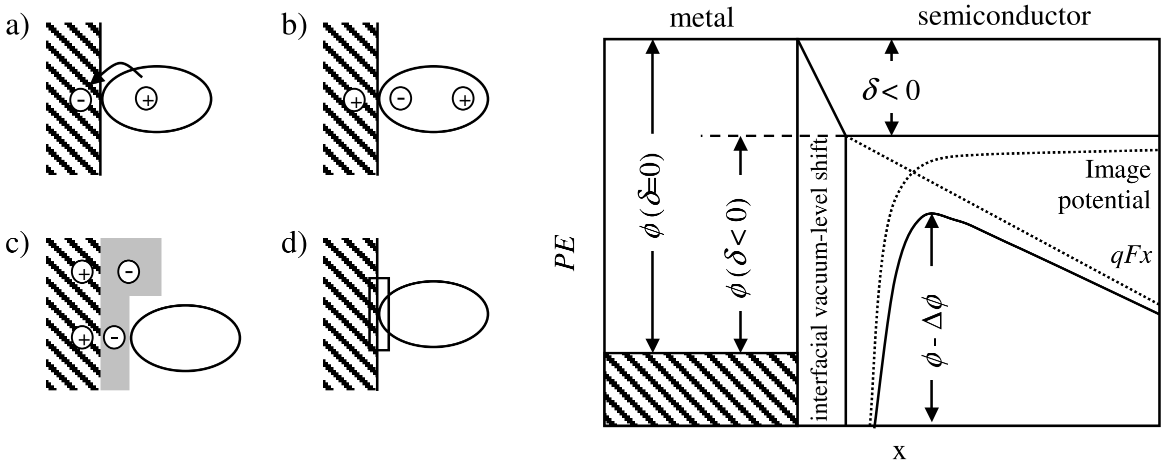

Figure 6.1 *Left*: Possible processes leading to a vacuum-level shift at a metal/organic interface [5]: a) charge transfer across the interface, b) mirror force, c) disturbance of the electron cloud extended into the vacuum at the metal interface upon adsorption of an organic moiety, d) charge buffering due to interfacial states. ***Right***: Schematic energy diagram of a metal/semiconductor interface with an interfacial vacuum-level shift of $\delta < 0$ for electron injection.

hexyloxy)benzene (MEH-OPV5) and buckminster fullerene (C_{60}) were used as organic semiconductors, Ag and Au were employed as electrode metals. The diodes were prepared and characterized in ultra-high vacuum (UHV), and were not exposed to any critical environment, which could bias the measurements. It will be demonstrated that strong vacuum-level shifts at the metal/organic interfaces have a significant impact on the charge carrier transport through these diodes.

6.2 Determination of the barrier height via UPS

The dispersion of the density of occupied states in solids is typically determined by photoelectron spectroscopy (PES), while inverse photoelectron spectroscopy probes the density of unoccupied states. Ultraviolet photoelectron spectroscopy (UPS) thereby provides information on the valence orbitals, for example, on the ionization potential of the organic semiconductor or the workfunction of metals, and, consequently, directly measures the hole injection barriers at metal/organic interfaces. Because PES techniques are highly surface-sensitive, measurements are typically performed under UHV conditions, since otherwise environmental moieties are immediately adsorbed on the surface. In general, the system has to be maintained at the same conditions during device preparation and characterization of the diode. Therefore, we performed the current-voltage (IV) measurements in a UHV electronic-test chamber attached to the UPS system. The electronic-test chamber, the diode design and the diode preparation strategy are described in *Chapter 2*.

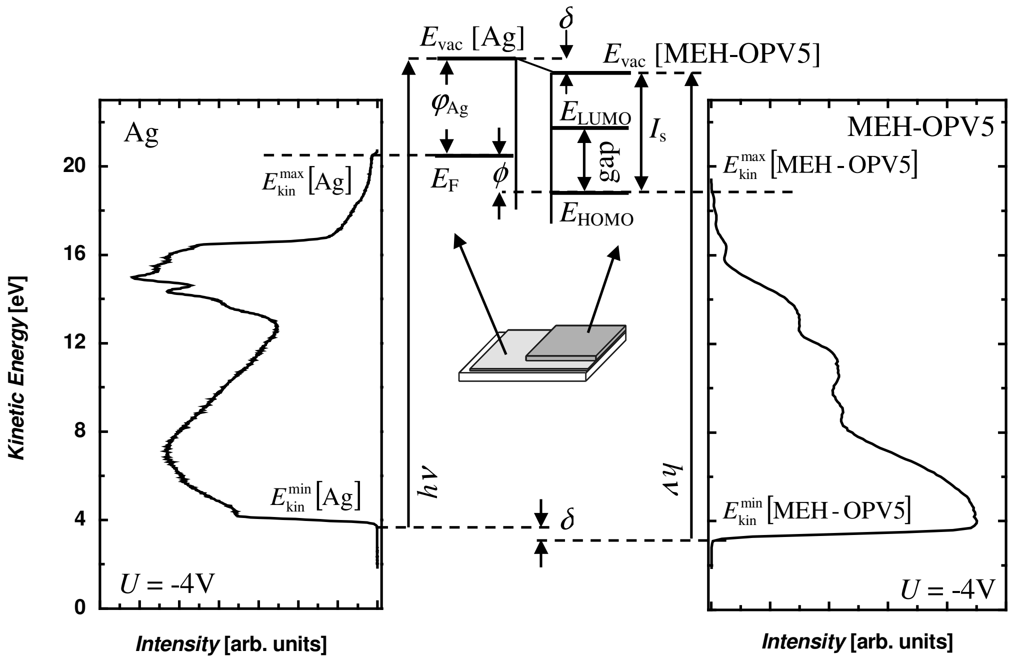

Figure 6.2 Determination of the energy band diagram at an Ag/MEH-OPV5 interface by UPS. UPS spectra were obtained at a potential difference of –4 V between sample and analyzer, permitting improved resolution of the low kinetic energy cut-off. E_{kin}^{min}, low kinetic energy cut-off of the spectra; E_{kin}^{max}, high kinetic energy cut-off of the spectra; $h\nu$, radiation energy (He I, 21.2 eV); E_{vac}, energy of vacuum-levels; E_F, energy of the metal Fermi-level; E_{HOMO}, energy of the HOMO level; E_{LUMO}, energy of the LUMO level; φ, workfunction of the metal; I_s, ionization energy of MEH-OPV5; δ, shift energy between the vacuum-levels of the metal and MEH-OPV5; ϕ, hole injection barrier.

Typical UPS spectra of polycrystalline Ag and of MEH-OPV5 are depicted in Fig. 6.2. The material under investigation was excited with ultraviolet light (He I, 21.2 eV) and the kinetic energy distribution of the emitted photoelectrons was measured. The kinetic energy of a photoelectron is, in principle, related to the orbital energy of the neutral molecule and to relaxation processes being involved in the photoemission process. The relaxation processes reduce the energy that is required to withdraw the electron from the molecule. In general, the contributions of the orbital and the relaxation energies to the binding energy cannot be discriminated. A frequently used approximation is to equal the binding energy of an electron with its negative orbital energy [12].

Once an electron has escaped the photo-excited molecule, it has to travel through the bulk, where inelastic scatter processes will occur. Inelastically scattered electrons (secondary electrons) usually result in a background signal in the recorded UPS spectrum with increased counts in the low kinetic energy wing. In order to release an electron from the medium into the vacuum, the kinetic energy of the photoelectron has to be insignificantly higher than the energy of the vacuum-level. As a result, an abrupt cut-off of the UPS spectrum at the kinetic energy equal to the vacuum-level energy occurs, which is resolved due to the background signal of secondary electrons.

The reconstruction of the energy diagram of a MEH-OPV5/Ag contact from UPS spectra is illustrated in Fig. 6.2. First, a UPS spectrum of a polycrystalline Ag layer was recorded. The workfunction φ of the metal is given by the difference of the vacuum-level energy and the Fermi-edge energy. The vacuum-level energy is simply the photon energy $h\nu$ added to the low kinetic energy cut-off $E_{\mathrm{kin}}^{\mathrm{min}}$ [metal], and the Fermi-edge energy is given by the high kinetic energy on-set $E_{\mathrm{kin}}^{\mathrm{max}}$ [metal] of the UPS spectrum:

Eq.6.1
$$\varphi = h\nu + E_{\mathrm{kin}}^{\mathrm{min}}[\mathrm{metal}] - E_{\mathrm{kin}}^{\mathrm{max}}[\mathrm{metal}]$$

$E_{\mathrm{kin}}^{\mathrm{min}}$ was determined by biasing the sample relative to the energy discriminator, thereby increasing the kinetic energy of the emitted electrons. This results in a corresponding rigid shift of the UPS spectra towards higher kinetic energies. After the characterization of the metal, an organic layer of MEH-OPV5 was deposited on the metal and an UPS spectrum was once more recorded. Similar to the workfunction of the metal, the ionization potential I_s of the organic material is given by:

Eq.6.2
$$I_s = h\nu + E_{\mathrm{kin}}^{\mathrm{min}}[\mathrm{organic}] - E_{\mathrm{kin}}^{\mathrm{max}}[\mathrm{organic}]$$

The vacuum-level mismatch δ due to interactions at the metal/organic interface is consequently:

Eq.6.3
$$\delta = E_{\mathrm{kin}}^{\mathrm{min}}[\mathrm{organic}] - E_{\mathrm{kin}}^{\mathrm{min}}[\mathrm{metal}]$$

Finally, the energy barrier for hole injection ϕ can be obtained by:

Eq.6.4
$$\phi = I_s - \varphi - \delta$$

A positive δ will reduce (increase) the hole (electron) injection barrier, while a negative δ will increase (reduce) it.

6.3 Diodes based on MEH-OPV5

The energy diagrams of MEH-OPV5/Ag and Au contacts obtained by UPS are depicted in Fig. 6.3 [13, 14]. While a vacuum-level shift of about -0.5 eV at the MEH-OPV5/Ag interface was found, a vacuum-level shift of even -1.2 eV was observed between the first mono-layer of MEH-OPV5 and Au. The exact mechanism that leads to these strong vacuum-level shifts at the metal/MEH-OPV5 interfaces is still not known. Park *et al.*, for instance, identified a partial charge transfer from Ca to comparable OPVs as the process that causes an energy level bending of 0.5 eV in a narrow space-charge region close to the metal/organic interface [15, 16]. The charge transfer is yet favored by the use of the low-workfunction metal Ca, which results in a

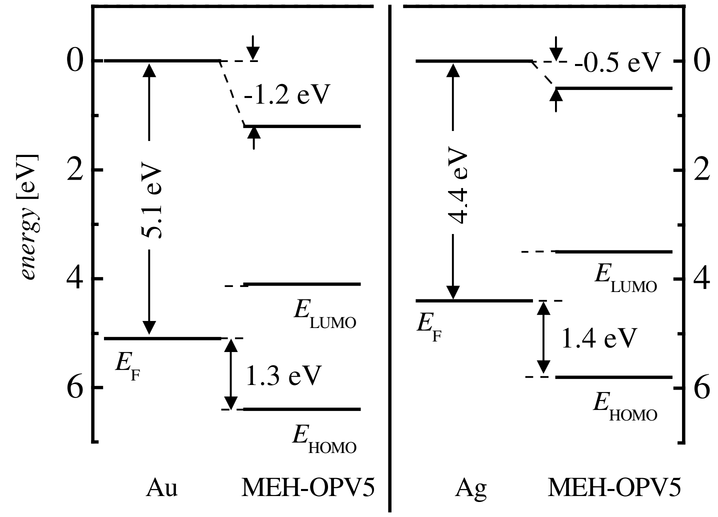

Figure 6.3 Energy diagram of an MEH-OPV5/Au and an MEH-OPV5/Ag contact obtained by UPS measurements [13, 14].

small energy barrier for electron emission from Ca to the LUMO of the OPV. Correspondingly, the HOMO of MEH-OPV5 is rather close to the Fermi-level of Au, which makes a charge exchange between both moieties energetically possible. The energy difference between the HOMO or the LUMO of MEH-OPV5 and the Fermi-level of Ag is, however, rather large, questioning any charge transfer between the two moieties. An alternative explanation of the revealed vacuum-level shifts could be the formation of a Schottky barrier, which yet requires free excess charges due to doping of the semiconductor. However, since the vacuum-level shifts are established in the first mono-layers, the required doping density would be unreasonably high. So far, it has been assumed that the observed vacuum-level shifts at the MEH-OPV5/Ag or Au interfaces are caused by the distortion of the electron cloud of the metal exposed to the vacuum at the metal surface upon adsorption of MEH-OPV5 molecules [14].

The vacuum-level shifts revealed by UPS have a dramatic consequence on the IV–characteristics of MEH-OPV5-based diodes. Assuming that the interfacial vacuum-

Table 6.1 Hole injection barriers ϕ obtained by UPS [13, 14] and estimated from IV-measurements for MEH-OPV5-based diodes.

Interface :	Au/MEH-OPV5	Ag/MEH-OPV5
ϕ_{UPS} [eV]	1.3	1.4
$\phi_{\text{UPS}}(\delta=0)$ [eV]	0.1	0.9
ϕ_{IV} [eV]	>0.9	>1.0

level shifts cannot be changed upon biasing the diode, the charge injection barriers at the cathode and the anode for hole and electron injection, respectively, are both in the range of 1 eV. In Table 6.1 the predicted injection barrier heights are listed. For these large injection barriers, the current is believed to be injection-limited, since charge carrier injection was identified as the limiting process for even much lower barriers (*Chapter 4*).

In Fig. 6.4, we present two typical IV–characteristics of Ag/MEH-OPV5/Au devices. In contrast to the IV–characteristics of comparable single-layer MEH-OPV5 devices presented in *Chapter 4*, the current densities observed here were solely governed by the leakage current through our setup, even for electric fields up to 10^8 V/m. Accordingly, a temperature decrease down to 153 K resulted in negligible variations of the current density-voltage dependencies. The actual currents flowing through the investigated diodes were, hence, most likely injection-limited as predicted by UPS. However, since the actual current densities were below the measured current densities, IV–measurements solely provide information on the minimally required injection barriers. By simulating the IV–characteristics with the charge injection model presented in *Chapter 3* and using the hole mobility data from *Chapter 4*, the minimally required hole injection barrier height was estimated to be ~0.9 eV, which corresponds

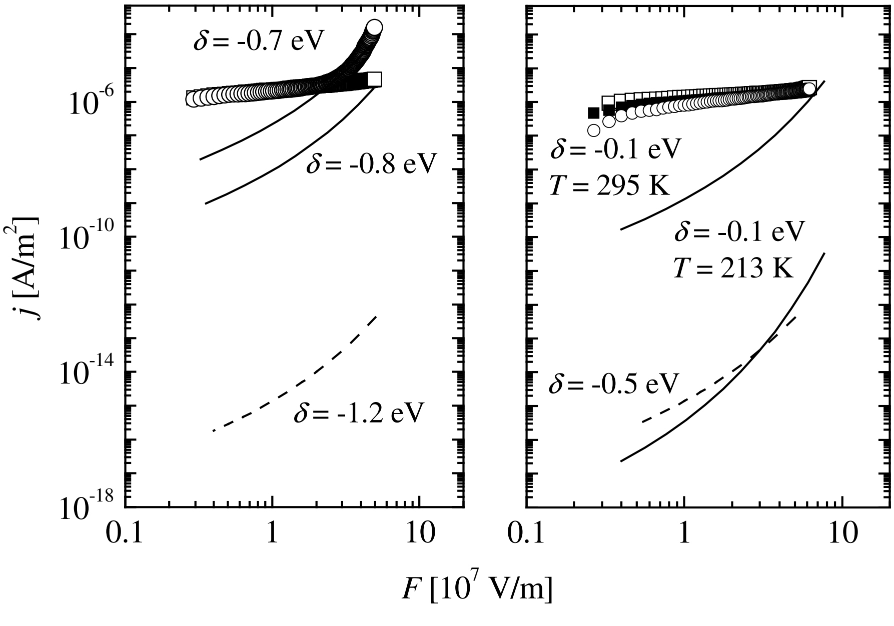

Figure 6.4 *Left*: IV-characteristics under reverse bias conditions of an Au/MEH-OPV5/Ag diode kept under UHV conditions (□) and for the same device polluted for 336 h at 1 bar in air (○). Holes were injected from the Au bottom contact into MEH-OPV5. The device thickness was 270 nm. *Right*: IV-characteristics under reverse bias conditions for an Ag/MEH-OPV5/Au diode at 295K (□), 213K (■), and 153K (○). Holes were injected from the Ag bottom contact into MEH-OPV5. The lines represent simulations of the hole injection current, using the injection model of Chapter 3 with the mobility data of *Chapter 4* and including vacuum-level shifts at the metal organic interfaces.

to vacuum-level shifts of –0.8 eV for a contact with Au and –0.1 eV for a contact with Ag. These estimates of the minimally required interfacial vacuum-level shifts are in accordance with the UPS results that indeed revealed stronger vacuum-level shifts. One should note, however, that an equally strong electron injection current cannot be excluded, since the electron injection barriers unveiled by UPS are comparable to the hole injection barriers.

An unambiguous proof whether the vacuum-level shifts at the metal/organic interfaces truly cause the low current densities still needs to be provided. It has been shown, however, that by exposing the metal/organic system to ambient atmosphere, the diffusion of environmental impurities through the organic material and their subsequent adsorption at the metal/organic interface result in an abatement of the vacuum-level shift [14]. This would lead to a decreased hole injection barrier at Au/MEH-OPV5 interfaces and, hence, to an increased charge injection current. Indeed, when exposing an Au/MEH-OPV5/Ag diode to air at 1 bar for 336 h, an increase of the current density for hole emission from Au became apparent (Fig. 6.4). The predicted vacuum-level shift changed from a value of below –0.8 eV to about –0.7 eV. The increase in current density upon pollution of the contacts may seem to be rather weak for a two-weeks exposure to air. It has been demonstrated, however, that the pollution of an only 8 nm thick layer of unsubstituted OPV5 deposited on Au merely results in a reduction of the interfacial vacuum-level shift from approximately –1 eV to –0.6 eV in as much as 75 h [14]. Since we typically prepared at least ten times thicker films, the diffusion process of the environmental impurities towards the organic/metal interface is expected to be slowed down. In addition, the metal top contacts effectively shielded the diode as the device diameter exceeded the typical device thickness by a factor >

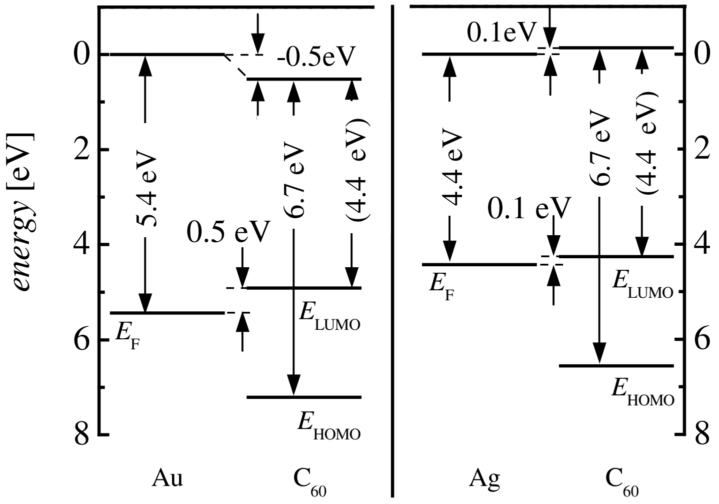

Figure 6.5: Energy diagram of a C_{60}/Au and a C_{60}/Ag contact obtained by UPS measurements [14, 17].

1000. The revealed vacuum-level shift of –0.7 eV for a polluted diode, consequently, seems to be amenable.

We can conclude that the strong interfacial vacuum-level shifts detected by UPS result in large electron and hole injection barriers, which basically prevent any measurable current through a diode. The disclosed IV–characteristics are, hence, in agreement with the energy diagrams revealed by UPS.

6.4 Diodes based on C_{60}

The energy diagrams of C_{60} deposited on polycrystalline Ag and Au are depicted in Fig. 6.5 as determined by UPS [14, 17]. While a vacuum-level shift of –0.5 eV was found at the C_{60}/Au interface, shifting E_{HOMO} of C_{60} downwards in energy compared to E_{F} of Au, a vacuum-level shift of +0.1 eV was unveiled at the C_{60}/Ag interface, which was earlier explained by a partial electron transfer from Ag to C_{60} [14, 17]. The Fermi-edge energy of Ag is close to E_{LUMO} of C_{60}, and the unoccupied states of C_{60} might be populated by excess charges of the metal. The resulting electric field causes a positive energy shift of C_{60} compared to Ag. The vacuum-level shift $\delta<0$ at the Au/C_{60} interface was previously identified as a back-donation process, where the formation of a hybrid bond between Au and C_{60} leads to a corresponding partial charging of the interfacial C_{60} [14, 17].

Since UPS is only sensitive for occupied states, the electron affinity of C_{60} is not directly accessible. E_{LUMO} can be, however, estimated by assuming the band gap of C_{60} (2.3 eV [18]) to be equal to the difference between its electron affinity and its ionization potential. The estimated electron injection barriers for Au and Ag/C_{60} contacts are listed in Table 6.2 and are clearly lower than the corresponding hole injection barriers. It is, therefore, most likely that the respective diodes are electron-only devices. Electron emission from the Au contact into C_{60} most probably results in an injection-limited current, since the electron injection barrier is rather large. In contrast, space-charge built-up and the concomitant screening of the electric field is the most plausible current limitation when electrons are injected from Ag, since the electron injection barrier at the Ag/C_{60} contact is only 0.1 eV. In the following, the IV–

Table 6.2 Electron injection barriers ϕ estimated by UPS [14, 17] and zero field activation energy E_{ac} of the current density for C_{60}-based diodes.

Interface :	Au/C_{60}	Ag/C_{60}
ϕ_{UPS} [eV]	0.5	0.1
$\phi_{\mathrm{UPS}}(\delta=0)$ [eV]	1.0	0.0
E_{ac} [eV]	0.58	0.49

characteristics of C_{60}-based diodes prepared and measured in UHV will be discussed with respect to their current limitations.

In Fig. 6.6, the IV–characteristics for electron emission from Ag and Au into C_{60} are depicted. In both cases, the current densities were temperature-activated and showed a stretched exponential field dependence of form $j_0(T)\times\exp[\gamma_j(T)\sqrt{F}]$ in a large field range rather than a power law dependence. Since the former is typical for injection limitation and the latter is expected for space-charge limitation, an injection mechanism is presumably the rate-limiting process. As apparent from Fig. 6.7, both the logarithmic of the zero field current density $j_0(T)$, and the field activation factor of the current density $\gamma_j(T)$ followed an Arrhenius type of temperature activation from 295 K down to 250 K. Interestingly, the temperature dependence of the field activation is sufficiently described by a Schottky lowering ($\gamma_j = q\beta_s/kT$, $\beta_s = \sqrt{q/4\pi\varepsilon_s}$) (Eq. 3.9) with a single dielectric constant of 4.09 ± 0.15, being close to the dielectric constant of C_{60} measured by others [19-21]. Here, ε_s is the permittivity of the semiconductor. This supports the hypothesis that charge carrier injection limits the current through the investigated diodes and suggests a thermionic emission type of injection process [1, 22]. Yet, for low-mobility media, the thermionic emission theory is hardly applicable [23], and the diffusion theory [1] or the model for emission-limited injection into a trap-free transport hopping system (*Chapter* 3) should in contrast be applied. However, it can be seen from Fig. 6.6 that the latter (as well as the diffusion theory) fails to

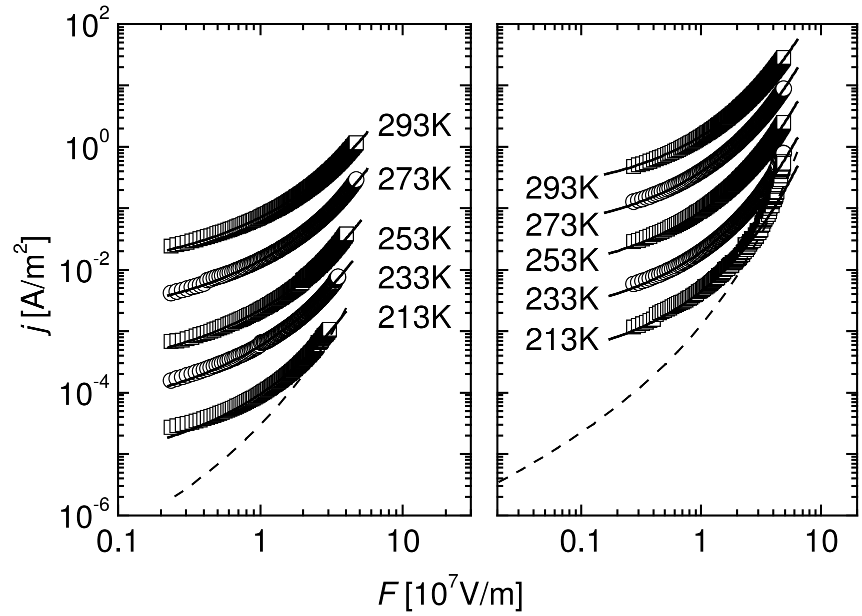

Figure 6.6 *Left*: IV-characteristics of an Au/C_{60}/Au device at various temperatures. Electrons were injected from the Au bottom contact into the semiconductor. *Right*: IV-characteristics of an Ag/C_{60}/Au device at various temperatures. Electrons were injected from the Ag bottom contact into the semiconductor. The layer thickness was 200 nm. The dashed lines represent fits using the injection model proposed in *Chapter 3*. Better fits could be obtained by using $j = j_0(T)\exp[\gamma_j(T)\sqrt{F}]$ (—).

describe the experimentally observed IV–characteristics in the low-field regime.

From the Arrhenius-type of temperature activation of the zero field current density j_0, we extracted the zero field activation energies E_{ac} for electron emission from Au and Ag, respectively, into C_{60} (Table 6.2). The unveiled zero field activation energy of 0.58 eV for electron emission from Au matched the electron injection barrier found by UPS, suggesting that the zero field activation energy is related to the charge injection barrier at the metal/organic interface, in accordance to an injection limitation of the current. On the other hand, we found that the zero field activation energy of the current density for charge carrier emission from Ag into C_{60} was higher than the electron injection barrier predicted by UPS, but was close to the zero field activation energy revealed for electron emission from Au. This indicates that E_{ac} is virtually independent from the used metal, questioning the hypothesis that exclusively the charge carrier injection barriers determine the activation energies of current densities.

In general, the activation energy of the conductance is given by the thermal activation of charge carriers (under injection limitation determined by the injection barriers) and the activation energy of the charge carrier mobility. This holds in particular for a diffusive injection mechanism. While for single-crystals almost

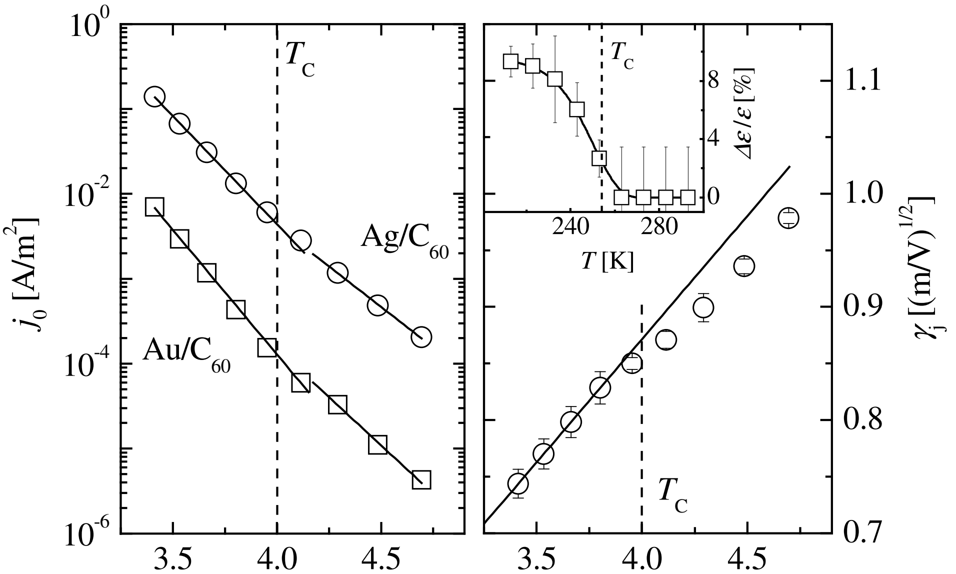

Figure 6.7 *Left*: Temperature dependence of the zero field current density j_0 for an Au/C_{60}/Au (□) and an Ag/C_{60}/Au (○) device under forward bias conditions (injection of electrons from the bottom contact), revealing zero field activation energies E_{ac} of 0.58 eV and 0.49 eV above T_c for electron emission from Au and Ag contacts, respectively. Below T_c, injection barriers of 0.45 eV and 0.38 eV were found. *Right*: Temperature dependence of the field activation factor γ_j averaged for Au/C_{60}/Au and Ag/C_{60}/Au devices biased in forward direction. Above T_c, a Schottky lowering (Eq. 3.9) with a single dielectric constant of 4.09 ± 0.15 sufficiently describes the field activation of the current. Below T_c, the field activation becomes weaker, comprehending an increase of the dielectric constant (insert).

temperature-independent charge carrier mobilities have been reported [24], the charge transport in polycrystalline or amorphous films of C_{60} is strongly temperature-dependent, since these systems are more disordered. As a consequence, the activation energy of the effective mobility increases up to 0.5 eV for amorphous films, depending on the purity of the material [25-27]. Since polycrystalline or amorphous films are typically obtained by evaporation techniques, a mobility activation of around 0.5 eV is most likely, matching the temperature activation of the conductivity reported here. This indicates that the temperature activation of the current density might rather originate from the charge carrier mobility than from the injection barriers and stresses the importance of C_{60} bulk properties for the injection process, as considered in the diffusion theory.

For temperatures below 250 K, the temperature dependencies of the zero field current density and the field activation deviated from the ideal Arrhenius dependence. The temperature activation at zero field was reduced by 0.1 eV and the field activation turned out to be weaker in the low-T regime. If a Schottky lowering is assumed to determine the field dependence of the current density (Fig. 6.7), the reduction of the field activation factor comprehends an increase of the dielectric constant. This behavior is probably a consequence of the first order phase transition that C_{60} performs at approximately $T_c = 250$ K [21, 28]. At room temperature, C_{60} forms a FCC crystal [29], in which each individual molecule is free to rotate around its lattice side [30], resulting in point symmetry in time average. Below T_c, however, four interpenetrating SC sublattices are formed with slightly changed lattice parameters [31]. In this low-temperature phase, each molecule acquires a net orientation along a specific crystallographic direction [29, 32]. It has been shown that as a result, the dielectric permittivity of C_{60} single-crystals abruptly increases by 3 % at T_c [21, 28]. The increase in the dielectric permittivity might weaken the Schottky effect and, hence, might reduce the field dependence of the injection current. Likewise, a dependence of the current density on the charge carrier mobility comprehends an increase in current densities below T_c. The FCC-SC phase transition results in an abrupt change in the lattice constant and, as a consequence, in an increased intermolecular interaction [31, 33, 34], which favors the charge transfer between adjacent molecules. Therefore, the charge carrier mobility and the conductivity in C_{60} change significantly at T_c [24, 28]. In single crystals of C_{60}, the charge carrier mobility exhibits a 60 % increase around the phase transition temperature, while elsewhere it is only slightly temperature-dependent. It was confirmed by conductivity and field effect measurements that even in polycrystalline or amorphous films the phase transition eventuates in improved charge transport properties of C_{60} below T_c [26, 27], which might cause the here-observed behavior of the current density at the phase transition.

The discussion in the last paragraphs leads to the conclusion that irrespective of the used electrode metals, the current densities are injection-limited. This is strongly supported by the fact that a simple Schottky lowering describes the field dependence of the current densities with one unique and reasonable dielectric constant for C_{60}. While the zero field activation energy for electron emission from Au equaled the electron injection barrier found by UPS, the one for electron emission from Ag was not reproduced. Since the unveiled zero field activation energies were comparable to the typical activation energy of the charge carrier mobility, almost independent of the employed electrode metals, and their changes were similarly strong when undergoing T_c, a temperature activation associated to the charge carrier mobility cannot be excluded. However, as no space-charge-limited current was observed in the investigated diodes, injection barriers - even for the Ag/C_{60} contact – must be high enough to prevent space-charge built-up.

6.5 Conclusion

In this chapter we compared conductivity measurements of thin-film organic diodes with their respective energy diagrams. Strong interactions between MEH-OPV5 and Ag or Au resulted in high hole and electron injection barriers, which in thin-film diodes led to current densities even below our detection limit. In contrast, C_{60} formed moderate electron injection barriers with Ag or Au, which permitted substantial electron injection currents. The FCC-SC phase transition of C_{60} arising at $T_c \sim 250$ K was reflected in the IV–characteristics.

The fact that vacuum-level shifts at the metal/organic interfaces have a significant impact on the device operation opens a new means for device engineering. For instance, compounds that introduce artificial vacuum-level shifts at the metal/organic interface such as self-assembled mono-layers may strategically be employed to tailor the properties of a given device. The two discussed systems illustrate the potency of interfacial interactions for an efficient tuning of thin-film diodes for specific applications.

References

[1] S. M. Sze, *Physics of Semiconductor Devices*, Wiley & Sons Inc., New York (1981).

[2] K. C. Kao and W. Hwang, *Electrical transport in solids with particular reference to organic semiconductors*, Pergamon Press, Oxford (1981).

[3] S. C. Jain, A. K. Kapoor, W. Geens, J. Poortsmans and R. Mertens, J. Appl. Phys. **92**, 3752 (2002).

[4] P. W. M. Blom and M. C. J. M. Vissenberg, Mater. Sci. Eng. **27**, 53 (2000).

[5] H. Ishii, K. Sugiyama, E. Ito and K. Seki, Adv. Mater. **11**, 605 (1999).

[6] W. R. Salaneck, M. Lögdlund, M. Fahlman, G. Greczynski and T. Kugler, Mater. Sci. Eng. R **34**, 121 (2001).

[7] G. Greczynski, T. Kugler and W. R. Salaneck, J. Appl. Phys. **88**, 7187 (2000).

[8] A. J. Mäkinen, I. G. Hill, R. Shashidhar, N. Nikolov and Z. H. Kafafi, Appl. Phys. Lett. **79**, 557 (2001).

[9] H. Peisert, M. Knupfer and J. Fink, Appl. Phys. Lett. **81**, 2400 (2002).

[10] H. Peisert, M. Knupfer, T. Schwieger, J. M. Auerhammer, M. S. Golden and J. Fink, J. Appl. Phys. **91**, 4872 (2002).

[11] N. Koch, A. Kahn, J. Ghijsen, J.-J. Pireaux, J. Schwartz, R. L. Johnson and A. Elschner, Appl. Phys. Lett. **82**, 70 (2003).

[12] T. Koopmans, Physica **1**, 104 (1934).

[13] S. C. Veenstra, U. Stalmach, V. V. Krasnikov, G. Hadziioannou, H. T. Jonkman, A. Heeres and G. A. Sawatzky, Appl. Phys. Lett. **76**, 2253 (2000).

[14] *Thesis:* S. C. Veenstra, *Electronic Structure of Molecular Systems. From Gas Phase to Thin Films to Devices*, Polymer Chemistry Rijksuniversiteit Groningen, Groningen (2002).

[15] Y. Park, V. Choong, E. Ettedgui, Y. Gao, B. R. Hsieh, T. Wehrmeister and K. Müllen, Appl. Phys. Lett. **69**, 1080 (1996).

[16] Y. Park, V. Choong, B. R. Hsieh, C. W. Tang, T. Wehrmeister, K. Müllen and Y. Gao, J. Vac. Sci. Technol. A **15**, 2574 (1997).

[17] S. C. Veenstra, A. Heeres, G. Hadziioannou, G. A. Sawatzky and H. T. Jonkman, Appl. Phys. A: Mater. Sci. Proc. **75**, 661 (2002).

[18] R. W. Lof, M. A. van Veendaal, B. Koopmans, H. T. Jonkman and G. A. Sawatzky, Phys. Rev. Lett. **68**, 3924 (1992).

[19] S. L. Ren, Y. Wang, A. M. Rao, E. Mc Rae, J. M. Holden, T. Hager, K. Wang, W. T. Lee, H. F. N. J. Selegue and P. C. Eklund, Appl. Phys. Lett. **59**, 2678 (1991).

[20] B. Pevzner, A. F. Hebard, R. C. Haddon, S. D. Senturia and M. S. Dresselhaus, *Science and Technology of Fullerene Materials*, Materials Research Society, Pittsburgh (1995).

[21] A. Fartash, Physical Review B **54**, 17215 (1996).

[22] H. A. Bethe, MIT Radiat. Lab. Rep. **43**, 12 (1942).

[23] J. G. Simmons, Phys. Rev. Lett. **15**, 967 (1965).

[24] E. Frankevich, Y. Maruyama and H. Ogata, Chem. Phys. Chem. **214**, 39 (1993).

[25] K. Kaneto, K. Yamanaka, K. Rikitake, T. Akiyama and W. Takashima, Jpn. J. Appl. Phys. **35**, 1802 (1996).

[26] C. P. Jarret, K. Pichler, R. Newbould and R. H. Friend, Synth. Met. **77**, 35 (1996).

[27] K. Kaneto, K. Rikitake, T. Akiyama and H. Hasegawa, Jpn. J. Appl. Phys. **36**, 910 (1997).

[28] G. B. Alers, B. Golding, A. R. Kortan, R. C. Haddon and F. A. Theil, Science **257**, 511 (1992).

[29] P. A. Heiney et al., Phys. Rev. Lett. **66**, 2911 (1991).

[30] R. D. Johnson, C. S. Yannoni, H. C. Dorn, J. R. Salem and D. S. Bethune, Science **255**, 1235 (1992).

[31] E. A. Katz, D. Faiman, S. Shtutina and A. Isakina, Thin Solid Films **368**, 49 (2000).

[32] W. I. F. David et al., Nature **353**, 147 (1991).

[33] W. I. F. David, R. M. Ibberson, T. J. S. Dennis, J. P. Hare and K. Prassides, Europhys. Lett. **18**, 735 (1992).

[34] P. A. Heiney, G. B. M. Vaughan, J. E. Fischer, N. Coustel, D. E. Cox, J. R. D. Copley, D. A. Neumann, W. A. Kamitakahara, K. M. Creegan, D. M. Cox, J. P. Mc Cauley and A. B. Smith, Phys. Rev. B. **45**, 4544 (1992).

7

Organic donor/acceptor photovoltaics

Abstract

In this chapter, the influence of the film organization of the donor/acceptor system on the cell performance of organic photovoltaic cells is discussed with a focus on characteristic parameters, such as the open circuit voltage (U_{oc}) and the photovoltaic sensitivity. At first, the photovoltaic properties of double-layer cells with one single planar heterojunction are compared with those of cells based on a blend of the same donor and acceptor materials, containing a spatially distributed heterojunction interface. In particular, we emphasize the impact of interface effects on U_{oc} and suggest a simple dilution model, which provides a link between the film morphology and U_{oc}. The influence of the film morphology on the susceptible volume fraction for efficient exciton dissociation is discussed. Secondly, we report on the action spectra of double-layer cells, which provide information on the exciton diffusion length of the employed materials. Finally, results on the morphology of thin films based on a donor/acceptor diblock copolymer are presented. The revealed film organization is compared to the photoresponse of corresponding photovoltaic cells.

7.1 Introduction

In the last decade, the potential of organic materials in the field of electronics triggered novel interest in material sciences, chemistry and physics. While organic light-emitting diodes are already commercially available, efficiencies of organic solar cells do not yet fulfill the industrial demands [1-6]. This requires an intensive search for more efficient organic materials suitable for photovoltaic applications, and a better understanding of the cell physics.

The photovoltaic effect involves the creation of electrons and holes under optical excitation and their successive collection at opposite electrodes. Upon excitation of organic semiconductors by light, neutral electron/hole pairs are created, called excitons [7]. The mobile excitons, having a lifetime in the sub-nanosecond range [8, 9], diffuse through the organic medium until they relax and the photogenerated charges get lost for the photovoltaic effect. In order to make electrons and holes available for the external circuit, excitons have to dissociate. Dissociation efficiently occurs at the interface of two materials with different ionization potentials and electron affinities, leading to the common use of donor/acceptor-type photovoltaic systems [1, 2, 10]. The energy of an optically excited donor electron is lowered by its ultra-fast transfer (sub-picosecond range) to the lowest unoccupied molecular orbital (LUMO) of the acceptor. This reversible metastable electron transfer results in electrons and holes that are susceptible for further transport. By using metal electrodes with different workfunctions (φ), a built-in field is created, leading to an electron current along the acceptor phase towards the low-workfunction metal and a hole current along the donor phase towards the high-workfunction electrode.

The quality of photovoltaic cells is reflected by a number of characteristics that can be obtained by current-voltage (IV) measurements performed under illumination. At zero bias, the photovoltaic performance is characterized by the photovoltaic sensitivity (S), which is the photocurrent density (short circuit condition) divided by the light intensity. The open circuit voltage (U_{oc}) is the required bias, at which no current is measured under illumination: the dark current and the photocurrent are equal in amplitude, but proceed in opposite directions. Usually, U_{oc} is close to the built-in potential (U_{bi}). The diode quality is characterized by the fill factor (FF), which is the maximal electrical power over the product of U_{oc} and the short circuit current. Finally, the external power conversion efficiency (η) of the photovoltaic cell is defined as the electrical output power divided by the input power of the light. Hence, η is equal to the product of S, FF, and U_{oc}. The definitions of the photovoltaic characteristics are listed in Table. 7.1.

Currently, two basic donor/acceptor cell structures are mainly discussed displaying contrary advantages and drawbacks. Double-layer cell structures with a single planar heterojunction interface show good diode behavior, but the limited exciton dissociation interface causes a rather low sensitivity [3, 11, 12]. In this respect, a percolated system of donor and acceptor phases, i.e. a network of heterojunctions through the entire film, seems to be more promising [1, 2, 5]. In turn, however, charge carrier transport in this second device structure might be less efficient due to the intermixing of two different materials. Consequently, internal losses of photogenerated charge carriers might become more essential, which would eventually restrict the photovoltaic response of a percolated photovoltaic cell. It is thus not evident whether a photovoltaic system based on a blend of donor and acceptor materials is superior if compared to a double-layer system of the same compounds. Since the morphology of the active layer in an organic donor/acceptor photovoltaic cell is obviously of crucial importance for an efficient cell performance, it is subject of this chapter.

7.2 Photovoltaic performance and morphology

In this section, the impact of the morphology of the donor/acceptor system on the overall photovoltaic cell performance is discussed. As photovoltaic model systems, we compared the two extreme structures of a strict double-layer and a random blend organization of donor and acceptor materials. For both film structures, the same materials and identical preparation procedures were employed, in order to address exclusively the impact of the morphology on the cell performance. As the anode, we used indium tin oxide (ITO) covered with a thin layer of poly(3,4-ethylene dioxythiophene) that was highly doped with poly(styrene sulfonic acid) (PEDOT:PSS), while aluminum (Al) was employed as the cathode. Pre-patterned ITO-coated glass substrates were wet cleaned and a thin layer (~80 nm) of PEDOT:PSS (Bytron P) was deposited by spin-coating. The layer was dried under high vacuum at elevated temperature. Double-layer cells were prepared by consecutive thermal vacuum deposition of the donor (*E*,*E*,*E*,*E*)-1,4-bis[(4-styryl)styryl]-2-methoxy-5-(2'-ethyl-hexyloxy)benzene (MEH-OPV5) and the acceptor Buckminster fullerene (C_{60}), while bulk heterojunction photovoltaic cells were obtained by the co-deposition of both

Characteristic	Definition
Short circuit current	$I \equiv I_{\mathrm{sc}}$ for $U = 0$
Open circuit voltage	$U \equiv U_{\mathrm{oc}}$ for $I = 0$
Photovoltaic sensitivity	$S \equiv \frac{I_{\mathrm{sc}}}{P_{\mathrm{L}}}$
Fill factor	$FF \equiv \frac{(I \times U)_{\max}}{I_{\mathrm{sc}} U_{\mathrm{oc}}}$
External power conversion efficiency	$\eta \equiv \frac{(I \times U)_{\max}}{P_{\mathrm{L}}} = S \cdot FF \cdot U_{\mathrm{oc}}$

Table 7.1 Photovoltaic characteristics of cells under illumination. I, U and P_{L} are the current, the applied voltage, and the light power, respectively.

moieties in a 1:1 ratio (1 Å/s at 10^{-6} mbar). The substrate temperature was equal to room temperature during deposition. Subsequently, Al was vacuum-deposited at 10^{-6} mbar on the obtained structures. All measurements were performed in an inert environment.

In Fig. 7.1, the IV–curves of an ITO/PEDOT:PSS/MEH-OPV5/C_{60}/Al double-layer cell in the dark and under illumination are presented. The cell showed an S of around 0.054 A/W and a high FF of 0.45. With U_{oc} = 0.88 V, this resulted in a monochromatic η of ~ 2 % (illuminated at 458 nm with 1mW/cm^2). S was constant over a broad range of light intensity (P_L), and U_{oc} saturated to almost 1 V at a P_L of approximately 10 mW/cm^2 (Fig. 7.2). A saturated open circuit voltage (U_{soc}) of 0.9 ±0.1 V was found as the average of several samples.

S of an ITO/PEDOT:PSS/MEH-OPV5+C_{60}/Al co-deposited cell was measured to be 0.078 A/W (Fig. 7.1, λ = 458 nm, P_L = 1 mW/cm^2). At low P_L (< 0.1 mW/cm^2), S was about 0.1 A/W, which is twice higher than for double-layer cells, and decreased with an increase in P_L. The FF of the co-deposited cell was determined to be only 0.25, and U_{oc} was found to be 0.65 V. U_{oc} saturated to 0.7 ±0.1 V at high P_L, averaged over several samples.

In Table 7.2, the photovoltaic parameters obtained for consecutively and co-deposited cells are summarized [13]. It is apparent that the higher photovoltaic sensitivity of co-deposited cells is negatively compensated by their lower FF and U_{oc}. This results in a monochromatic external power conversion efficiency of 1 % that is,

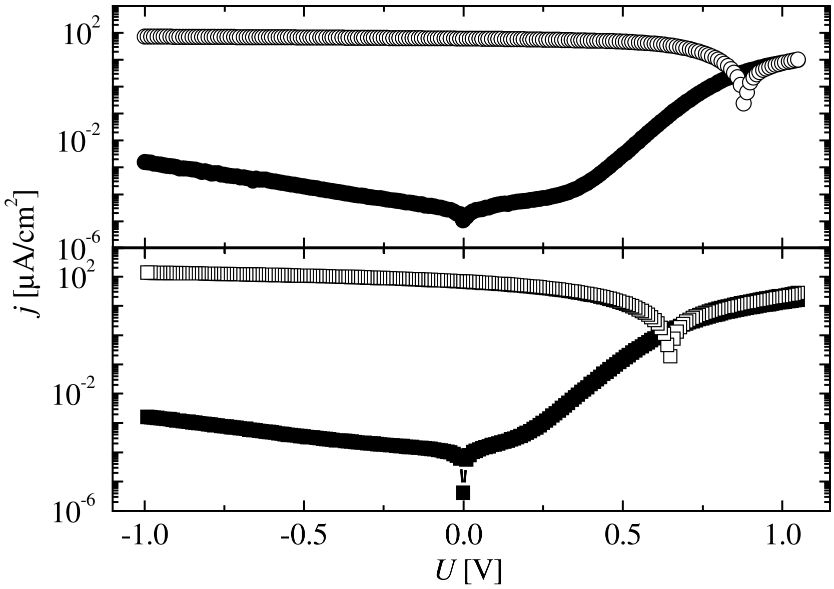

Figure 7.1 IV–characteristics of double-layer ITO/PEDOT:PSS/MEH-OPV5/C_{60}/Al (top) and of co-deposited ITO/PEDOT:PSS/MEH-OPV5 + C_{60}/Al cells (bottom) in the dark (filled symbols) and under illumination (open symbols) with 1 mW/cm^2 at 458 nm. The total layer thickness was around 100 nm in both cases.

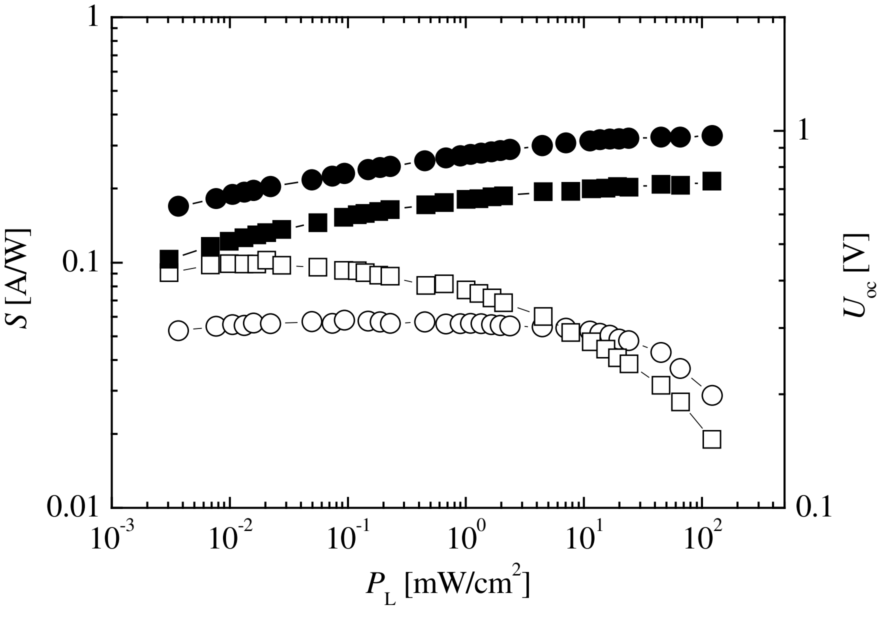

Figure 7.2 Photovoltaic sensitivity (open symbols) and open circuit voltage (filled symbols) versus the light intensity for the consecutively (circles) and co-deposited cells (squares) of Fig. 7.1.

	S [A/W]	FF	U_{oc} [V]	η [%]	U_{soc} [V]	δU_{bi} [eV]	N_i [10^{16} cm^{-3}]	W_{0V} [nm]
Double-layer	0.054	0.45	0.88	2.1	0.9 ±0.1	0.0 ±0.1	–	–
Blend	0.078	0.25	0.65	1.3	0.7 ±0.1	-0.2 ±0.1	0.5 ±0.1	240 ±7
Single-layer MEH-OPV5	–	–	–	–	1.1 ±0.1	0.2 ±0.1	–	–
Single-layer C_{60}	–	–	–	–	0.3 ±0.2	-0.6 ±0.2	1.1 ±0.4	110 ±20

Table 7.2 Main cell characteristics for double-layer ITO/PEDOT:PSS/MEH-OPV5/C_{60}/Al cells, co-deposited ITO/PEDOT:PSS/MEH-OPV5 + C_{60}/Al cells, single-layer MEH-OPV5, and C_{60} cells. The total thickness of the semiconducting layers was ~100 nm. S is the photovoltaic sensitivity and FF is the fill factor measured with 1 mW/cm^2 light intensity at an illumination wavelength of 458 nm. U_{soc} is the saturated open circuit voltage at the same wavelength, and δU_{bi} is the effective change in U_{bi} due to vacuum-level shifts. The built-in potential U_{bi} was found to be equal to U_{soc}. N_i and W_{0V} are the ionized state density and the depletion width at zero bias, respectively.

surprisingly, two times lower than the one of double-layer cells (2%), even though the exciton dissociation efficiency in a co-deposited cell is supposed to be significantly higher due to the larger heterojunction interface. Others have reported similar observations for cells employing indium tin oxide as the anode material [14]. To understand the observed difference in the monochromatic external power conversion efficiency in more detail, one has to trace back the origin of the disparities in *FF*, *S* and U_{oc}.

7.2.1 Fill factor

The lower monochromatic η of photovoltaic cells based on co-deposited films is partly related to their lower *FF*. For efficient charge carrier read-out, both the donor and the acceptor phases are required to form a continuous network to allow bipolar charge transport. However, in the case of spatially distributed donor/acceptor heterojunctions, partial discontinuities in the donor and/or acceptor phases can occur. Furthermore, an increased energy level disorder in both phases due to strong intermixing of donor and acceptor materials may result in an increase of the charge carrier trap densities and, therefore, in a reduction of the electron and/or hole transport properties. Intuitively, it seems possible that this scenario holds true in the here-investigated bulk heterojunction photovoltaic cells, where the phase separation of the donor and the acceptor material is not optimized. If, as a consequence, the charge carrier transit times exceeded the lifetime of the charge carriers, charge carrier recombination and, hence, internal losses would be significant [15, 16], typically leading to a low *FF*. Moreover, space-charge built-up could determine the photoresponse of the cell, namely if blending resulted in strongly unbalanced charge carrier transport properties, favoring accumulation of the slower charge carrier species in the film. The resulting screening of the electric field dramatically affects the *FF* [15, 17]. In contrast to random blends, the *FF* of consecutively deposited cells was found to be higher, which demonstrates the superior transport properties of double-layer systems. However, the fill factors in MEH-OPV5/C_{60} blends may still be improved by tuning the film morphology as reported for other organic bulk heterojunction photovoltaic cells, in which an optimal phase separation allowed fill factors as high as 0.6 [5].

7.2.2 Photovoltaic sensitivity

In general, excitations created in the donor material within the exciton diffusion length from the heterojunction interface are susceptible for efficient exciton dissociation. Since the exciton diffusion length is typically shorter than the light absorption depth, a percolation of donor/acceptor heterojunctions is more efficient in terms of exciton dissociation than a conventional double-layer structure with a single planar donor/acceptor heterojunction. Very efficient photovoltaic cells using this kind of bulk heterojunction systems have been produced, shifting the performance of organic photovoltaic cell towards the one of their inorganic counterparts [5, 18].

Surprisingly, however, the saturated *S* of a co-deposited cell based on MEH-OPV5 and C_{60} was only two times higher than the one of a consecutively deposited cell (Fig. 7.2). This observation is in agreement with the findings of others, employing the same donor and acceptor materials, but a different anode [14].

In section 7.3, it will be demonstrated that the exciton diffusion length in MEH-OPV5 is in the 20 nm range, which makes a rather large volume fraction of the donor material in a consecutively deposited cell susceptible for exciton dissociation. However, from the results of section 7.3 and considering the architecture of the here-presented cells, it can be estimated that the photovoltaic sensitivity of a perfect bulk heterojunction cell should still exceed the one of a truly planar double-layer cell by one order of magnitude. To gain more insight into the relatively small increase in *S* upon changing the morphology from a double-layer to a percolated system, we therefore studied the topography of vacuum-deposited MEH-OPV5 on ITO/PEDOT:PSS substrates by atomic force microscopy (AFM) (Fig. 7.3). For comparison, the surface topographies of ITO and ITO/PEDOT:PSS were measured. While the ITO-coated substrate and the spin-coated PEDOT:PSS showed a rather smooth topography, the thermal vacuum deposition of MEH-OPV5 resulted in the formation of islands with an maximal height of about 40 nm and lateral extensions of around 200 nm. As a consequence, the area of the heterojunction interface of a consecutively deposited cell is larger than the one of an ideal double-layer cell, thereby approaching the area of a percolated system in terms of availability for exciton dissociation. Similar observations

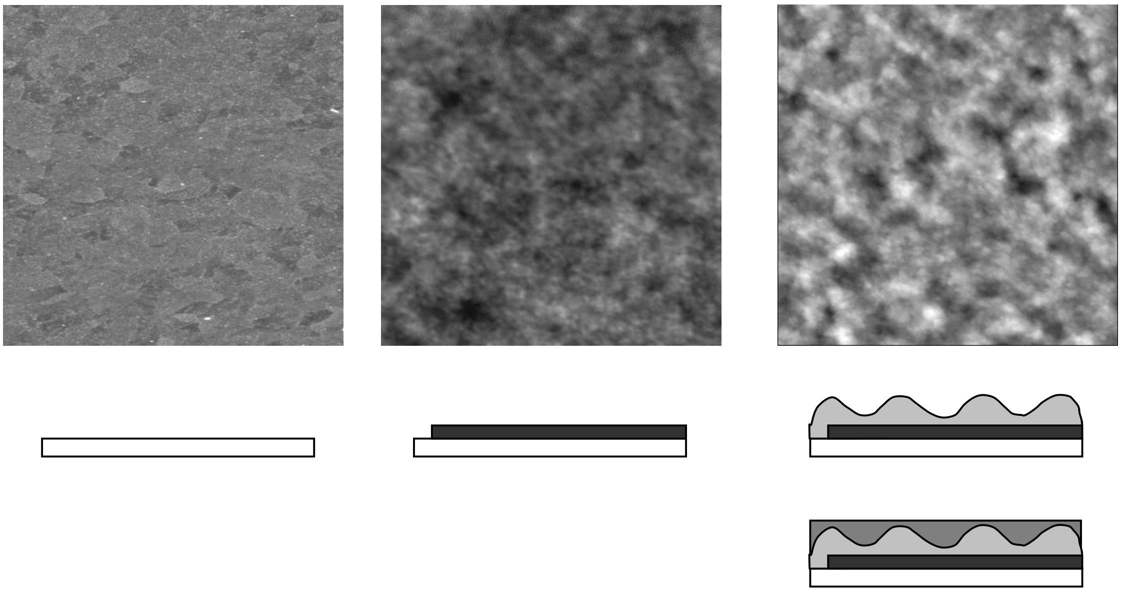

Figure 7.3 Topography of the ITO-coated glass substrate (left), spin-coated PEDOT:PSS on the ITO substrate (middle), and thermal vacuum-deposited MEH-OPV5 on PEDOT:PSS (right). All pictures are 2×2 μm. Maximal heights are from left to right: 20 nm, 15 nm, and 50 nm. Sketches below the pictures indicate the structure of the measured cells.

were reported by Ouali *et al.* [14], who studied the surface topography of vacuum-deposited MEH-OPV5 on mica. Likewise, they found that the consecutively deposited cell has an intermediate morphology between a blend and a truly planar double-layer film, exhibiting a finger-shaped interpenetrating pattern as indicated by the sketch in Fig. 7.3. Yet, the island formation of MEH-OPV5 deposited on PEDOT:PSS translates in a relative increase of the heterojunction interface of only 5 %, which cannot be exclusively responsible for the comparable photovoltaic sensitivities. In order to increase the heterojunction interface substantially, the average height of the topographic features needs to be close to the cell thickness d (~ 100 nm) and, concomitantly, their diameter is required to be much smaller than 200 nm, preferably in the range of the exciton diffusion length. Besides the increased heterojunction interface in a consecutively deposited cell due to roughness effects, a sub-optimal phase separation in the blend is even more likely to cause the similar exciton dissociation efficiencies, leading to the unveiled weak disparity in S.

7.2.3 Open circuit voltage

From Fig. 7.2 it can be seen that the U_{soc} of a double-layer cell came close to 0.9 V, while the one of a co-deposited cell was measured to be only 0.7 V. This difference in U_{soc} contributes to the disparity in the monochromatic η of consecutively and co-deposited cells. We also investigated the photovoltaic performance of single-layer MEH-OPV5 and C_{60} cells, respectively. The IV–characteristics in the dark and under illumination can be seen in Fig. 7.4. While the U_{soc} of a single-layer MEH-OPV5

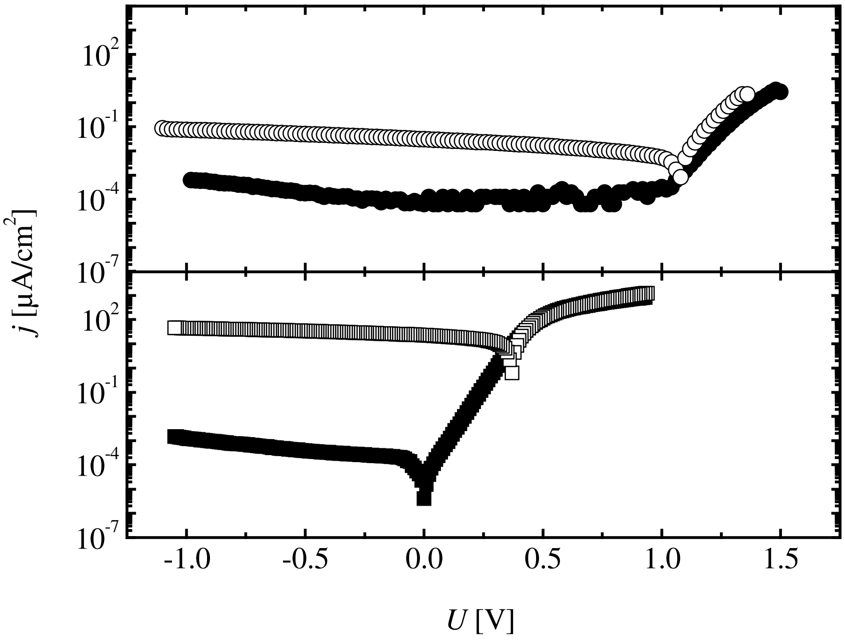

Figure 7.4 IV-characteristics of an ITO/PEDOT:PSS/MEH-OPV5/Al single-layer cell in the dark (●) and under illumination (○), and of an ITO/PEDOT:PSS/C_{60}/Al single-layer cell in the dark (■) and under illumination (□) with 1 mW/cm^2 at 458 nm.

cell approached 1.1 ±0.1 V (Table 2), the U_{soc} of a single-layer C_{60} cell was found to be only 0.3 ±0.2 V.

7.2.3.1 Built-in potential

Capacitance-voltage (CV) measurements on single-layer C_{60}, single-layer MEH-OPV5, double-layer and co-deposited cells revealed a bias-independent geometrical capacitance C_g at high frequencies (> 1 kHz). However, at low frequencies (< 100 Hz), a steep increase of the capacitance C in forward bias was observed for single-layer C_{60} and co-deposited cells (Fig. 7.5), while the capacitance of single-layer MEH-OPV5 and double-layer cells was hardly affected upon a change in bias.

Several models including Schottky contact, p-n junction, charging of surface states etc. predict such bias-dependent capacitance with slow dynamics. In the low frequency regime, a linear dependence of $1/C^2$ on bias reveals a depletion capacitance and simultaneously provides its built-in potential (U_{bi}), ionized state density (N_{i}), and the depletion width (W, e.g. at zero bias: $W_{0\mathrm{V}}$):

Eq. 7.1
$$\frac{1}{C^2} = \left(\frac{W}{\varepsilon_s}\right)^2 = \frac{2}{q\varepsilon_s N_i}\left(U_{\mathrm{bi}} - U\right)$$

where q is the electron charge, U is the applied voltage and ε_s is the semiconductor permittivity [19]. Similar to the photovoltaic measurements, the CV-measurements

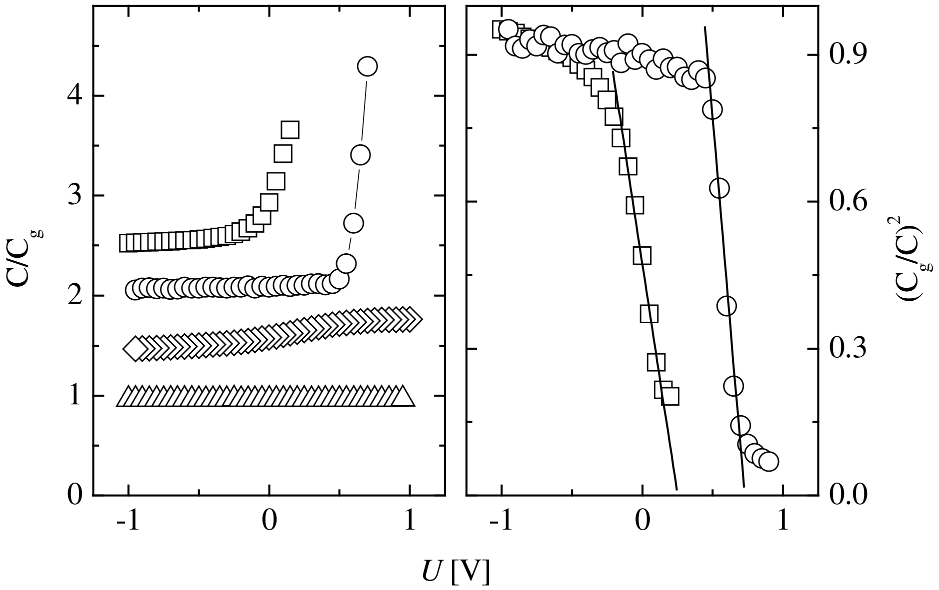

Figure 7.5 *Left*: Capacitance-voltage relation of a C_{60} single-layer cell (□), an MEH-OPV5 single-layer cell (Δ), a double-layer cell (◊), and a co-deposited cell (○) normalized on the geometrical capacitance C_g. Curves are shifted for clarity. *Right*: $(C_g/C)^2$ versus applied voltage of a single-layer C_{60} and a co-deposited cell.

showed strong deviations of U_{bi} from sample to sample and, consequently, also of W_{0V} and N_i. For each cell, however, the obtained U_{bi} was close to the measured U_{soc}. For single-layer C_{60} cells, $1/C^2$ versus U unveiled a depletion capacitance region only in a narrow range of forward bias when very thin layers of C_{60} were employed. At reverse bias, in contrast, the capacitance approached the geometrical capacitance (Fig. 7.5, Fig. 7.6). An increase in film thickness of C_{60} extended the depletion capacitance region towards reverse bias, corroborating a transition from a partly to a fully depleted cell (Fig. 7.6) and suggesting a one-side abrupt p-n heterojunction-type contact between C_{60} and one of the electrodes. Since a constant capacitance was observed over a wide range of bias and frequency for double-layer cells, the depletion layer was presumably formed at the anode/C_{60} contact. The energy diagrams of a partly and a fully depleted single-layer C_{60} cell are depicted in Fig. 7.6. We infer that the C_{60} layer is most likely n-doped with a rather low doping density of 10^{16} cm^{-3}. Although the origin of the doping is not known, Hayashi *et al.* demonstrated the formation of a Schottky barrier at C_{60}/metal interfaces by imaging the band bending with the Kelvin probe technique [20] and suggested a doping of C_{60} by intrinsic impurities.

Analogous to the observations in single-layer C_{60} cells, $1/C^2$ versus U in the low frequency regime of co-deposited cells showed a linear behavior in a narrow voltage range in forward bias, unveiling a depletion capacitance. The capacitance saturated to the geometrical capacitance in weak forward bias, which can be attributed to a transition from a partly to a fully depleted cell. Similar to single-layer C_{60} cells, the

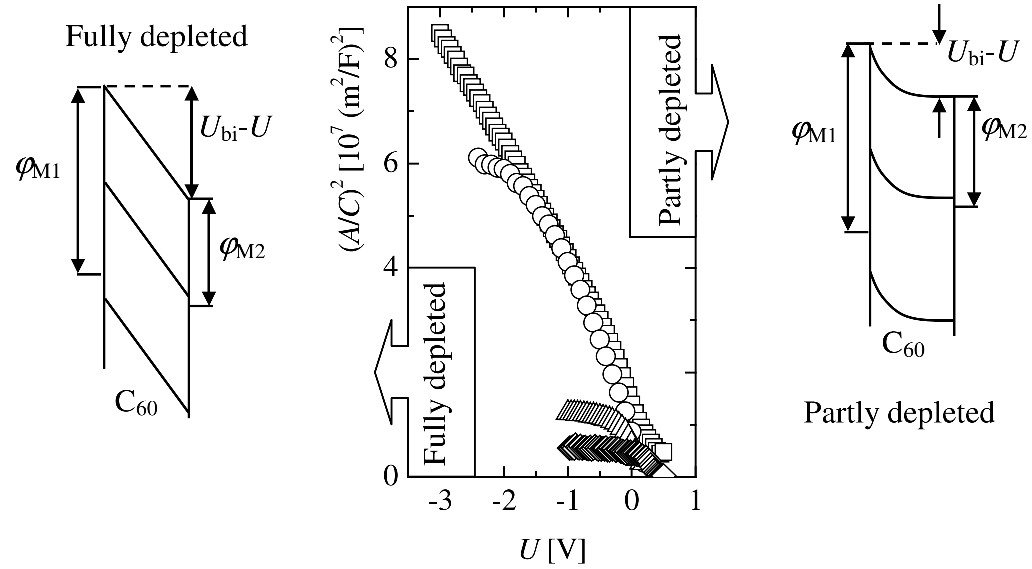

Figure 7.6 $(A/C)^2$ versus applied voltage for ITO/PEDOT:PSS/C_{60}/Al single-layer devices of 100 nm (◊), 130 nm (△), 300 nm (○), and 500 nm (□) thickness. A is the device area. The energy diagrams for fully and partly depleted conditions can be seen at the left and at the right side, respectively.

unveiled U_{bi} was always close to U_{soc}.

In conclusion, one-side abrupt p-n junctions were found to be present in single-layer C_{60} and co-deposited cells because of the use of slightly doped C_{60}. In turn, single-layer cells of MEH-OPV5 can be regarded to be fully depleted, since no depletion capacitance was observed. Moreover, it became apparent that for single-layer C_{60} and blended cells U_{bi} is a good approximation of U_{soc}.

7.2.3.2 Open circuit voltage and film structure

The major cell characteristics of the examined photovoltaic systems can be seen in Table 7.2. Assuming the metal-insulator-metal (MIM) model and typical workfunctions (φ) of PEDOT:PSS (5.2 eV) and Al (4.3 eV), the predicted U_{soc} for all cell-types should be about 0.9 V. We rationalize the lower U_{soc} found for single-layer C_{60} cells on basis of results obtained by ultraviolet photoelectron spectroscopy (UPS) that revealed strong vacuum-level shifts at metal/C_{60} interfaces (*Chapter 6*) [21], resulting in a low U_{bi}. Since the electron affinity of C_{60} (~ 4.4 eV) is approximately 0.1 eV below φ of Al, an electron transfer from Al to C_{60} is likely, pinning the LUMO of C_{60} to the Fermi-level of Al (δ_{AC} ~ 0.1 eV). Thus, a vacuum-level shift at the PEDOT:PSS/C_{60} interface (δ_{PC}) of about -0.5 eV would explain an U_{soc} of 0.3 V.

Similarly strong vacuum-level shifts were observed at metal/MEH-OPV5 contacts (*Chapter 6*) [22], which resulted in an U_{bi} of almost zero eV for Au/MEH-OPV5/Ag cells. The fact, however, that a single-layer ITO/PEDOT:PSS/MEH-OPV5/Al cell displayed an U_{soc} of 1.1 V (Table 7.2) shows that the formation of vacuum-level shifts at MEH-OPV5/electrode interfaces is strongly suppressed in terms of a reduction in U_{bi}. From *Chapter 4*, we know that the hole injection barrier at PEDOT:PSS/MEH-OPV5 contacts is approximately 0.4 eV. With an ionization potential of 5.3 eV for MEH-OPV5 (*Chapter 6*), a vacuum-level shift (δ_{PM}) of -0.3 eV is, hence, expected at the MEH-OPV5/PEDOT:PSS contact. Since we found $U_{\mathrm{soc}} = 1.1$ V for single-layer MEH-OPV5 cells, a vacuum-level shift (δ_{AM}) of -0.5 eV must occur at Al/MEH-OPV5 contacts.

In a double-layer cell, an additional interface occurs, namely the donor/acceptor interface, and significant vacuum-level shifts (δ_{het}) at this heterojunction were previously unveiled [23]. Indeed, in order to obtain the U_{soc} of 0.9 V found for consecutively deposited cells (Table 7.2), a vacuum-level shift of 0.4 eV should exist at the heterojunction interface of C_{60} and MEH-OPV5. Yet, this is rather large if compared to vacuum-level shifts of 0.25 eV found at e.g. OPV5/C_{60} interfaces [23]. However, in a double-layer cell under illumination the accumulation of photoinduced charge carriers generated close to the planar heterojunction interface gives rise to a diffusion current that must be counterbalanced by a drift current at open circuit in order to yield zero current [24, 25]. The drift current requires an additional electric field, which is provided by an external voltage beyond the flat band condition. It has been shown that the open circuit voltage of double-layer cells might, therefore, even exceed the predictions of the MIM model by more than 1 V [24].

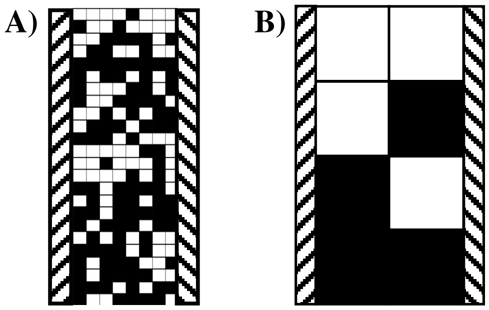

$$\delta U_{\text{bi}}^{1} = \delta_{\text{PM}} - \delta_{\text{AM}}$$

$$\delta U_{\text{bi}}^{2} = \delta_{\text{PM}} - \delta_{\text{AC}} + \delta_{\text{het}}$$

$$\delta U_{\text{bi}}^{3} = \delta_{\text{PC}} - \delta_{\text{AM}} - \delta_{\text{het}}$$

$$\delta U_{\text{bi}}^{4} = \delta_{\text{PC}} - \delta_{\text{AC}}$$

$$\left\langle \delta U_{\text{bi}}^{\text{blend}} \right\rangle = \tfrac{1}{2}\left(\delta_{\text{C}} + \delta_{\text{M}}\right)$$

Figure 7.7 Raster representation of a random blend of C_{60} (■) and MEH-OPV5 (□) sandwiched between PEDOT:PSS and Al (A). For an equally distributed blend, where both moieties and all patterns appear with the same probability, the system can be described by four general situations (B). $\left\langle \delta U_{\text{bi}}^{\text{blend}} \right\rangle$ is the spatially averaged change in U_{bi} that finally results from the vacuum-level shifts δ_{C} at the C_{60}/metal contacts and the vacuum-level shifts δ_{M} at the MEH-OPV5/metal contacts.

Our interpretation of the performance of co-deposited cells is mainly based on the assumption that the dipole strength at the metal/organic contacts and the ionized state density are proportional to the prevailing densities of organic materials. Since the ionized state density in MEH-OPV5 was zero, the N_i of a co-deposited film is solely determined by the volume fraction of C_{60} in the blend. As we deposited C_{60} and MEH-OPV5 in a ration of 1:1, the resulting N_{i} is consequently assumed to be half of the N_{i} determined for bare C_{60} films, while $W_{0\text{V}}$ is roughly two times larger, as confirmed by CV measurements (Table 7.2).

Accordingly, we anticipated that the dipole strength δ is proportional to the surface density σ_{S} of the organic medium: $\delta \propto \sigma_{\text{S}}$. The relation between U_{bi} of a blend and the unveiled vacuum-level shifts at the respective interfaces can be rationalized on basis of a schematic raster representation of a random blend as depicted in Fig. 7.7. In terms of vacuum-level shifts, the system can be reduced to four general situations. When MEH-OPV5 forms contact with both electrodes, such as it is depicted in the first line of Fig. 7.7 A and B, the vacuum-level shifts δ_{PM} and δ_{AM} contribute to U_{bi}, while vacuum-level shifts related to the heterojunctions between C_{60} and MEH-OPV5 (δ_{het}) compensate each other, resulting in a zero shift with respect to the heterojunctions. The same holds true when C_{60} is in contact with both electrodes. For situations where MEH-OPV5 forms contact with the anode, while C_{60} is in contact with the cathode and vice versa, the net-heterojunction vacuum-level shifts are $+\delta_{\text{het}}$ and $-\delta_{\text{het}}$, respectively. However, in a 1:1 random blend of MEH-OPV5 and C_{60}, all four situations statistically appear with the same frequency. Thus, in spatial average, solely the interfacial vacuum-level shifts at the metal/organic interfaces contribute to U_{bi} of cells based on random blends, since the averaged vacuum-level shift related to the heterojunctions is zero.

With U_{soc} = 1.1 V of a single-layer MEH-OPV5 cell and an U_{soc} of 0.9 eV predicted by the metal-insulator-metal (MIM) model, the vacuum-level shifts at the metal/MEH-OPV5 interfaces increase the built-in potential by 0.2 eV. The interfacial MEH-OPV5 density in a blended cell, however, is half of the interfacial MEH-OPV5 density in a bare MEH-OPV5 cell, resulting in a dipole-layer strength of only 0.1 eV at the MEH-OPV5/metal interfaces. The same reasoning holds true for the C_{60}/metal interfaces in the blend. Since the vacuum-level shifts in a single-layer C_{60} cell change the U_{soc} by -0.6 eV, our assumption requires a vacuum-level shift contribution from the C_{60}/metal interfaces in the blend to be -0.3 eV. The predicted total vacuum-level shift is then -0.2 eV and U_{soc} of a co-deposited cell should be 0.7 V, which is in good agreement with the measured value (Table 7.2). Although requiring further verification, the proposed simple dilution model is useful to relate cell performance and morphology, since it predicts very accurately the effective ionized state density N_{i}, the saturated open circuit voltage U_{soc} (U_{bi}) and, consequently, the depletion width at zero bias $W_{0\mathrm{V}}$ for co-deposited photovoltaic cells as can be seen from Fig. 7.8.

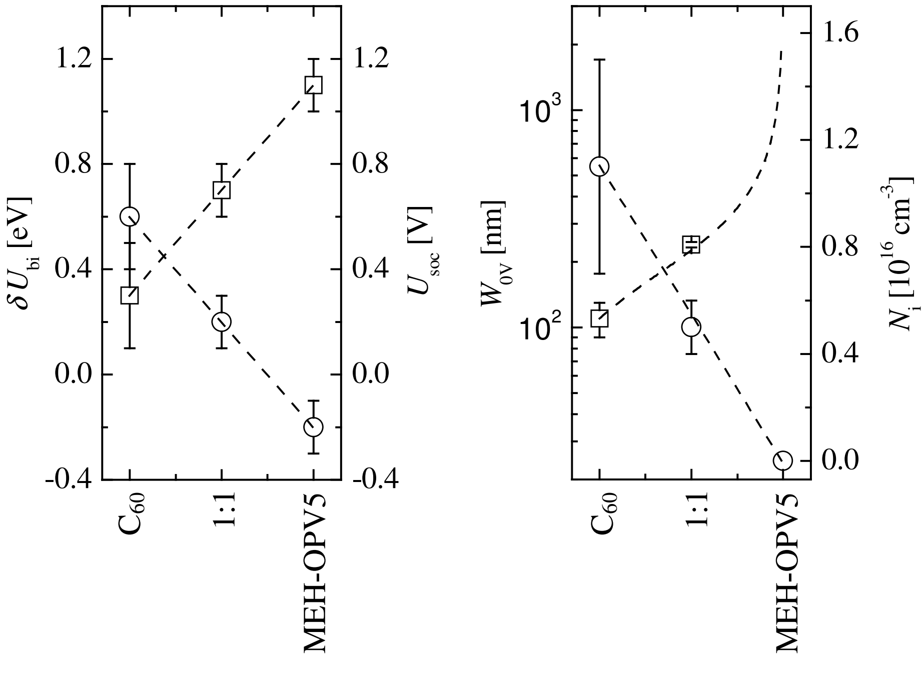

Figure 7.8 *Left*: The dipole layer strength (○) and the saturated open circuit voltage (□) versus the film composition of co-deposited systems, using MEH-OPV5 as donor and C_{60} as acceptor material. Dotted lines indicate the linear dependence on the material surface density. *Right*: The depletion width at zero bias (□) and the ionized state density (○) versus the film composition of co-deposited systems, using MEH-OPV5 as donor and C_{60} as acceptor. The dotted lines correspond to the predicted behavior, assuming the simple dilution model proposed in this study.

7.3 Action spectra and exciton diffusion

For many organic semiconductors, the relationship between the absorption spectrum and the spectral dependence of the photoresponse (action spectrum) can be classified as one of two types. If absorption and action spectra correlate well, i.e. the strongest absorption corresponds to the maximal photoresponse, the photoresponse is said to be *symbatic* to the absorption spectrum. Under other conditions, the spectrum is almost complementary, meaning that the minimum of the action spectrum occurs at the wavelength of strongest absorption. This behavior is termed *antibatic*. The normalized external quantum efficiency (EQE) and absorption spectra of double-layer cells based on the donors MEH-PPV, MEH-OPV5, and Ooct-OPV5 and the acceptor C_{60} are depicted in Fig 7.9. Substrates were maintained at room temperature during deposition. EQE spectra were measured under short circuit conditions and the samples were illuminated from the glass side, i.e. through the donor phase. Obviously, all EQE spectra of the investigated double-layer cells exhibited *antibatic* behavior at short circuit conditions, while bulk heterojunction photovoltaic cells typically show *symbatic* behavior [5]. Phenomenologically, we explain the *antibatic* behavior of the action spectra by the interplay of the pre-absorption of incident light in the donor phase, resulting in a weaker photon flux through the sensitive volume close to the donor/acceptor interface, with the exciton generation cross-section, which determines

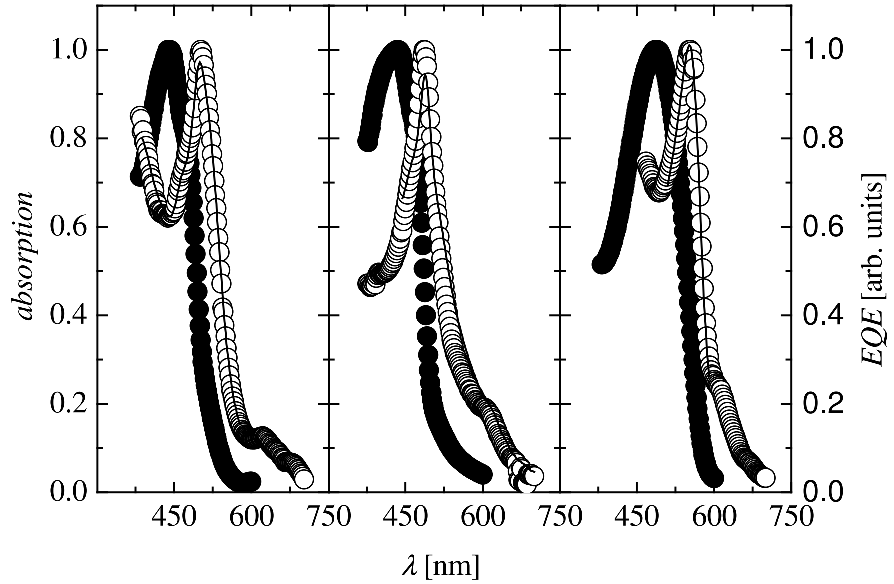

Figure 7.9 Normalized absorption (●) and action spectra (external quantum efficiency) (○) of double-layer photovoltaic cells with Ooct-OPV5 (130 nm) (left), MEH-OPV5 (105 nm) (middle), and MEH-PPV (100 nm) (right) as donor and C_{60} (~20 nm) as acceptor. The lines are fits using Eq. 7.4.

the number of generated excitons per photon. Since the extinction coefficient of C_{60} is small at the wavelengths of interest, we ignore photocurrents resulting from excitons generated in the C_{60} phase. The generation rate of excitons at the distance z from the anode upon an initial photon flux j_p is proportional to the photon flux $j_p Exp[-\alpha z]$ and the generation cross-section, which is characterized by the extinction coefficient α. Since almost all excitons within the exciton diffusion length L_e around the heterojunction interface dissociate, the rate of exciton dissociation is approximately given by $\int_{d-L_e}^{d} j_p \alpha Exp[-\alpha z]\partial z$. d is the thickness of the donor layer. The solution is $j_p Exp[-\alpha d](Exp[\alpha L_e]-1)$ and reduces for $\alpha L_e \ll 1$ to $j_p \alpha L_e Exp[-\alpha d]$. Thus, in the regime of very low absorption, the exciton generation cross-section becomes too small to result in strong exciton generation, even though the photon flux is high. The rate of exciton dissociation increases linearly with α. For stronger absorption, the rate of exciton dissociation is at its maximum and tends to decrease for even higher α, because the preabsorption of light reduces the photon flux through the active volume to such extend that even the large exciton generation cross-section does not allow significant exciton generation close to the heterojunction interface. As depicted in Fig. 7.10, EQE versus α, therefore, exhibited a bell-shaped form, with the maximal photoresponse being related to the thickness of the donor layer. The action spectra of non-optimized double-layer donor/acceptor photovoltaic cells are, hence, generally *antibatic*. In contrast, the exciton dissociation rate in a perfect blend can be approximated to $j_p(1-Exp[-\alpha d])$, and the maximum of the action spectrum coincides with the maximum of absorption.

For a more detailed analysis of the action spectra of double-layer cells, we derived the photovoltaic quantum efficiency, considering diffusive transport of excitons in the donor phase by solving the following steady-state continuity equation:

Eq. 7.2

$$0=\frac{\partial n_e(z)}{\partial t}=g_e(z)-\frac{n_e(z)}{\tau}+D\frac{\partial^2 n_e(z)}{\partial z^2}$$

where $g_e(z)$ is the exciton generation rate, τ is the exciton lifetime, D is the exciton diffusion constant, and n_e is the density of excitons. The exciton generation rate is given by $g_e(z) \propto \alpha j_p Exp[-\alpha z]$. Interference of the incident light beam with back-reflected light, considering the actual device architecture, was ignored [26]. We regarded excitons to immediately dissociate via electron transfer from the donor to the acceptor when reaching the donor/acceptor interface, which results in the boundary condition $n_e(d) = 0$. Likewise, the boundary condition at the metal/donor interface was assumed to be $n_e(0) = 0$. This is justified, since excitons are quenched via energy transfer close to metal/organic interfaces. In first instance, we ignored the typical interaction distances for efficient charge and energy transfer. The photocurrent was taken to be proportional to the current j_e of excitons through the donor/acceptor interface:

Eq. 7.3
$$j_e = -D\left.\frac{\partial n_e(z)}{\partial z}\right|_{z=d}$$

The solution of Eq. 7.2 and Eq. 7.3 considering the assumed boundary conditions is:

Eq. 7.4
$$j_e = j_\mathrm{p}\frac{L_e\alpha\left(\operatorname{Sinh}\left[\frac{d}{L_e}\right]^{-1} - \operatorname{Exp}[-\alpha d]\cdot\left(L_e\alpha + \operatorname{Coth}\left[\frac{d}{L_e}\right]\right)\right)}{(L_e\alpha)^2 - 1}$$

j_e is proportional to the incident photon flux j_p, and depends furthermore on the donor thickness d, the extinction coefficient α, and the exciton diffusion length L_e that is related to the diffusion coefficient and the exciton lifetime by $L_e^2 = D\tau$. Hence, by analyzing the action and the absorption spectra, and by knowing the thickness of the donor layer, one can gain information about the exciton diffusion length in the donor phase.

Assuming exciton diffusion in the donor-type material, the normalized EQE spectra could be modeled with Eq. 7.4 as depicted in Fig. 7.9 and 7.10. While d was determined by atomic force microscopy in tapping mode (TM-AFM), L_e was used as a free parameter. Reasonable fits could be obtained for action spectra from ITO/MEH-PPV/C_{60}/Al devices, requiring an exciton diffusion length in MEH-PPV of 7 ±4 nm.

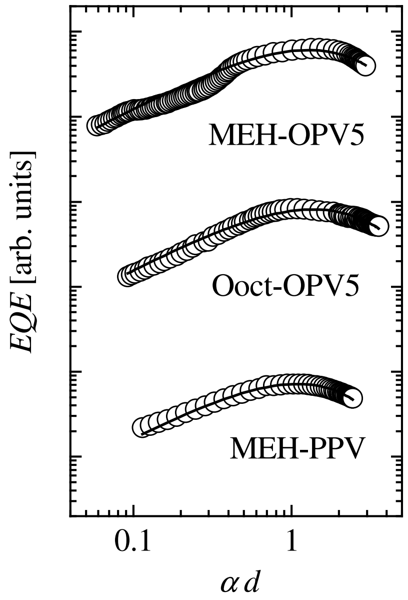

Figure 7.10 The normalized EQE versus the absorption cross-section α for double-layer photovoltaic cells with C_{60} as acceptor and Ooct-OPV5 (130 nm), MEH-OPV5 (105 nm), and MEH-PPV (100 nm) as donor. The lines are fits using Eq. 7.4. Curves are shifted for clarity.

This perfectly matches the exciton diffusion length reported for PPV by Halls *et al.* [26, 27] and is close to the one of MEH-PPV, which has been found to be 10-20 nm [28, 29]. Likewise, an L_e of 20 and 30 nm, respectively, was required to simulate the EQE spectra of double-layer cells based on MEH-OPV5 and Ooct-OPV5, which is considerably larger than that of MEH-PPV. Yet, from Fig. 7.10 it becomes apparent that the unveiled L_e of double-layer cells based on the investigated oligomers are only rough estimates, since the proposed diffusion model only partly predicts the observed EQE spectra. The mismatch of simulated and measured EQE spectra might result from the high surface roughness that is predominant in polycrystalline films. Light scattering, for instance, was clearly visible in this type of films, and the assumption that a simple exponential decay function describes the light intensity distribution in the sample is, hence, not valid.

The high surface roughness of the oligomeric thin films might, moreover, explain their larger L_e if compared to the polymer. In the used one-dimensional exciton diffusion model, L_e is determined by the assumption that double-layer cells are truly planar. Due to roughening of the heterojunction interface, which is predominant for cells based on Ooct-OPV5, this assumption is not fulfilled and the device thickness in Eq. 7.4 is a matter of distribution. However, the thickness variation, even for vacuum-deposited Ooct-OPV5 thin-films where the RMS film roughness is high, did not result in a considerable variation of the simulated action spectra. In addition, as discussed in section 7.2.2, the effective volume of exciton dissociation is increased if the heterojunction interface roughness is high and, hence, the deduced L_e is overestimated. One can estimate the discrepancy of measured and actual L_e by dilating the topographical map obtained by TM-AFM with a sphere of radius L_e as indicated in Fig. 7.11. It becomes apparent that the resulting L_e locally exceeds the factual L_e in regions of strong topographical variations, but yields an overestimation of L_e below 3 nm in spatial average. This is again a consequence of the fact that the diameter of the topological features exceeded the actual exciton diffusion length. Nonetheless, the unveiled disparity in L_e of the investigated donor materials correlates with their degree of crystallinity and might, hence, have its origin in differences in inter- and intramolecular organization, affecting the excitation lifetime and transport. It is likely that in highly disordered films of MEH-PPV exciton diffusion is suppressed, while in the tighter packed crystalline structures it is promoted. It has been, for example, reported that the exciton diffusion length in single crystals of anthracene is close to 50 nm [30], whereas the one in disordered films of PPV is below 10 nm [26, 27]. The low L_e found for MEH-PPV is partly related to its short excitation lifetime of 200-300 ps [8, 9]. With $L_e^2 = D\tau$ and an L_e of 7 nm , a diffusion constant in MEH-PPV of 2×10^{-7} m^2/s is obtained, which is not contradictory to previous results [8]. In contrast, however, an excitation lifetime of 1.2-1.7 ns [31] has been reported for vacuum-deposited thin films of Ooct-OPV5, which is considerably larger than the one of MEH-PPV. L_e in Ooct-OPV5 thin films is, hence, supposed to exceed that of MEH-PPV. Assuming an L_e of 30 nm for Ooct-OPV5 thin films, a diffusion constant of 5×10^{-7} m^2/s was estimated, comprehending a superior exciton transport in polycrystalline Ooct-OPV5 compared to disordered MEH-PPV thin films.

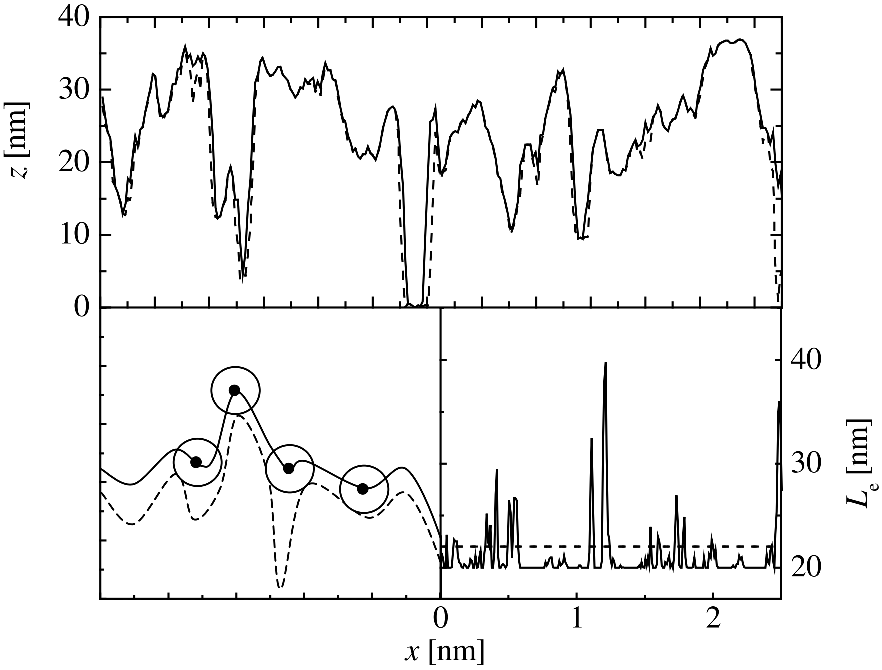

Figure 7.11 *Top*: Line scan (---) of the topographical map of Ooct-OPV5 deposited on PEDOT:PSS. Margins of the volume of efficient exciton dissociation determined by L_e (—). L_e was assumed to be 20 nm. *Left, bottom*: Schematic picture of the determination of the active volume in terms of exciton dissociation: excitons can diffuse in a sphere of radius L_e. (---) is a topographical line scan. (—) represents the limiting surface for efficient exciton dissociation. *Right, bottom*: Distributed L_e due to roughness effects (—) and spatial average of L_e (---).

7.4 A donor/acceptor block copolymer

Nowadays, the organization of donor and acceptor phases in bulk heterojunction photovoltaic cells is believed to be one of the technological challenges, which have to be tackled in order to bring organic photovoltaic cells closer to practical applications. Besides the fact that the lateral dimensions of donor and acceptor phases are required to be in the range of L_e, long-range order through the entire semiconducting film is essential for efficient charge carrier read-out. The establishment of phase separation in the nm-scale with long-range order, however, is not trivial, since the blending of two different molecular species usually results in a phase separation in the μm-scale with strong molecular intermixing and poor long-range correlation.

For the creation of the essential structural order in the donor/acceptor composite, the self-organization of block copolymers by micro-phase separation can be exploited [32-36]. The chemical link between the blocks of different chemical nature restricts the molecular ordering to the radius of gyration of the macromolecule, which typically is in the nm-range. The micro-phase separation of non-crystalline coil-coil diblock copolymers is governed by the interaction enthalpy and the degree of polymerization, while the stability limit depends on the block length ratio. A variety of continuous and co-continuous two-phase morphologies, such as lamella, cylindrical or spherical morphologies have been observed. Certainly, the co-continuous morphologies have to be regarded as highly interesting for organic photovoltaic cells, since they provide a large heterojunction interface and, concomitantly, allow bipolar charge carrier read-out.

Tailoring of organic donor/acceptor phases by micro-phase separation can be achieved by implementing the donor and the acceptor functionality into different individual blocks. The functionalities can either be introduced into the backbone of the polymer block or into its sidechains. A donor/acceptor diblock copolymer with a conjugated PPV-like donor block (poly(1,4-(2,5-dioctyloxy)phenylene vinylene), DOO-PPV) and a coil-like copolymer block of styrene (S) and methylstyrene (MS) functionalized with C_{60} has been synthesized and extensively characterized [37-42]. In the frame of this work, we probed the establishment of micro-phase separation by TM-AFM. TM-AFM supplies information about the variations in the tip/surface interaction along the scanned area by investigating the phase change in the tip oscillation, thereby revealing the lateral distribution of regions with different chemical nature. In a simple picture, the rod-like DOO-PPV block can be regarded to be rigid compared to the flexible PS block, which results in a phase contrast between areas rich of PPV and areas mostly consisting of PS. Unfortunately, only information about the surface can be obtained and the spatial phase distribution remains inaccessible.

We investigated the topography and the phase contrast of thin films of DOO-PPV-b-P(S-stat-C_{60}MS) and of DOO-PPV-b-P(S-stat-ChloroMS) that was not functionalized with C_{60}. Both films were casted from chloroform on mica. Chloroform is a good solvent for both blocks, and self-organization in solution, such as micellization, should virtually not occur. The typical layer thickness was about 80 nm. While in both cases, the topography was rather smooth with a RMS roughness below 2 nm within the scanned area, phase contrast was clearly visible, suggesting a phase-separated morphology. The phase contrast maps revealed elongated features, but long-range order was not detectable in both cases. The elongated features in the DOO-PPV-b-P(S-stat-C_{60}MS) diblock copolymer exhibited a fairly uniform width of approximately 9 nm, which is comparable to the two-fold DOO-PPV block length of 4 nm. Phase contrast maps thus revealed a micro-phase separation in the range of the exciton diffusion length, a situation we intended to achieve in order to make the whole volume of the semiconducting layer sensitive for efficient exciton dissociation. The phase contrast maps, however, were not typical for micro-phase separated coil-coil-like block copolymers. The low molecular weight of the diblock copolymers, resulting in a weak phase segregation, and the rod-like character of the DOO-PPV block may explain the poor long-range ordering of the phase separation. Furthermore, each PS block embraced 28 methylstyrenes, while solely an average of 13 fullerenes were attached. Hence, bis-addition of two MS groups to each fullerene can be assumed. This observation suggests less flexible and, most likely, cross-linked polystyrene blocks that hinder the formation of micro-phases and may additionally reduce the solubility of the

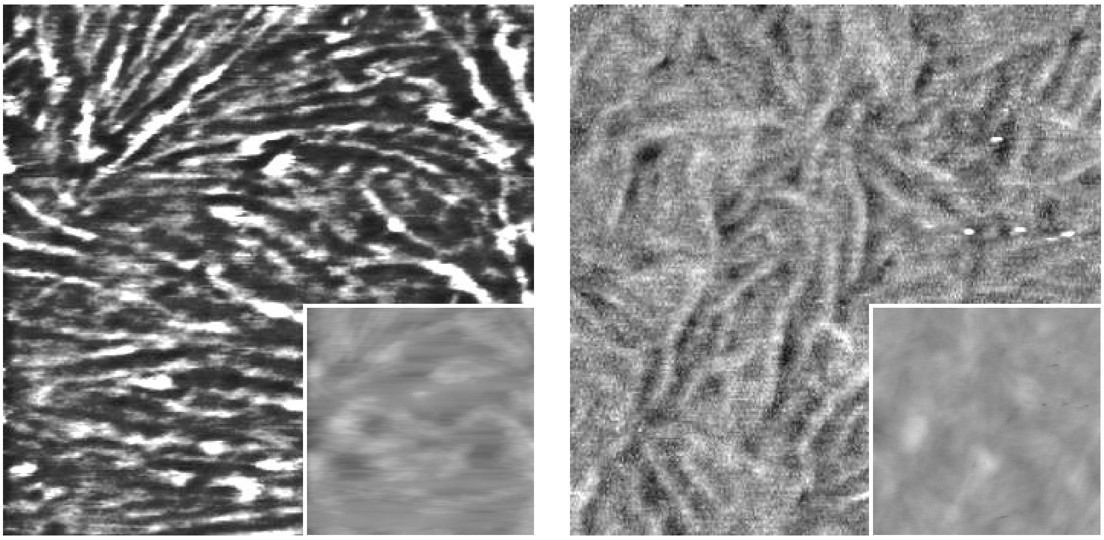

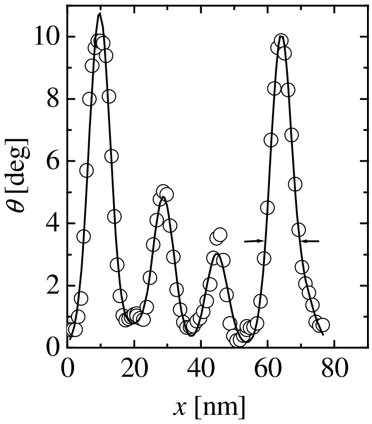

Figure 7.12 Topographical (*insert top*, 10 nm maximum) and phase contrast maps (*top*, 10 degree maximum) of thin films based on DOO-PPV-b-p(S-stat-C60MS) (400×400 nm) (left) and DOO-PPV-b-p(S-stat-ChloroMS) (right) (200×200nm). The width of the elongated features is about 9 nm (*bottom left*).

diblock copolymer in solvents like chloroform, toluene or dichlorobenzene. The poor processability and film-forming properties of the used diblock copolymer support this assumption.

The photovoltaic properties of cells based on the DOO-PPV-b-P(S-stat-C_{60}MS) diblock copolymer in an ITO/PEDOT:PSS/DOO-PPV-b-P(S-stat-C_{60}MS)/Al structure were compared to the ones of cells based on a blend of the DOO-PPV homopolymer and a statistical copolymer P(S-stat-C_{60}MS) in a 1:1 molar ratio. Both the diblock copolymer and the statistical copolymer P(S-stat-C_{60}MS) contained the same amount of C_{60} and the conjugation length of the DOO-PPV homopolymer was as long as the one of the DOO-PPV block in the block copolymer. Differences in the photovoltaic performance can, therefore, be attributed to morphological differences between the diblock copolymer and the blend. Both cells revealed a rather poor photovoltaic response (Fig. 7.13). The fact, however, that *S* of the diblock copolymer is much higher than of the blend justifies the use of block copolymers in photovoltaics. Even though the exciton dissociation interface is large in diblock copolymers, the weak long-range order and the narrow donor and acceptor phases may result in non-

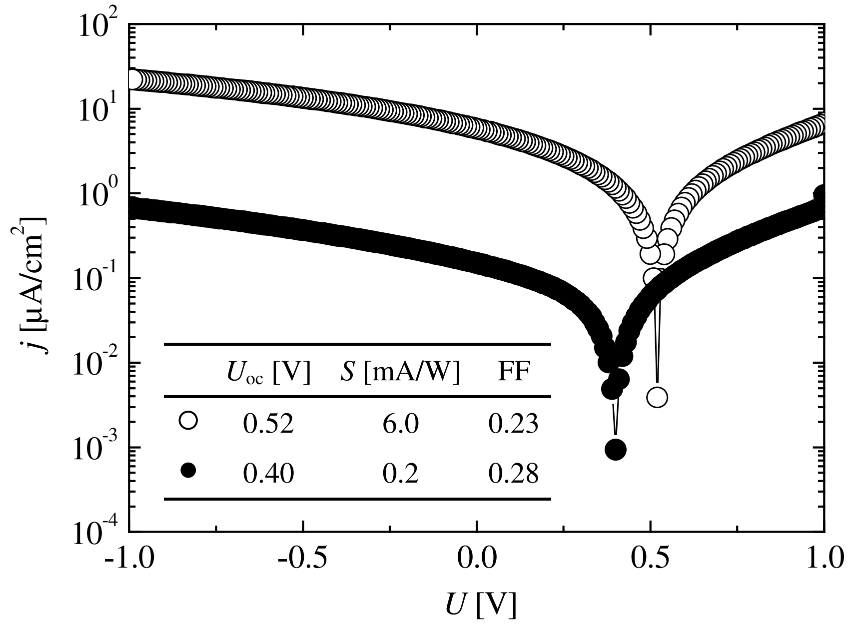

	U_{oc} [V]	S [mA/W]	FF
○	0.52	6.0	0.23
●	0.40	0.2	0.28

Figure 7.13 Photovoltaic response of a PPV-b-P(S-stat-C_{60}MS) donor/acceptor block copolymer (○) compared with a blend of the donor homo- and acceptor copolymer (●) under illumination at 458 nm with P_L = 1 mW/cm^2. The table summarizes the main photovoltaic characteristics.

continuous charge carrier transport paths throughout the semiconductor and in a high trap level density. These effects dramatically reduce the charge carrier transport properties and, therefore, the diode quality, which is reflected in the poor *FF*. In the blend, phase separation resulted in larger domains, and transport paths will most likely be semi-continuous, which demonstrates the importance of the mesoscopic phase organization. Optimization of the morphologies for both cases is, therefore, still required in order to give a conclusive answer to the question whether micro-phase separation results in a superior photovoltaic performance. Nonetheless, it is promising that a 30-fold increase in S could be achieved by replacing the blend of the donor and acceptor polymers by their corresponding block copolymer.

7.5 Conclusion

In this section, we reported on the influence of the thin-film morphology on the photovoltaic cell performance of donor/acceptor photovoltaic cells. The difference in monochromatic η between double-layer and co-deposited structures based on MEH-OPV5 and C_{60} could be rationalized in terms of charge carrier transport phenomena, interfacial effects, exciton diffusion, and morphology.

In particular, we found that the open circuit voltage in the investigated cells strongly depended on interfacial interactions, resulting in a lower U_{oc} in co- than in consecutively deposited cells. This was elucidated on basis of a simple dilution model, which relates the open circuit voltage of co-deposited cells to interfacial interactions, taking the blend morphology into account.

From action spectra measurements, the exciton diffusion length for polymeric and oligomeric moieties could be estimated. An apparent increase of L_e with the degree of crystallinity was unveiled. We believe that the long exciton diffusion length found for MEH-OPV5 makes a large volume fraction of the donor material in double-layer cells susceptible for exciton dissociation, bringing S close to the one of blended cells. Concomitantly, a non-optimal phase separation in the blend can be assumed, contributing to the weak disparity in photovoltaic sensitivities that were found for co- and consecutively deposited photovoltaic cells. We discussed, furthermore, the influence of heterojunction roughness in double-layer systems on the accessible volume fraction for efficient exciton dissociation. Although a high surface roughness was unveiled, no substantially increased heterojunction interface could be confirmed. Hence, the increase in heterojunction interface due to surface roughness is regarded to be only secondarily responsible for the unveiled weak disparity in S between the two cell types. The relatively large S together with the higher open circuit voltage and superior diode behavior of the consecutively deposited cell, finally resulted in a higher monochromatic external power conversion efficiency than in a co-deposited cell.

The need for improved spatial distribution of donor and acceptor phases in a blend finally led us to use a donor/acceptor diblock copolymer, which exhibited a micro-phase separation in the nm-range. Even though the photovoltaic performance was generally weak, we found that the photovoltaic sensitivity of the diblock copolymer significantly exceeded the one of a blend of the corresponding homopolymers, which demonstrates the potential of functionalized block copolymers in the field of organic photovoltaic cells.

References

[1] J. J. M. Halls, C. A. Walsh, N. C. Greenham, E. A. Marseglia, R. H. Friend, S. C. Moratti and A. B. Holms, Nature **376**, 498 (1995).

[2] G. Yu, J. Gao, J. C. Hummelen, F. Wudl and A. J. Heeger, Science **270**, 1789 (1995).

[3] M. Granström, K. Petritsch, A. C. Arias, A. Lux, M. R. Anderson and R. H. Friend, Nature **395**, 257 (1998).

[4] L. S. Roman, W. Mammo, L. A. A. Petterson, M. R. Andersson and O. Inganäs, Adv. Mater. **10**, 774 (1998).

[5] S. E. Shaheen, C. J. Brabec, N. S. Sariciftci, F. Padinger, T. Fromherz and J. C. Hummelen, Appl. Phys. Lett. **78**, 841 (2001).

[6] A. Goetzberg and C. Hebling, Solar Energy Materials & Solar Cells **62**, 1 (2000).

[7] E. L. Frankevich, A. A. Lymarev, I. Sokolik, F. Karasz, S. Blumstengel, S. Baughman and H. H. Hörhold, Phys. Rev. B **46**, 9320 (1992).

[8] M. Gailberger and H. Bässler, Phys. Rev. B **44**, 8643 (1991).

[9] H. Becker, A. Lux, A. B. Holmes and R. H. Friend, Synth. Met. **85**, 1289 (1997).

[10] N. S. Sariciftci, L. Smilowitz, A. J. Heeger and F. Wudl, Science **258**, 1474 (1992).

[11] C. W. Tang, Appl. Phys. Lett. **48**, 183 (1986).

[12] P. Peumans and S. R. Forrest, Appl. Phys. Lett. **79**, 126 (2001).

[13] C. Melzer, V. V. Krasnikov and G. Hadziioannou, Appl. Phys. Lett. **82**, 3101 (2003).

[14] L. Ouali, V. V. Krasnikov, U. Stalmach and G. Hadziioannou, Adv. Mater. **11**, 1515 (1999).

[15] A. M. Goodman and A. Rose, J. Appl. Phys. **42**, 2823 (1971).

[16] V. D. Mihailetchi, J. A. Knoster and P. W. M. Blom, *to be published* (2004).

[17] C. Melzer, E. J. Koop, V. D. Mihailetchi and P. W. M. Blom, Adv. Funct. Mater. (2004), *accepted.*

[18] T. Munters, T. Martens, L. Goris, V. Vrindts and J. Manca, Thin Solid Films **403-404**, 247 (2002).

[19] S. M. Sze, *Physics of Semiconductor Devices*, Wiley & Sons Inc., New York (1981).

[20] N. Hayashi, H. Ishii, Y. Ouchi and K. Seki, J. Appl. Phys. **92**, 3784 (2002).

[21] S. C. Veenstra, A. Heeres, G. Hadziioannou, G. A. Sawatzky and H. T. Jonkman, Appl. Phys. A: Mater. Sci. Proc. **75**, 661 (2002).

[22] S. C. Veenstra, U. Stalmach, V. V. Krasnikov, G. Hadziioannou, H. T. Jonkman, A. Heeres and G. A. Sawatzky, Appl. Phys. Lett. **76**, 2253 (2000).

[23] *Thesis:* S. C. Veenstra, *Electronic Structure of Molecular Systems. From Gas Phase to Thin Films to Devices*, Polymer Chemistry Rijksuniversiteit Groningen, Groningen (2002).

[24] C. M. Ramsdale, J. A. Baker, A. C. Arias, J. D. MacKenzie, R. H. Friend and N. C. Greenham, J. Appl. Phys. **92**, 4266 (2002).

[25] J. A. Baker, C. M. Ramsdale and N. C. Greenham, Phys. Rev. B **67**, 075205 (2003).

[26] J. J. M. Halls, K. Pichler, R. H. Friend, S. C. Moratti and A. B. Holms, Appl. Phys. Lett. **68**, 3120 (1996).

[27] J. J. M. Halls, K. Pichler, R. H. Friend, S. C. Moratti and A. B. Holmes, Synth. Met. **77**, 277 (1996).

[28] T. J. Savenije, J. M. Warman and A. Goossens, Chem. Phys. Lett. **287**, 148 (1998).

[29] L. Smilowitz, A. Hays, A. J. Heeger, G. Wang and J. E. J. Bowers, J. Chem. Phys. **98**, 6505 (1993).

[30] M. D. Cohen, E. Klein and Z. Ludmer, Chem. Phys. Lett. **37**, 611 (1976).

[31] *Thesis:* H. J. Brouwer, *Semiconducting Polymers for Light-Emitting Diodes and Lasers*, Polymer Chemistry Rijksuniversiteit Groningen, Groningen (1998).

[32] E. Helfand and Z. R. Wassermann, *Development in Block Copolymers-1*, Applied Science Publisher, New York (1982).

[33] F. S. Bates and G. H. Fredrickson, Annu. Rev. Phys. Chem. **41**, 525 (1990).

[34] F. S. Bates, Science **251**, 898 (1991).

[35] T. P. Lodge and M. J. Muthukumar, Phys. Chem. **100**, 13275 (1996).

[36] S. I. Stupp, V. Le Bonheur, K. Walker, L. S. Li, K. E. Huggins, M. Keser and A. Amstutz, Science **276**, 384 (1997).

[37] U. Stalmach, B. de Boer, C. Videlot, P. F. van Hutten and G. Hadziioannou, J. Am. Chem. Soc. **122**, 5464 (2000).

[38] B. de Boer, U. Stalmach, H. Nijland and G. Hadziioannou, Adv. Mater. **12**, 1581 (2000).

[39] U. Stalmach, B. de Boer, A. D. Post, P. F. van Hutten and G. Hadziioannou, Angew. Chem. Int. Ed. **40**, 428 (2001).

[40] B. de Boer, U. Stalmach, P. F. van Hutten, C. Melzer, V. V. Krasnikov and G. Hadziioannou, Polymer **42**, 9097 (2001).

[41] B. de Boer, U. Stalmach, C. Melzer and G. Hadziioannou, Synth. Met. **121**, 1541 (2001).

[42] *Thesis:* B. de Boer, *Design, Synthesis, Morphology and Properties of Semiconducting Block Copolymers for Photonic Applications*, Polymer Chemistry Rijksuniversiteit Groningen, Groningen (2001).

Summary

Nowadays, optoelectronic elements but also rectifiers and transistors are still primarily based on inorganic semiconductors, like intrinsic (Ge, Si) or III-V (GaAs, InSb) semiconductors. Already in the 1960's, however, a new class of materials entered this field of technology: the organic semiconductor. In particular, conjugated polymeric compounds are promising candidates for optoelectronic elements, since they can be easily processed, which reduces the production cost of the desired products, and they are light-weighted and flexible, opening new perspectives for applications such as displays or solar cells. Recently, commercial products incorporating such organic semiconductors emerged on the marked (*Chapter 1*). In Fig. 1 some examples of conjugated organic semiconductors are depicted.

Organic semiconductors possess intrinsic properties that are quite different from those of the usually used inorganic semiconductors. While, for instance, inorganic semiconductors display an atomic crystalline structure with long-range order, conjugated polymers form a disordered bulk matter with weak intermolecular interaction, which dramatically influences their semiconductor properties and the operation of the desired device. In order to bring semiconductor devices based on organic compounds closer to industrial applicability, it is therefore required to learn more about the relation between the specific characteristics of organic materials and the general device performance, which was the major purpose of this thesis.

In *Chapter 2*, the experimental setup used to study the device characteristics of organic rectifiers and optoelectronic elements based on different organic compounds was outlined. The development of an optimized infrastructure for device preparation and characterization constituted an important part of the presented research project. The design of the constructed glove-box system, consisting of three interconnected boxes to allow the preparation and characterization of optoelectronic elements and diodes in an inert environment, was thoroughly described. In this system, wet processing and thermal vacuum deposition facilities as well as a variety of automated

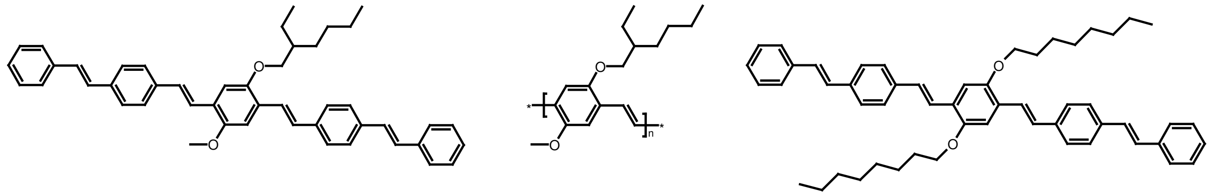

MEH-OPV5

MEH-PPV

Ooct-OPV5

Figure 1 Oligomeric and polymeric organic semiconductors investigated in this study. From left to the right the chemical structures of MEH-OPV5, MEH-PPV and Ooct-OPV5 are depicted.

measurement units were implemented.

In *Chapter 3*, a phenomenological charge carrier injection model based on the decisive aspects of charge injection from a metal to a disordered organic semiconductor was presented. In disordered organic semiconductors, charge carriers are strongly localized and charge carrier transport involves subsequent thermally assisted hopping processes along localized states. Since the extension of the electronic wavefunction of the metal charges into the semiconductor is smaller than the typical nearest neighbor hopping distance, we assumed that thermally activated charge carriers in the metal primarily populate the first mono-layer of the organic semiconductor, establishing a charge carrier density according to the Boltzmann statistics. The injected charges then have to escape their image charges by further nearest neighbor hopping events. Comparison of the injection model with experimental data obtained from injection-limited unipolar rectifiers based on a substituted oligo(phenylene vinylene) (MEH-OPV5, Fig. 1) revealed the importance of disorder effects, involving a disorder-controlled charge carrier mobility, and a disorder induced lowering of the injection barrier. These disorder effects were introduced in a phenomenological way to the model. Perfect agreement between measured and simulated current-voltage relations was obtained.

In *Chapter 4*, the impact of disorder on the charge carrier transport and, in more general terms, on the device characteristics of unipolar rectifiers was discussed on basis of a comparison between MEH-OPV5 and its polymeric counterpart MEH-PPV (Fig. 1). The hole mobility in the highly disordered MEH-PPV was found to be below the one of its oligomeric counterpart, and to be more field-dependent. The different transport properties were attributed to a substantial disparity in disorder energies, which we believe to cause dissimilar current limitations in the inspected unipolar rectifiers. In diodes based on the strongly disordered polymer, the hole injection barrier was effectively lowered by the disorder-induced broadening of the density of states. This resulted in a substantial charging of the semiconductor and, hence, in space-charge-limited current. In contrast, the disorder-induced injection barrier lowering in oligomeric diodes was weaker, and diodes were consequently found to be injection-limited.

In *Chapter 5*, we investigated the relation between the morphology and the charge transport properties of polycrystalline thin films deposited on a typical anode material used in the field of organic electronics. Thin films of a substituted highly crystalline oligo(phenylene vinylene) (Ooct-OPV5) prepared at different deposition conditions were characterized with respect to their structural and hole transport properties. We found that the hole mobility in Ooct-OPV5 thin films increased and became less field-dependent in films prepared at higher substrate temperatures. This observation was primarily related to the increase in crystal size and quality, reducing the disorder energy, the density of traps, and grain boundaries in the thin film. Moreover, an increased substrate temperature resulted in a change of the relative appearance of two polymorphs and their orientation towards the preferential current direction. While one polymorph was predominant when films were deposited at low substrate temperature, another solely existed for substrate temperatures above 60°C. Yet, the influence of the relative occurrence of the high- and low-temperature polymorph and their crystal orientation towards the preferential current direction on the hole transport properties could not be seized completely, since the crystal structure of the low-temperature polymorph is not known.

In *Chapter 6*, the performance of organic thin-film diodes was related to their respective experimentally obtained energy diagrams. It has been shown that the deposition of small organic molecules on metals occasionally results in a mismatch of vacuum-levels of the metal and the organic semiconductor, caused by an electric field at the interface. We demonstrated that interfacial vacuum-level shifts are detrimental for the charge carrier transfer process from metals to organic semiconductors, since these shifts alter the energy barrier that charges have to overcome in order to be emitted from the metal. In this context, strong interactions between MEH-OPV5 and Ag or Au were found to result in large vacuum-level shifts at the metal/organic interface and in high hole and electron injection barriers, which prevented any measurable current through the respective thin-film diodes. In contrast, the interaction between Buckminster fullerene (C_{60}) and Ag or Au resulted in moderate electron injection barriers, and substantial electron injection currents were observed. Besides, also the FCC-SC phase transition of C_{60} arising at 250 K was reflected in the device characteristics.

In *Chapter 7*, we reported on the relation between the thin-film morphology and the photovoltaic cell performance of donor/acceptor photovoltaic cells, employing MEH-OPV5 as donor and C_{60} as acceptor material. We compared cells of planar double-layer structure with cells consisting of a random blend of both moieties. The device design and operation principle of double-layer heterojunction photovoltaic cells is depicted in Fig. 2. The superior monochromatic power conversion efficiency for double-layer cells resulted from the fact that its slightly lower photovoltaic sensitivity was compensated by a higher fill factor and open circuit voltage. Typically, the optical excitation of organic semiconductors results in strongly bound electron hole pairs (excitons), which need to be dissociated before they are susceptible to the external circuit. The dissociation of excitons efficiently occurs at the interface of two materials with different ionization potentials and electron affinities, leading to the common use of donor/acceptor-type photovoltaic systems. However, since the exciton diffusion length is typically shorter than the light absorption depth, a percolation of donor/acceptor heterojunctions is more efficient in terms of exciton dissociation than a conventional double-layer structure with a single planar donor/acceptor heterojunction, which led to higher photovoltaic sensitivities of the investigated blended cells. Yet, the difference in the photovoltaic sensitivity was small, and we assigned this primarily to a not optimized phase separation in the blend, and a long exciton diffusion length in the donor material. In this respect, the increased heterojunction interface in the double-layer structure induced by the pronounced roughness of the donor film was only of secondary importance. Moreover, we found that the open circuit voltage in the investigated cells strongly depended on the interfacial interactions that were unveiled in *Chapter 6*, resulting in a lower open circuit voltage in the blended than in the

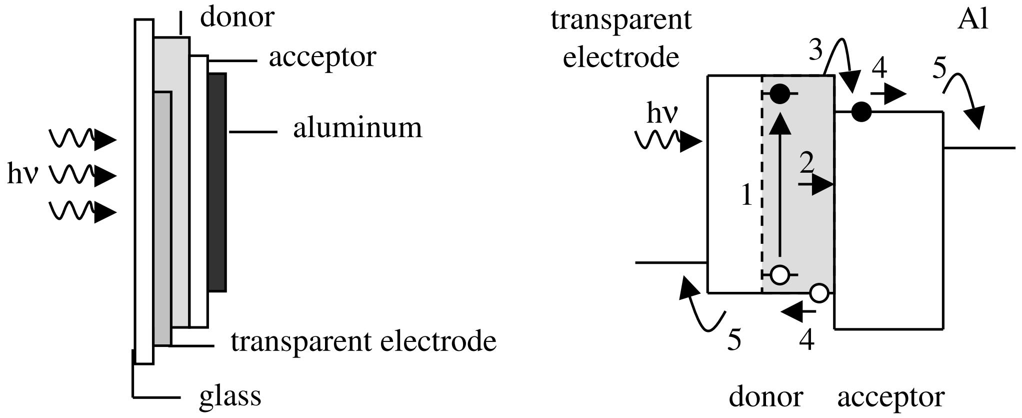

Figure 2 Schematic structure of a double-layer heterojunction photovoltaic cell. The cell is illuminated from the glass side through the donor material. Typical donor and acceptor materials are poly(phenylene vinylene)s and Buckminster-fullerene C_{60}, respectively. On basis of the respective energy diagram, the operation principle is illustrated: (1) Exciton formation due to light absorption; (2) Exciton diffusion; (3) Exciton dissociation at the donor/acceptor interface. Only excitons created in the range of the exciton diffusion length (gray area) close to the heterojunction interface are susceptible for exciton dissociation. (4); Charge transport; (5) Charge carrier collection at the electrodes.

double-layer heterojunction cell. This observation was rationalized on basis of a simple dilution model, which we used to correlate the open circuit voltage of a bulk heterojunction cell with interfacial interactions, taking into account the blend morphology.

The need for improved spatial distribution of donor and acceptor phases in a blend finally led us to use a donor/acceptor diblock copolymer, which exhibited a micro-phase separation in the nm-range, comparable to the typical exciton diffusion length. As a consequence, the photovoltaic sensitivity of the diblock copolymer significantly exceeded the one of a blend of the corresponding homopolymers, even though the photovoltaic performance was generally weak. The poor photovoltaic performance was related to the missing long-range order in the film, resulting in weak transport properties.

In conclusion, we investigated rectifiers and optoelectronic elements based on oligomeric and polymeric organic semiconductors with respect to their device characteristics and related those to their morphology. We addressed disordered, crystalline and composite semiconducting systems. It was demonstrated that within a broad range of length-scales, the organization of the used organic semiconducting system is of crucial importance for the performance of the respective thin-film devices. From the molecular conformation, the intermolecular arrangement up to the long-range organization of organic semiconducting systems, structural properties have to be tuned, in order to obtain devices that can satisfy the industrial demands.

Samenvatting

Heden ten dagen zijn niet alleen optoelektronische elementen, maar ook gelijkrichters en transistoren nog steeds gebaseerd op anorganische halfgeleiders zoals intrinsieke (Ge, Si) of III-IV (GaAs, InSb) halfgeleiders. Reeds in de zestiger jaren kwam een nieuwe klasse van materialen in dit technologieveld: de organische halfgeleider. De geconjugeerde polymere verbindingen zijn met name veelbelovend als optoelektronische elementen, omdat deze makkelijk te verwerken zijn waardoor ze de kostprijs van het gewenste product reduceren, en omdat ze een laag gewicht kennen en flexibel zijn waardoor perspectief bieden voor nieuwe applicaties zoals beeldschermen en zonnecellen. Recentelijk zijn de eerste commerciële producten bestaande uit organische halfgeleiders op de markt verschenen (*Hoofdstuk 1*). Fig. 1 geeft enige voorbeelden van deze geconjugeerde organische halfgeleiders weer.

Organische halfgeleiders bezitten een intrinsieke eigenschap die behoorlijk afwijkt ten opzichte van anorganische halfgeleiders. Anorganische halfgeleiders hebben een atomaire kristallijne structuur met een regelmatige pakking over grote afstanden, terwijl geconjugeerde polymeren een ongeordend materiaal vormen met erg zwakke intermoleculaire interacties welke een zeer grote invloed hebben op de halfgeleider eigenschappen en de uiteindelijk prestatie van het element (device) waarin deze organische materialen zijn toegepast. Om deze organische halfgeleider elementen dichter bij industriële toepassingen te brengen vereist daarom een verdere kennis van de relatie tussen de specifieke karakteristieken van het organische materiaal en de prestaties van het element (device). Dit is dan ook het belangrijkste doel van dit proefschrift.

In *Hoofdstuk 2* worden de experimentele methoden behandeld die gebruikt zijn om de karakteristieken van de organische gelijkrichters en optoelektronische elementen gebaseerd op verschillende organische verbindingen te bestuderen. De ontwikkeling van een geoptimaliseerde infrastructuur voor het prepareren en karakteriseren van de devices beslaat een belangrijk deel van dit huidige onderzoeksproject. Het ontwerp van

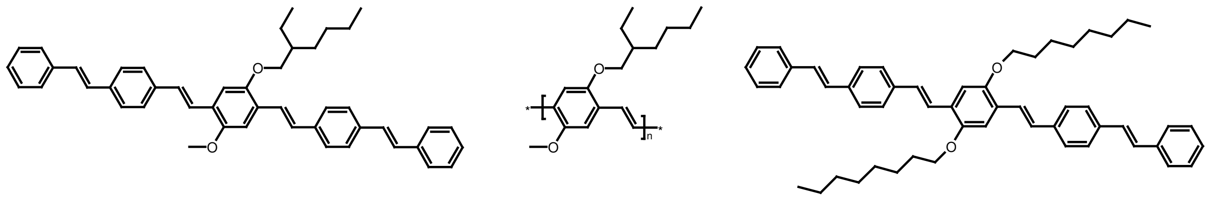

MEH-OPV5 MEH-PPV Ooct-OPV5

Figuur 1 De bestudeerde oligomere en polymere organische halfgeleiders. Van links naar rechts de chemische structuur van MEH–OPV5, MEH–PPV en Ooct–OPV5.

het geconstrueerde stikstofkasten systeem, bestaande uit drie onderling verbonden stikstofkasten is uitvoerig beschreven. Dit systeem staat toe om de elementen (devices) te prepareren en te karakteriseren in een inerte atmosfeer door middel van de inbouw van natte verwerkingseenheid (wet-processing) en thermische vacuümdepositie faciliteiten en tevens door de implementatie van een variëteit aan geautomatiseerde meetopstellingen.

In *Hoofdstuk 3* wordt een fenomenologisch ladingsdragerinjectiemodel gebaseerd op een beslissende aspecten van de ladingsinjectie van het metaal in de wanordelijke organische halfgeleider gepresenteerd. In wanordelijke organische halfgeleiders is de landingsdrager sterk gelokaliseerd en het ladingsdragertransport omvat opeenvolgende, thermisch geassisteerde hopping processen langs de gelokaliseerde niveaus. Aangezien de reikwijdte van de elektronische golffunctie van de ladingen in het metaal binnen in de halfgeleider kleiner is dan de typische afstand tussen gelokaliseerde niveaus, nemen we aan dat de thermisch geactiveerde ladingdragers in het metaal met name de eerste monolaag van de organische halfgeleider bezetten en daardoor een ladingsdragerdichtheid aannemen die overeenkomt met de Boltzmann statistiek. De op deze manier geïnjecteerde ladingsdragers moeten vervolgens ontsnappen aan hun compensatie ladingen in het metaal door naar het dichtstbijzijnde gelokaliseerde niveau te springen. Een vergelijking tussen het injectiemodel en de experimentele data die verkregen zijn uit injectie gelimiteerde unipolaire gelijkrichters gebaseerd op gesubstitueerde oligo(fenyleen vinyleen) (MEH-OPV5, Fig. 1) laat zien hoe belangrijk deze wanordelijke effecten, die bestaan uit wanorde gecontroleerde ladingsdragermobiliteit en wanorde geïnduceerde verlaging van de injectie barrière, zijn. Deze wanorde-effecten zijn fenomenologisch geïntroduceerd in het model. Een perfecte overeenstemming tussen de gemeten en gesimuleerde stroom–voltage karakteristieken is verkregen.

In *Hoofdstuk 4* wordt de impact van de wanorde op de ladingsdragertransport en, meer algemeen, de impact van de wanorde op karakteristieken van unipolaire gelijkrichters uiteen gezet en bediscussieerd op basis van een vergelijking tussen MEH–OPV5 en zijn polymere tegenhanger MEH-PPV (Fig. 1). De gevonden waarde van gatenmobiliteit in het zeer wanordelijke MEH-PPV is lager en meer veld afhankelijk dan in het oligomere materiaal. De verschillende transport eigenschappen zijn toegekend aan de substantiële ongelijkheid van de wanorde energieën, waarvan wij denken dat ze verschillende stroomlimitaties in de unipolaire gelijkrichters veroorzaken. In diodes gebaseerd op het sterk wanordelijke polymeer is de gateninjectiebarrière effectief verlaagd door de wanorde geïnduceerde verbreding van de toestandsdichtheid. Dit resulteert in een substantiële oplading van de halfgeleider en vervolgens een ruimte-ladings-begrensde stroom. In tegenstelling hiermee is de door wanorde geïnduceerde injectiebarrièreverlaging in de oligomere diodes minder en daarom zijn deze diodes injectie gelimiteerd.

In *Hoofdstuk 5* wordt de relatie beschreven tussen de morfologie en de ladingstransport eigenschappen van polykristallijne dunne lagen die zijn opgedampt op

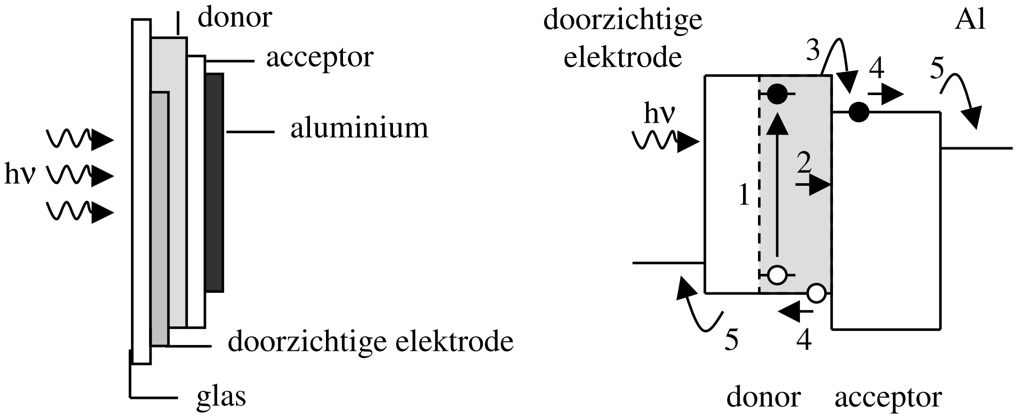

Figuur 2 De schematische structuur van een dubbellaag heterojunctie fotovoltaïsche cel. De cel wordt belicht vanaf de kant van het glas door het donor materiaal. Kenmerkende donor en acceptor materialen zijn respectievelijk poly(fenyleen vinylenen) en Buckminsterfullereen (C_{60}). Op basis van het energie diagram is het werkingsprincipe geïllustreerd: (1) Exciton formatie als gevolg van licht absorptie; (2) Exciton diffusie; (3) Excitondissociatie aan het donor/acceptor interface. Alleen excitonen gevormd binnen de excitondiffusielengte (grijze gebied) dicht bij de heterojunctie interface zijn gevoelig voor excitondissociatie; (4) Lading transport; (5) Ladingdragercollectie door de elektroden.

een bepaald anode materiaal dat wordt gebruikt in het onderzoeksgebied voor organische elektronica. De dunne lagen van een gesubstitueerde hoog kristallijn oligo(fenyleen vinyleen) (Ooct–OPV5), die is geprepareerd onder verschillende opdamp condities, zijn gekarakteriseerd op het gebied van de structurele en gatengeleiding eigenschappen. Hier werd gevonden dat de gatenmobiliteit in dunne lagen van Ooct–OPV5 toeneemt en minder veld afhankelijke worden naar mate de substraat temperatuur hoger is tijdens het opdampen. Deze observatie is voornamelijk gerelateerd aan de toename van de grootte en kwaliteit van de kristallen waardoor de wanorde energie, de ladingsdragervallen (traps) en het aantal grensvlakken van het kristal is afgenomen in de dunne lagen. Bovendien resulteert de toename van de substraat temperatuur in een verandering van de relatieve hoeveelheid van twee polykristallijne structuren en de oriëntatie naar de voorkeursrichting van de stroom. Terwijl één bepaalde polykristallijne structuur hoofdzakelijk aanwezig was indien de dunne lagen waren opgedampt bij lage substraat temperaturen, de andere uitsluitend voor kwam bij substraat temperaturen boven de 60 °C. Doch de invloed van de relatieve aanwezigheid van de twee polykristallijne structuren (gevormd bij hoge en lage temperatuur) kon niet helemaal worden begrepen, omdat de kristalstructuur die bij lage temperatuur wordt verkregen niet bekend is.

In *Hoofdstuk 6* wordt de relatie tussen de prestatie van organische dunne lagen in diodes en de bijbehorende experimenteel verkregen energie diagrammen beschreven. Er is aangetoond dat het opdampen van kleine organische moleculen op metalen incidenteel resulteerde in niet bij elkaar passende vacuümniveaus van het metaal en de organische halfgeleider, die veroorzaakt wordt door een elektrisch veld aan het interface. We demonstreerde dat de verschuiving van de vacuümniveaus aan het interface een nadelige invloed hebben op de processen van de ladingdrageroverdracht van het metaal naar de organische halfgeleider, omdat deze verschuiving de energiebarrière verandert die de ladingen moeten overkomen om uit het metaal te kunnen worden geëmitteerd. In deze context werd een sterke interactie tussen MEH–OPV5 en zilver of goud gevonden, die resulteerde in een grote verschuiving van de vacuümniveaus bij het metaal–organische interface en in een hoge gaten- en elektroninjectiebarrière met als gevolg dat het meten van de stroom door de organische dunne laag diodes onmogelijk werd gemaakt. In tegenstelling met het hiervoor genoemde, resulteerde de interactie tussen het Buckminster-fullereen (C_{60}) en zilver of goud in een gematigde elektroninjectiebarrière, waardoor een substantiële elektroninjectiestroom kon worden geobserveerd. Daarnaast was ook de FCC–SC fase overgang van C_{60} bij 250 K te zien in de karakteristieken van de diode.

In *Hoofdstuk 7* rapporteren we over de relatie tussen de morfologie van de dunne laag en de fotovoltaïsche prestatie van de cel die opgebouwd is uit MEH–OPV5 als donor en C_{60} als acceptor. We vergelijken cellen opgebouwd uit een vlakke dubbellaag structuur met cellen bestaande uit een aselect mengsel van functionaliteiten. Het ontwerp en de werking van de fotovoltaïsche cellen met een dubbellaag heterojunctie is weergegeven in Fig. 2. De superieure monochromatische stroomconversie efficiëntie van de dubbellaagcel is het resultaat van het feit dat de iets lagere fotovoltaïsche gevoeligheid wordt gecompenseerd door een hogere vulfactor en openklemspanning. Kenmerkend is dat de optische excitatie van de organische halfgeleider resulteert in een sterk gebonden elektron–gat paren (excitonen), die moeten worden gescheiden voordat ze beïnvloed kunnen worden door het externe circuit. De dissociatie van de excitonen gebeurd efficiënt aan het interface van twee materialen met verschillende ionisatiepotentialen en elektronaffiniteiten zoals deze in het algemeen worden toegepast in donor/acceptor fotovoltaïsche systemen. Echter, omdat de excitondiffusielengte kenmerkend korter is dan absorptiediepte van het licht, is een percolatie van de donor en acceptor heterojuncties efficiënter op het gebied van excitondissociatie dan een conventionele dubbellaagstructuur met een enkele, vlakke donor/acceptor heterojunctie, waardoor de onderzochte cellen gebaseerd op een aselect mengsel van beide resulteerde in een hoger fotovoltaïsche gevoeligheid. Echter het verschil in de fotovoltaïsche gevoeligheid is klein en we wijzen dit hoofdzakelijk toe aan een niet geoptimaliseerde fasescheiding in het aselecte mengsel en een lange excitondiffusielengte in het donor materiaal. In dit opzicht is de toename van de oppervlakte van de heterojunctie in de dubbellaagstructuur geïnduceerd door een uitgesproken ruwheid van de donor laag alleen van secundair belang. Bovendien ondervonden we dat de openklemspanning van de onderzochte cellen sterk afhing van de interacties van het interface zoals die werden gevonden in *Hoofdstuk 6* wat resulteerde in een lagere openklemspanning voor het aselecte mengsel dan voor de dubbellaag heterojunctie cel. Deze observatie is rationeel afgeleid op basis van een simpel verdunningsmodel die we hebben gebruikt om de openklemspanning van een aselecte heterojunctie cel te correleren aan de interacties aan het interface waarbij de morfologie van het mengsel werd meegenomen in het model.

De behoefte aan een verbeterde ruimtelijke verdeling van de donor- en acceptorfasen in een mengsel heeft ons uiteindelijk geleid naar het gebruik van een donor/acceptor diblokcopolymeer, die een microfase scheiding in de orde van grootte van nanometers liet zien, wat vergelijkbaar is met de kenmerkende excitondiffusielengte. Dit resulteerde in een sterk verbeterde fotovoltaïsche gevoeligheid van het diblokcopolymeer ten opzichte van het mengsel van beide afzonderlijke homopolymeren, hoewel de fotovoltaïsche prestaties in het algemeen matig waren. Deze matige fotovoltaïsche prestatie kon worden gerelateerd aan het ontbreken van de ordering over lange afstanden waardoor de transport eigenschappen matig waren.

In conclusie hebben wij gelijkrichters en optoelektronische elementen (devices) gebaseerd op oligomere en polymere organische halfgeleiders onderzocht op de karakteristieken en dit gerelateerd aan de structuureigenschappen. We benadrukken wanordelijke, kristallijne en gemengde halfgeleidende systemen. Er is aangetoond dat binnen een grote verscheidenheid aan lengteschalen, de organisatie van de gebruikte organische halfgeleiders van cruciaal belang is voor de prestaties van deze elementen bestaande uit dunne lagen. Vanaf de moleculaire conformatie, de intermoleculaire rangschikking tot aan de ordering over lange afstanden van organische halfgeleider systemen kunnen de structurele eigenschappen worden afgestemd om elementen te verkrijgen die voldoen aan de industriële eisen.

Acknowledgments

For this thesis I owe a lot to many people, who contributed to the here-presented work, gave their advice, encouraged me or simply were present when needed:

Prof. Dr. Georges Hadziioannou, who offered me a PhD position in his research group and, hence, made this thesis possible. Thank you for giving me freedom and support during my stay in your group.

Dr. Viktor Krasnikov, with whom I could discuss about science and more important topics during endless smoking breaks. With your deep knowledge and broad overview on the field of organic semiconductors, you substantially contributed to a successful time.

Dr. Paul van Hutten, who helped with his astonishing language skills and his clear vision of scientific content. Thank you for discussion, reading, and correcting.

Dr. Martin Brinkmann, who substantially contributed to the work presented in *Chapter 5*.

I particular want to thank Dr. Harry Jonkmann, Dr. Sjoerd Veenstra and Ir. Arend Heeres for the nice cooperation. Without you, *Chapter 6* would not exist.

Especially, I also appreciated the shelter that Prof. Hummelen and Prof. Blom gave me after Georges' leave to Strasbourg. It was nice to be involved in the daily business of your groups and to attend your group meetings. Thanks also to all the group members for the nice time, especially to Valli for willing to be one of my paranimfen.

I also want to thank the reading committee, the professors Blom, Heiser, and Malliaras for the positive assessment of my thesis.

And last but not least, thanks to all the remaining colleagues from the Hadziioannou group: Alice, Amalia, Bert (thanks for your help with the Nederlandse samenvatting!), Christine, Dimitris, Harry Nijland, Jurjen, Karin, Lahoussine, Lutte, Maarten, Marleen, Michel, Nikos, Patrick, Sophia, Ulf, Valérie, You, and the Papyron guys (and girls), who allowed me to join their night-volleyball team.

I also want to thank the secretaries Nettie, Hilda, Karin, and Margriet, who took over the major part of the annoying paper business.

Thanks also to MSC^{plus}, NWO-CW, and PPM for finances.

Finally, I want to thank my friends and family in Groningen and in Germany for their support. Special thanks I owe to my girlfriend Esther. In hard times, you pushed me always in the right direction.

Thanks to all I forgot.

Chris
June 04

List of Publications

C. Melzer, E.J. Koop, V.D. Mihailetchi, and P.W.M. Blom, *Hole transport in poly(phenylene vinylene)/methanofullerene bulk heterojunction solar cells*, Advanced Functional Materials, *accepted for publication* (2003).

C. Melzer, V.V. Krasnikov, and G. Hadziioannou, *Charge transport, injection, and photovoltaic phenomena in oligo(phenylene vinylene)-based diodes*, Journal of Polymer Science, Part B: Polymer Physics **41**, 2665 (2003).

C. Melzer, V.V. Krasnikov, and G. Hadziioannou, *Organic donor/acceptor photovoltaics: the role of* C_{60}*/metal interfaces*, Applied Physics Letters **82**, 3101 (2003).

T. Gu, D. Tsamouras, C. Melzer, V. Krasnikov, J.P. Gisselbrecht, M. Gross, G. Hadziioannou, and J.F. Nierengarten, *Photovoltaic devices from fullerene oligo(phenylene ethynylene) conjugates*, Journal of Chemical Physics and Physical Chemistry **3**, 124 (2002).

B. de Boer, U. Stalmach, P. F. van Hutten, C. Melzer, V.V. Krasnikov, and G. Hadziioannou, *Supramolecular self-assembly and opto-electronic properties of semiconducting block copolymers*, Polymer **42**, 9097 (2001)

B. de Boer, U. Stalmach, C. Melzer, and G. Hadziioannou, *Synthesis and self-organization of PPV-based block copolymers for photonic applications*, Synthetic Metals **121**, 1541 (2001).

V.V. Krasnikov, C. Melzer, L. Ouali, U. Stalmach, and G. Hadziioannou, *Interpenetrating morphologies for photovoltaic devices*, Abstract of Papers of the American Chemical Society **219**, 412 (2000)

A. Fort, C. Melzer, J. Muller, O. Cregut, S. Mery, J.F. Nicoud, C. Combellas, G. Mathey, and A. Thiebault, *New results on low* T_G *photorefractive materials*, Proceedings of the SPIE **3471**, 88 (1998).

L. Mager, C. Melzer, M. Barzoukas, A. Fort, S. Mery, J.F. Nicoud, *High net gain at 514 nm in a photorefractive polymer doped with a chalcone derivative*, Applied Physics Letters **71**, 2248 (1997).

Stellingen

behorende bij het proefschrift van Christian Melzer
te verdedigen op 2 juli 2004

“There are two things that are infinite: the universe and the human stupidity. But, concerning the universe I am not yet certain.”
(*Albert Einstein, 1879-1955*)

“The climb on the ladder of social prestige often ends with a horrible muscle ache.”
(*Sir Peter Ustinov, 1921-2004*)

Age is just a matter of your mind. It does not matter, if you don't mind.

“The people should again learn to work, rather than to live on the expenses of the public.”
(*Marcus Tullius Cicero, 106 - 43 BC*)

“I prefer to be roughly right than exactly wrong.”
(*John Maynard Keynes, 1883-1946*)

The most typical Dutch culinary specialties are loempias.

The relation between a big and a small country of similar cultural background reminds me of the relation between siblings, they express permanently their aversion, while in reality they love each other.

The World Wide Web proved that too much information equals no information.

The problem with disordered semiconductors is their disorder.

“By organic, one customarily means a compound containing carbon. Of the almost two million compounds known, approximately 90% are organic.”
(“*Electronic Processes in Organic Crystals*”, *Martin Pope and Charles E. Swenberg, Oxford University Press, New York, 1982*)

Christian Melzer
June 04